A MATHEMATICAL AND COMPUTATIONAL MULTISCALE CLOTHING

MODELING FRAMEWORK

by

Xiaolin Man

A thesis submitted in partial fulfillment
of the requirements for the Doctor of
Philosophy degree in Civil and Environmental Engineering
in the Graduate College of
The University of Iowa

December 2006

Thesis Supervisor: Professor Colby C. Swan

Graduate College
The University of Iowa
Iowa City, Iowa

CERTIFICATE OF APPROVAL

_____

PH.D. THESIS

_____

This is to certify that the Ph.D. thesis of

Xiaolin Man

has been approved by the Examining Committee
for the thesis requirement for the Doctor of Philosophy
degree in Civil and Environmental Engineering at the December 2006
graduation.

Thesis Committee: _____
                       Colby C. Swan, Thesis Supervisor

                  _____
                       Asghar M. Bhatti

                  _____
                       Jia Lu

                  _____
                       Shaoping Xiao

                  _____
                       Han-Chin Wu

To my wife, Xinxin and to our parents

ABSTRACT

In many circumstances, clothing adversely impacts human performance while also providing protection from exposure to a wide spectrum of external hazards. For a successful design of protective clothing systems, two competing factors, i.e. maximizing the protection that it provides while minimizing the negative impact that it has on performance, have to be balanced. However, due to the lack of understanding on the complex nature of clothing-wearer interactions and the limitation of available tools and approaches, the design task has always been a challenge. In this study, the mechanical aspect of the clothing-wearer interaction is investigated. The objective is to realistically describe clothing with computational models and to then exercise these models to realistically predict their impact on wearers' performance for given tasks. With a knowledge of how clothing impacts human performance, the clothing can be re-designed to improve performance.

Computational solid mechanics approaches are adopted here. A mathematical clothing modeling framework is developed and the contact tractions that clothing exerts on a wearer for prescribed motions are determined. Based on these tractions, other physical quantities are derived to quantify the clothing's impact. The clothing modeling framework includes four components: (1) a macroscale clothing/fabric model, which represents highly flexible fabrics; (2) a mesoscale fabric/material model, which captures the complex material properties of woven fabrics; (3) a contact computation and collision detection module, which identifies potential collision and enforces appropriate contact constraints; and (4) a digital human model, which provides the definition of the wearer's body surface and kinematics description.

In constructing the framework, many challenging issues are identified and explored, such as robust computational models for highly flexible and unstable systems, contact computation techniques, efficient collision detection algorithms, and constitutive

modeling of complex fabric properties. Each of these issues still remains its own challenge and the solution adopted may require improvement. However, the novel framework presented in this work provides a construct to incorporate these individual components and has been proved effective in studying the mechanical interactions between clothing and wearers.

TABLE OF CONTENTS

LIST OF BOXES

LIST OF FIGURES

Figure

CHAPER 1

INTRODUCTION

1.1 Motivation

Clothing, besides its aesthetic function, has long been used by human beings for protection against adversities and hazards, such as severe weather or weapon attacks. Nowadays, protective clothing has been widely employed in various applications, ranging from civilian to military. Special suits have been designed for agriculture workers, fire fighters and astronauts to protect them against exposure to toxic chemicals, extreme heat or hazardous radiation etc. Sports gears have been developed to protect athletes in competitive sports activities. Body armors, helmets, boots, nuclear, biological and chemical (NBC) warsuits have been constructed to protect soldiers in various warfare.

While clothing systems provide protection, they can also negatively impact wearers' performance in many aspects [9]. Physiologically, it has been well established, e.g. [4-6], that a chemical protective suits due to its impermeability and high insulation properties can significantly constrain the heat dissipation and impose heat stress on a wearer. Mechanically, it has been observed as in [4-6] that clothing can restrict wearers' mobility, dexterity or range-of-motion and interfere with the execution of tasks. Clothing can also have negative psychological effects on wearers as reported in [7,8]. These factors in addition to many others not mentioned here interact and affect wearers' performance in a very complex way [10]. Moreover, the negative impact may lead to rejection of protection clothing, thus increasing the risk of injury or casualty.

Consequently, in order to design a good protective clothing system, two competing factors, i.e. maximizing the protection the clothing provides while minimizing the negative impact it has on performance, have to be balanced. Due to the lack of understanding on the complex nature of clothing-wearer interaction and the limitation of available tools and approaches, however, the design task has always been a challenge.

Many factors considered in clothing-wearer interaction currently adopt subjective measures. The vague definitions of these measures limit the quantification and comparison of the factors and obscure the understanding of the interactions between clothing and wearers. Most approaches and tools currently adopted are based on experimental studies, which have been effective in identifying the factors yet provide limited help in understanding them as it is difficult to isolate the huge volume of interacting factors and to conduct experiments that test all the possibilities. For example, an important factor considered in the clothing-wearer interaction is fit and sizing, which is usually measured by visual identification of the stress regions, where fabrics are stretched and are thus considered as restriction on the wearer's motion. The visual identification can be subjective and inconclusive. In addition, for physical try-on, prototyping and subjects are needed, which can be time-consuming and expensive considering the large anthropometry variations in wearers and the iterative nature of a design cycle.

It is thus instrumental to construct an analysis framework, which can quantify the effects a given design may have on the wearers' performance and can thus lead to better understanding of the clothing-wearer interaction problem. Based on the analysis framework, a design tool can be developed to facilitate the design process for protective clothing. This very idea motivated the research presented in this work, where a mathematical clothing modeling framework is investigated.

1.2 Objectives and organization

Clothing impacts a wearer in various ways and the factors can be physiological, mechanical and psychological etc. This work is by no means to include all the factors. Instead, only the mechanical factors are considered here. Two notations justify the choice: (1) the mechanical effects are most likely to be related to objective measures, eliminating the uncertainty due to the subjectivity; (2) the mechanical effects constitute

the fundamental component of the clothing-wearer interaction, on which other factors depend. For example, the heat dissipation feature of clothing is closely related to the air space between the clothing and the wearer and the information is determined by the mechanical interaction.

In this work, a computational framework for clothing modeling is constructed and the mechanical interactions between clothing on wearers are investigated. Computational models are developed for both clothing and wearers and their interaction are calculated using computational solid mechanics approaches. The main focus of the study is to explore the construction of the entire framework rather than to develop novel techniques to solve the individual mechanics problems involved. Due to this reason, some mature methods in computational solid mechanics are directly applied here while some are developed if they are not available.

The quantity studied here is the contact forces or tractions clothing exerts on a wearer. Given the wearer's motion, the contact forces are determined by considering the contact constraints between the cloth and the wearer's body surface. Based on the contact forces, other physical quantities are derived and they are then interpreted as the impacts clothing has on the wearer for the given motion. With this scenario, the clothing modeling framework is decomposed into the following four components: (1) a macroscale clothing/fabric model, which basically represents a garment under macroscopic loading, such as a given posture the wearer undertakes; (2) a mesoscale fabric/material model, which captures the complex material properties of woven fabrics; (3) a contact computation and collision detection module, which identifies potential collision and enforces appropriate contact constraints; and (4) a digital human model, which provides the definition of the wearer's body surface and kinematics description.

A multiscale terminology is adopted in the discussion of fabric modeling. This is due to the complex hierarchical constituents of varying length scales observed in woven fabrics. On macroscale, fabrics are perceived as thin plates or membranes. On

mesoscale, discontinuous yarn structures are observed and the interactions of the interwoven yarns determine the macroscopic material properties of fabrics. On microscale, each yarn is a fiber bundle and the behaviors of the bundle govern the overall properties of a yarn. A schematic of the multiscale hierarchy view of woven fabrics is shown in Fig.1. In this work, fabric modeling on the macroscale and the mesoscale are investigated and computational homogenization techniques are applied to relate the mesoscale yarn interactions to the macroscale fabric properties. While the microscale problem of the fiber bundles is not covered here.

Macroscale garment and fabrics

Mesoscale yarn structures
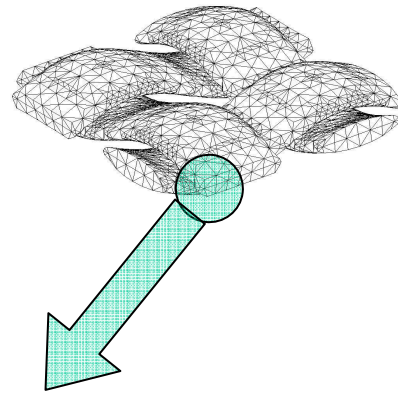
Microscale fiber bundles
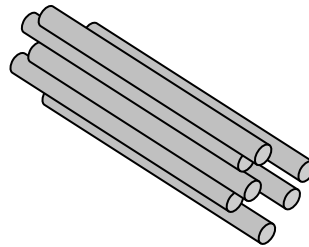
Figure 1: A schematic view of multiscale modeling of woven fabrics

      The organization of the paper is as follows: In Chapter 2, the macroscale clothing/fabric modeling is discussed. Previous research works on the subject are first reviewed and a fabric model based on geometrically nonlinear shell finite element formulation is proposed. In Chapter 3, contact computation and collision detection techniques are summarized and two algorithms are devised to solve contact problems on the macroscale and the mesoscale, respectively. In Chapter 4, the complexities in fabric properties and their constitutive modeling are presented. Computational homogenization and unit cell analysis techniques for mesoscale fabric/material modeling are proposed. In Chapter 5, the digital human model developed for this study is briefly introduced and the clothing-wearer interaction studies based on the proposed clothing and human model are presented. Finally, the paper is summarized in Chapter 6 and research visions are shared as well.

CHAPTER 2

MACROSCALE FABRIC MODELING

As highly flexible media, clothing fabrics develop complex configurations with vague wrinkling patterns when draped onto objects or human bodies. Due to the small fabric thickness, these wrinkling configurations are very unstable and change responsively to tiny perturbations. The vague and vibrant fabric behavior, though quite appealing to the eyes of artists and fashion designers (Fig.2), poses a great challenge to mathematical modeling of clothing mechanics. In this chapter, numerical models that can realistically represent the complex fabric feature are studied.

Figure 2: Study of Madonna and Child with St Anne by Leonardo da Vinci

A major momentum in cloth/fabric modeling research is accredited to computer graphics community as movie and game industries try to create realistic visual effects and animations related to clothing. The approach that prevails in this area is particle-based method, which treats cloth as a dynamic system composed of interacting mass points or particles and solves cloth animations by time integration of the system. Simple as it is,

the particle-based method does shed light on the essence of cloth modeling, i.e. evolution of a dynamic system, and it is capable of generating realistic (even stunning) animations as shown in Fig.3. However, the method falls short in relating a model to real fabric properties. A general practice an animator adopts is to tweak the parameters of a particle model until the animation looks right visually.
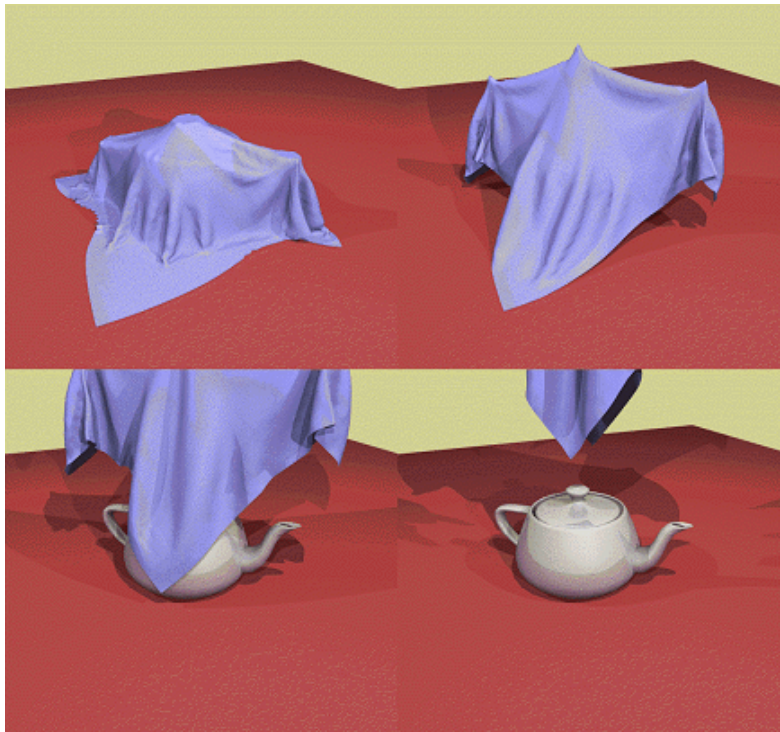
Figure 3: A cloth drape simulation by Breen using a particle model

Apart from particle-based method, another type of approach treats fabric as a deformable surface. Local equilibrium of a continuous medium is usually considered and used as a point of depart. Numerical models are derived following standard computational techniques, such as finite difference methods of finite element methods. A typical application of this approach, mostly contributed by textile and mechanical engineers, is to study the effects of fabric material properties on its drape configurations.

In their models, fabric drape is formulated as an equilibrium problem and solved with finite element methods, which allows incorporation of various material models. The surface-based approach is generally more rigorous in a mathematical and mechanical sense but tends to be more complex than the particle-based method.

In this work, a thorough study on both approaches is conducted. A representative particle model is implemented first. And a finite element model is formulated and constructed as well. A comparison of the two approaches is provided and suggestions on macroscale fabric modeling are presented.

<u>2.1 Previous works on clothing simulation</u>

2.1.1 Particle-based methods

<u>2.1.1.1 Mass-spring models</u>

In 1995, Provot [11] proposed a mass-spring cloth model. In his model, fabrics were modeled as an array of mass particles inter-connected by linear springs of three different types, structural, shear and flexion springs characterizing the stretching, in-plane shear and bending deformation of fabrics respectively. As illustrated in Fig.4, structural springs connect a particle with its direct neighbors along the two perpendicular axes, which are usually aligned with warp and weft yarn directions, while shear springs connect a particle with its neighbors in the diagonal directions. Flexion springs are also along the two perpendicular yarn axes but each connects every other particles.

Since the interaction between two inter-connected particles was defined as a linear spring, given the positions of two particles, say i and j, the forces exerted on them can be computed as

$$\mathbf{F}_i = k\left(|\mathbf{d}| - l_0\right)\frac{\mathbf{d}}{|\mathbf{d}|} \text{ and } \mathbf{F}_j = -k\left(|\mathbf{d}| - l_0\right)\frac{\mathbf{d}}{|\mathbf{d}|}, \qquad (2.1)$$

where $\mathbf{d} = \mathbf{x}_j - \mathbf{x}_i$ is the relative position vector of the two particles and l_0 and k denote the free length and stiffness of the spring respectively.
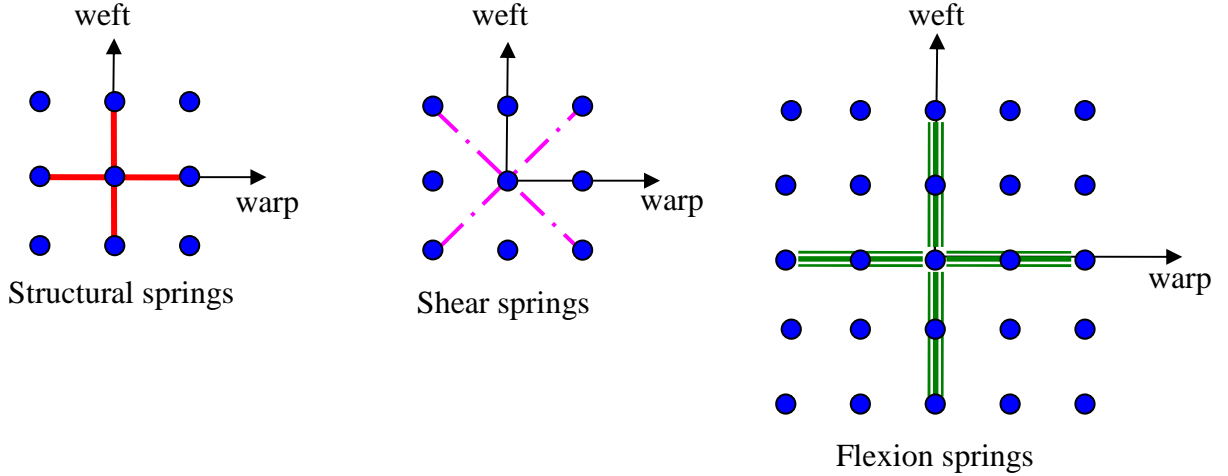
Figure 4: Provot's mass-spring model

The evolution of the system was obtained by the time integration of the particle accelerations, $\mathbf{a}_i = \sum \mathbf{F}_i / m_i$, where m_i denotes the mass of particle i and $\sum \mathbf{F}_i$ the sum of total forces applied on it. An explicit time integration scheme was adopted, which is summarized as follows

$$\mathbf{a}(t + \Delta t) = \frac{1}{m} \sum \mathbf{F}(t);$$
$$\mathbf{v}(t + \Delta t) = \mathbf{v}(t) + \Delta t \cdot \mathbf{a}(t + \Delta t); \quad . \tag{2.2}$$
$$\mathbf{x}(t + \Delta t) = \mathbf{x}(t) + \Delta t \cdot \mathbf{v}(t + \Delta t).$$

Since the step size of an explicit integration is controlled by the stiffness of the system, relatively compliant springs were used, which resulted in unrealistic overstretch in some springs. To address this issue, a heuristic method was proposed by Provot to adjust the positions of the particles associated with the overstretched springs.

An extension of the mass-spring model was proposed by Choi and Ko [12]. They considered the buckling effect of fabrics and included it in the formulation of the bending springs. A buckled segment of fabric of length L subjected to a compressive load P was assumed to be pinned on both ends as shown in Fig.5, which yields the following equilibrium equation

$$k_b \kappa + Py = 0, \tag{2.3}$$

where k_b is the bending rigidity, κ the curvature and y denotes the deflection. Numerical solutions of this differential equation were found for different load levels. The strain energy due to bending, which in is general defined as

$$E = \frac{1}{2} \int_0^L M \kappa ds, \tag{2.4}$$

can be obtained by integrating the curvature and moment in terms of the arc-length of the spring, s. In doing this, the length of the fabric segment was assumed to remain the same before and after buckle as L. In stead of using the numerical solution of Equation (2.3) for the integration, the curvature κ was assumed to be a constant for simplicity and the integration became

$$E = \frac{1}{2} k_b L \kappa^2. \tag{2.5}$$

Choi and Ko expressed the curvature in terms of the length of a bending spring as

$$\kappa = \frac{2}{L} \text{sinc}^{-1} \left(\frac{|\mathbf{d}|}{L} \right), \tag{2.6}$$

where $\text{sinc}(x) = \sin(x)/x$. This relationship can be derived by noticing that the radius

$$\rho = \frac{L}{2\theta} \text{ and } \rho = \frac{|\mathbf{d}|}{2\sin\theta}, \tag{2.7}$$

which yields

$$\frac{|\mathbf{d}|}{L} = \frac{\sin\theta}{\theta} \tag{2.8}$$

and thus

$$\theta = \text{sinc}^{-1}\left(\frac{|\mathbf{d}|}{L}\right). \tag{2.9}$$

The spring force, which is the derivative of the bending energy in Equation (2.5), was derived as

$$\begin{aligned}\mathbf{f}_i &= k_b L \kappa \frac{d\kappa}{d|\mathbf{d}|}\frac{\mathbf{d}}{|\mathbf{d}|}\\ &= k_b \kappa^2 \left(\cos\frac{\kappa L}{2} - \text{sinc}\frac{\kappa L}{2}\right)^{-1}\frac{\mathbf{d}}{|\mathbf{d}|},\end{aligned} \tag{2.10}$$

which is a nonlinear force representing the compression/buckling behavior of fabrics.

Choi and Ko's work provides some insight into the physical meaning of the flexion/bending spring used in a mass-spring model. In fact, it is more appropriate to name it as a compression spring, since the spring directly models the buckling response of fabrics subjected to compressive loading. However, as the buckling is essentially a deformation controlled by bending, the spring is also representative of the bending behavior of fabrics.

Simple as they are, mass-spring models are capable of producing visually convincing animations and have been widely adopted in computer graphics community for clothing simulation. However, since the models are not related to any real fabric properties, they cannot simulate a specific fabric type without modifications and the mechanical response they predict may not be realistic. Moreover, for complicated

geometry, if the structural springs are not aligned with the warp and weft directions, unrealistic results are observed.
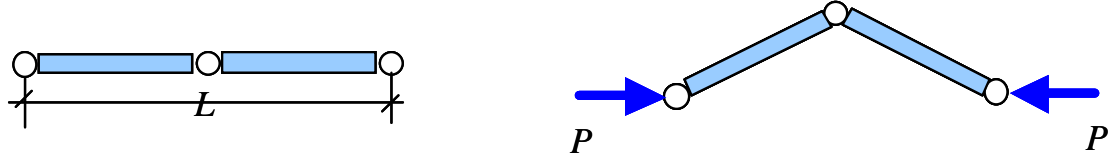
Figure 5: Fabric buckling model used by Choi and Ko

2.1.1.2 Particle models

Instead of using simple linear elastic springs, some researchers constructed more sophisticated particle-based fabric models. Motivated by Hearle [15]'s comments on the inadequacy of traditional continuum theory for fabric modeling, Breen et al. [13,14] proposed a discrete fabric model based on interacting particles. They founded their work "on the premise that by modeling the low-level structures of a material and computationally aggregating their interactions, correct macroscopic behavior will emerge". With their approach, a piece of fabric is modeled as an array of particles conceptually representing the crossing points of warp and weft yarns in plain weave fabric. For computation feasibility, a particle in the model actually represents a fabric patch with dimensions determined by the discretization resolution and the interactions between particles are the aggregation of those between the represented patches.

Four basic mechanical interactions between particles, i.e. repulsion, stretching, bending and trellising (in-plane shear), were modeled by the definition of energy functions and the strain energy of particle i was the summed as

$$U_i = U_{repel_i} + U_{stretch_i} + U_{bend_i} + U_{trellis_i}. \qquad (2.11)$$

The repulsion energy U_{repel_i} was an artificial energy designed to prevent self-intersection of the cloth and was calculated by summing over all particles as

$$U_{repel_i} = \sum_{j \neq i}^{n} R(r_{ij}), \tag{2.12}$$

with n denoting the total number of particles in the model and function R defined as

$$R(r) = \begin{cases} C_0 [(\sigma - r)^5 / r], & r \leq \sigma \\ 0, & r > \sigma \end{cases} \tag{2.13}$$

where r denoted the distance between two particles and σ the nominal distance between the two. The stretching energy $U_{stretch_i}$ was defined between particle i and its four neighbors along the yarn directions as

$$U_{stretch_i} = \sum_{j \in N_i} S(r_{ij}), \tag{2.14}$$

where N_i was the set of the four neighbors and function S was approximated by

$$S(r) = \begin{cases} 0, & r \leq \sigma \\ C_0 [(r - \sigma)/\sigma]^5, & r > \sigma \end{cases}. \tag{2.15}$$

C_0 in both Equation (2.13) and (2.15) was a stiffness parameter. According to Breen, the combination of these two energy functions should "constrain each particle tightly to the nominal distance σ from each of its four-connected neighbors" and a "separation force" between neighboring particles can be derived as

$$F(r) = \frac{\partial(R + S)}{\partial r} = \begin{cases} -C_0(4r + \sigma)(r - \sigma)^4 / \sigma^2, & r \leq \sigma \\ 5C_0(r - \sigma)^4 / \sigma^5, & r > \sigma \end{cases} \tag{2.16}$$

From this equation, one may notice that in addition to its original purpose, preventing cloth from self-intersection, the repulsion energy also describes the compression behavior of fabric yarns. However, this may lead to an ambiguity regarding the choice σ. For compression σ is the free distance between two neighboring particles, which depends on

the grid spacing of discretization resolution, while for repulsion σ is the minimum distance keeping clothing from self-contact. These two quantities are different in magnitudes and need to be distinguished.

Noticing that "the bending and trellising properties are significant contributors to the overall draping behavior of cloth", Breen et al. formulated the energy functions for bending and trellising based on experimental data obtained from Kawabata Evaluation System for Fabrics (KES-F) [16]. The bending energy at particle i was defined by

$$U_{bend_i} = \sum_{j \in M_i} B(\theta_{ij}), \qquad (2.17)$$

where M_i was the set of six angles formed by the segments connecting particle i and its eight nearest neighbors along the yarn directions (Fig.6a). Assume that each particle represents a $\sigma \times \sigma$ fabric patch, the bending energy due to the bending angle θ made by two segments in either yarn direction was evaluated as

$$B = \frac{M\kappa}{2}\sigma^2, \qquad (2.18)$$

where M and κ denoted moment and curvature in the bending direction and the relationship $M = M(\kappa)$ was obtained from Kawabata tests . For constant curvature, κ was related to the bending angle θ shown in Fig.6a by

$$\kappa = \frac{2}{\sigma}\cos\left(\frac{\theta}{2}\right). \qquad (2.19)$$

Trellising deformation at a particle was characterized by the shear angle ϕ shown in Fig.6b. The trellising energy function at particle i was defined as

$$U_{trellis_i} = \sum_{j \in K_i} T(\phi_{ij}), \qquad (2.20)$$

where K_i was the set of four neighbors of particle i along the yarn directions. Function T was derived by considering the work performed by external force in a Kawabata shear test and it was computed as

$$T(\phi) = \int Fl \cos \phi d\phi, \qquad (2.21)$$

where F and ϕ denoted the measured shear force and angle respectively while l was the width of the Kawabata shear test specimen. Since each particle represents a $\sigma \times \sigma$ fabric patch, Equation (2.21) was scaled by a ratio of the area of the patch to the area of actual Kawabata shear test specimen.

Particles associated with bending   Bending angle θ

(a) Bending

Particles associated with trellising   Trellising angle ϕ

(b) Trellising
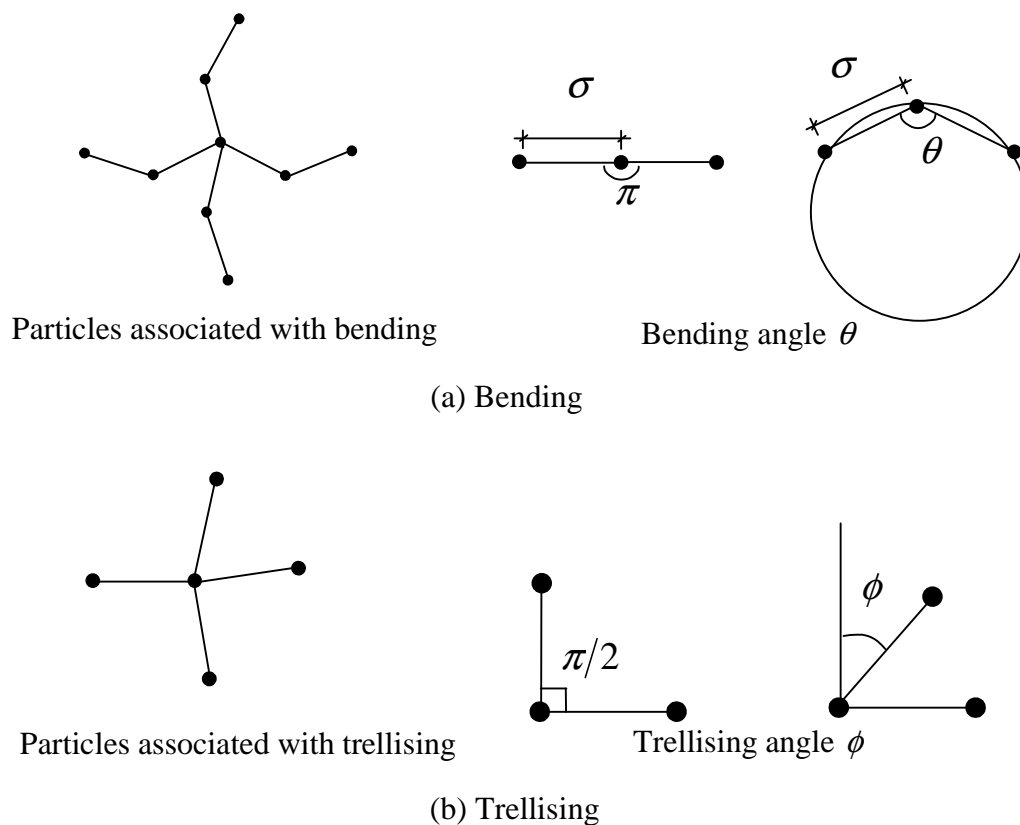
Figure 6: Breen's energy function definitions

Based on the particle model, the draping characteristics of fabrics were predicted by minimizing the total energy in the particle system and the results compared favorable with experimental validations. The most significant contribution of this model is that the mechanical properties of a specific fabric type can be included through the formulation of the energy functions, which make it possible to simulate the macro-scale behaviors of different fabric types. As the internal forces between particles can be derived from the definitions of the energy functions, the model can be reformulated as a dynamic problem and the evolution of the particle system can thus be computed. The reformulated dynamic particle-based model can be viewed as a generalized mass-spring model with nonlinear internal forces.

Motivated by Breen et al.'s work, Eberhardt et al. [17] proposed a model to simulate the dynamics of fabric draping. Like Breen's model, a rectangular grid aligned with the warp and weft directions of cloth was adopted with each grid point representing a particle, whose trajectory is governed by the Lagrange equation

$$\frac{d}{dt}\frac{\partial L}{\partial \mathbf{v}_i} = \frac{\partial L}{\partial \mathbf{x}_i},$$ (2.22)

where $\mathbf{x}_i$ and $\mathbf{v}_i$ denote the position and velocity of particle i respectively. The Lagrange function of the particle system was evaluated by

$$L = \sum_{i=0}^{n-1} E_{kin_i} - \left(\sum_{i=0}^{n-1} E_{pot_i} + \sum_{i=0}^{n-1} E_{t_i} + \sum_{i=0}^{n-1} E_{s_i} + \sum_{i=0}^{n-1} E_{b_i} \right),$$ (2.23)

where E_{kin_i} and E_{pot_i} are the kinetic energy and gravitational potential of particle i respectively and E_{t_i}, E_{s_i} and E_{b_i} strain energies corresponding to three types of internal forces, tension/compression, shearing and bending.

To construct accurate energy functions, Kawabata experimental data was used. Piecewise linear functions were used to approximate the original Kawabata curves and two parameters, C, the slope of the curve and h, the intercept of the curve with x-axis,

were retrieved for each linear approximation segment. Based on the two parameters, a quadratic form of strain energy for the approximated neighborhood was constructed.

The bending energy at a particle was assumed to be a function of the two bending angles about the two yarn directions as shown in Fig.7a and it was given as

$$E_b = \sum_{i=1}^{2} \frac{1}{2} C_{b_i} \left(\psi_i - \pi - h_{b_i} \right)^2 . \tag{2.24}$$

The shearing energy at a particle was considered as a function of the four shear angles formed by the gridlines connecting itself and its four directly connected neighbors (Fig.7b) and was defined as

$$E_s = \sum_{i=1}^{4} \frac{1}{2} C_{s_i} \left(\varphi_i - \frac{\pi}{2} - h_{s_i} \right)^2 . \tag{2.25}$$

(a) Bending   (b) Shear
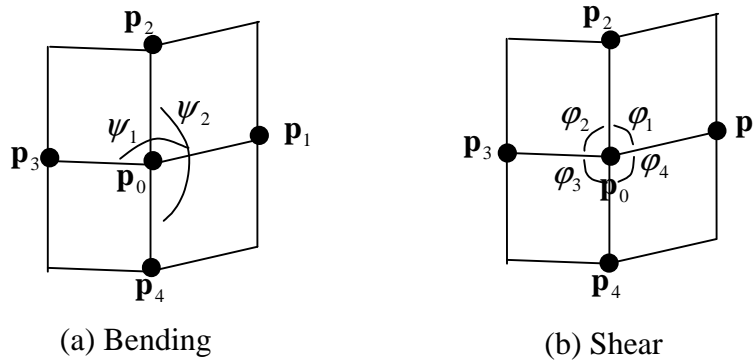
Figure 7: Eberhardt's energy function definitions

Likewise, the tension/compression energy was defined as follows

$$E_t = \begin{cases} \sum_{i=1}^{4} \frac{1}{2} C_{i,t_1} \left(|\mathbf{p}_0 - \mathbf{p}_i| - d_i - h_{t_i} \right)^3, & if |\mathbf{p}_0 - \mathbf{p}_i| \ge d_i \\ \sum_{i=1}^{4} \frac{1}{2} C_{i,t_2} \left(|\mathbf{p}_0 - \mathbf{p}_i| - d_i - h_{t_i} \right)^3, & if |\mathbf{p}_0 - \mathbf{p}_i| < d_i \end{cases} \tag{2.26}$$

where $\mathbf{p}_0$ and $\mathbf{p}_i$ denote the position of a particle and one of its four neighbors respectively and d_i is the free distance between them. Different values for the parameters C and h were stored for each linear approximation segment of the Kawabata curves and the right set was picked given the deformation and the history. Then the Lagrange function was differentiated symbolically and the resulting differential equations were solved by a Runge-Kutta method with adaptive step-size control. With this approach, the hysteresis of fabrics was included.

<div align="center">2.1.2 Surface-based methods</div>

<u>2.1.2.1 Nonlinear elastic surface models</u>

In order to create animations of deformable bodies in computer graphics, Terzopoulos et al. [18] introduced a physical-based model by applying the principles of elasticity and differential geometry. They started with Lagrange equation, which governs the motion of a deformable body

$$\frac{\partial}{\partial t}\left(\mu\frac{\partial \mathbf{r}}{\partial t}\right)+\gamma\frac{\partial \mathbf{r}}{\partial t}+\frac{\delta\varepsilon(\mathbf{r})}{\delta\mathbf{r}}=\mathbf{f}(\mathbf{r},t)\,, \tag{2.27}$$

where $\mathbf{r}(\mathbf{a},t)$ is the position of a material point $\mathbf{a}$ at time t, $\mu(\mathbf{a})$ the mass density at the point, $\gamma(\mathbf{a})$ the damping density, and $\mathbf{f}(\mathbf{r},t)$ the external forces applied. The functional $\varepsilon(\mathbf{r})$ is the strain energy function characterizing the elastic deformation of the object. For a surface, the strain energy function was assumed to be

$$\varepsilon(\mathbf{r})=\int_{\Omega}\left(\eta_{ij}(G_{ij}-G_{ij}^0)^2+\xi_{ij}(B_{ij}-B_{ij}^0)^2\right)da_1da_2\,, \tag{2.28}$$

where

$$G_{ij}=\frac{\partial \mathbf{r}}{\partial a_i}\cdot\frac{\partial \mathbf{r}}{\partial a_j}\,,\quad B_{ij}=\mathbf{n}\cdot\frac{\partial^2\mathbf{r}}{\partial a_i\partial a_j}\,, \tag{2.29}$$

and **n** denotes the unit surface normal. The deformation measures **G** and **B** are the first and second fundamental forms of surfaces and the superscript 0 indicates the quantities associated with the reference configuration. Then the conservative forces, i.e. $\delta\varepsilon/\delta\mathbf{r}$, are given by

$$\mathbf{e}(\mathbf{r}) = -\frac{\partial}{\partial a_i}\left(\alpha_{ij}\frac{\partial\mathbf{r}}{\partial a_i}\right) + \frac{\partial^2}{\partial a_i\partial a_j}\left(\beta_{ij}\frac{\partial^2\mathbf{r}}{\partial a_i\partial a_j}\right),$$ (2.30)

where

$$\alpha_{ij} = \eta_{ij}\left(G_{ij} - G_{ij}^0\right)$$
$$\beta_{ij} = \xi_{ij}\left(B_{ij} - B_{ij}^0\right)$$

are constitutive functions describing the elastic properties of the material. By changing η_{ij} and ξ_{ij}, different materials, such as rubber, paper, metal and cloth, were modeled. For cloth, η_{ij} was set to large values and ξ_{ij} to zero, indicating strong resistance to stretching and compliance to bending. Equation (2.27) together with (2.30) was discretized by finite difference methods over a regular mesh and a set of second-order ordinary differential equations as

$$\mathbf{M}\frac{\partial^2\mathbf{r}}{\partial t^2} + \mathbf{C}\frac{\partial\mathbf{r}}{\partial t} + \mathbf{K}(\mathbf{r})\mathbf{r} = \mathbf{f},$$ (2.31)

was obtained and solved by implicit time integration.

Terzopoulos et al. also proposed the strain energy functions for curves and solids based on the deformation measures derived from the differential geometry. Since these deformation measures are invariant under rigid body motion, large deformation was properly modeled and realistic simulations were obtained. In one of their later work, Terzopoulos and Fleischer [18] even included viscoelasticity, plasticity and fracture into their model, enabling a complete physical-based simulation framework for computer

graphics. Terzopoulos's general model was later adopted and extended by Thalman et al. [20] in cloth simulation.

2.1.2.2 Finite element models

In 1991, Collier et al [21] showed that fabric drape can be predicted using a nonlinear shell finite element model. A circular piece of cotton plain-weave fabric was modeled and the drape predicted by the model was compared with experimental results of drape test [22, 23]. A four-node quadrilateral flat-shell element, which combines a membrane element with a plate-bending element, was adopted and Green strain measure was used. Two constitutive models, isotropic and orthotropic linear elasticity were tested and it was found out that the orthotropic one is more appropriate for fabric modeling. Three input parameters were needed for the orthotropic model, the tensile moduli in two yarn family directions, which were measured using KES-F system, and the Poisson's ratio, for which literature values were used. An interesting effect was reported that the deformed shape was sensitive to the Poisson's ratio.

In the mid 90s, Chen and Govindaraj [24, 25] proposed a fabric model based on nine-node degenerated shell elements. The constitutive relationship adopted was given by the following form

$$
\begin{Bmatrix} \sigma_1 \\ \sigma_2 \\ \sigma_6 \end{Bmatrix} = \begin{bmatrix} Q_{11} & Q_{12} & 0 \\ Q_{12} & Q_{22} & 0 \\ 0 & 0 & Q_{66} \end{bmatrix} \begin{Bmatrix} \varepsilon_1 \\ \varepsilon_2 \\ \varepsilon_6 \end{Bmatrix} \text{ and } \begin{Bmatrix} \sigma_4 \\ \sigma_5 \end{Bmatrix} = \begin{bmatrix} Q_{44} & 0 \\ 0 & Q_{55} \end{bmatrix} \begin{Bmatrix} \varepsilon_4 \\ \varepsilon_5 \end{Bmatrix},
\tag{2.32}
$$

where σ_i and ε_i denote the stress and strain respectively and Q_{ij} are elastic constants deduced from the plane stress assumption, which read as

$$
Q_{11} = \frac{E_1}{1-v^2}, \ Q_{12} = \frac{vE_1}{1-v^2}, \ Q_{22} = \frac{E_2}{1-v^2}, \ Q_{66} = G_{12}, \ Q_{44} = G_{23}, \ Q_{55} = G_{13},
$$

where E_1 is Young's modulus in the warp direction, E_2 is Young's modulus in the weft direction, G_{12}, G_{23} and G_{31} are shear modulus and ν is Poisson's ratio. Such a constitutive model can be categorized as orthotropic linear elasticity without differentiating Poisson's ratios for different material directions. The Young's moduli and the shear moduli were obtained by KES-F and the Poisson's ratio was determined from tests using an Instron tensile tester. Nonlinear strain measures defined in local curvilinear coordinate frames were adopted and a Newton-Raphson method was used to solve the nonlinear equations. Fabric drape shapes predicted by the model were compared with the actual experiment measurements and good agreements were observed. In addition, Chen and Govindaraj [25] did some parametric studies of the effects of various material properties on the drape deformation. It was found that

- Orthotropy in drape deformation were affected by the thickness and shear modulus. For low shear modulus or small thickness, the model didn't exhibit orthotropic drape shapes even though orthotropic material properties were used.

- Poisson's ratio didn't affect the drape shape, which is contrary to what has been reported by Collier et al. [18].

Moreover, they presented an example showing that Young's and shear moduli retrieved in the low strain range of Kawabata experiment data generated drape shape very close to actual one, which indicated that for fabric drape linear elastic model is an acceptable assumption.

Around the same time, Gan, Ly and Steven [26] also reported a nonlinear shell fabric model. They used the curved degenerated shell element introduced by Bathe in [27]. Green strain and Piola-Kirchhoff stress were used to describe the strains and stresses and the problem was solved using Newton-Raphson method. They assumed that fabrics are linearly elastic and orthotropic. Instead of relating the bending stiffness of fabrics to the Young's moduli based on linear strain assumption as Chen and Govindaraj

[24, 25] did, they assumed that fabrics have independent bending and tensile stiffness and experimental data of fabric bending rigidity obtained from KES-F system were used. In order to eliminate locking, reduced integration with zero energy mode control was applied. Two examples were presented, one simulating two-dimensional cantilever bending and the other simulating three-dimensional drape. The simulation results were checked against experimental measurements and good agreement was found.

Deviating from traditional degenerated shell elements, Eischen [28] proposed a fabric model based on Simo's [29-31] geometrically exact shell theory. Isotropic elastic material model with a nonlinear moment/curvature relationship derived from KES-F system was used and arc-length controlled solution technique was implemented to treat the instability due to fabric buckling. The contact between fabrics and rigid surfaces was considered and the contact constraint was enforced by a penalty method. Examples such as fabric drape and handing were presented.

2.2 A macroscale fabric model using particle method

To understand the detail of fabric modeling using particle-based methods, the mass-spring fabric model proposed by Provot [11] is implemented here. With this model, a piece of fabric is represented as a network of the three types of springs, structural, shear and flexion. The dynamics of the fabric, which is essentially the trajectory of each mass point in the system, is determined by the forward Euler time integration. The implementation is straightforward and visually realistic fabric animations are created with the model. Fig.8 shows a snapshot of a draping simulation of a square fabric piece pinned at two corners on an ellipsoid.

To achieve visual realism with the model, a critical step is to tweak the stiffness parameters for the springs. As the springs are not rigorously defined on the basis of mechanics, it is not straightforward to relate the spring stiffness to actual material properties of fabrics. As a result, visual inspection is heavily relied upon when these

parameters are to be determined. Another observation about the mass-spring model is its mesh dependency. When mesh is refined, the spring stiffness parameters need to be modified. And when irregular mesh is employed, especially when structural springs are not orthogonal, the model does not behave properly. These limitations are due to the lack of explicit definition on the discretization scheme, which relates an actual fabric with a discrete model. Tis weakness motivated the development of a shell finite element formulation presented in the following.
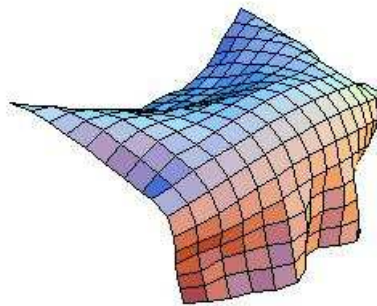
Figure 8: Fabric drape simulation using Provot's mass-spring model

2.3 A macroscale fabric model based on shell formulation

In this section, a macroscale fabric modeling framework based on nonlinear shell finite formulation is constructed. The major concern here is to construct a computational fabric model, which has rigorous specification on the spatial discretization and allows straightforward incorporation of realistic material properties.

A shell finite element with fully nonlinear kinematics description is developed and consistent linearization is conducted. Both the quasi-static and the dynamic formulation are supported and the solution algorithms based on Newmark's methods are presented. St. Venant material model is considered here by assuming a small strain in

fabrics under normal wearing conditions. More discussions on fabric material properties

are presented in Chapter 3.

2.3.1 Geometrically nonlinear shell formulation

2.3.1.1 Problem statement

Total Lagrangian formulation is adopted and the governing equations are

summarized as follows:

$$\left.\begin{array}{c} P_{iJ,J} + \rho_0 b_i = \rho_0 \ddot{u}_i \text{ in } \Omega_0 \\ P_{iJ} N_J = \overline{t}_i^{\,0} \text{ on } \Gamma_{t_i}^0 \\ u_i = \overline{u}_i \text{ on } \Gamma_{u_i}^0 \end{array}\right\} \tag{2.33}$$

where Ω_0 is the reference configuration and P_{iJ} is the first Piola-Kirchhoff stress tensor.

$\Gamma_{t_i}^0$ and $\Gamma_{u_i}^0$ are the parts of the boundary $\partial\Omega_0$ where the traction $\overline{t}_i^{\,0}$ and displacement $\overline{u}_i$

are prescribed. N_J is the outward normal to the boundary in the reference configuration.

With an admissible variation $\delta\mathbf{u}$, the weak form is obtained as

$$\int_{\Omega_0} \delta u_{i,J} P_{iJ} d\Omega_0 = \int_{\Omega_0} \delta u_i \rho_0 b_i d\Omega_0 + \int_{\Gamma_{t_i}^0} \delta u_i \overline{t}_i^{\,0} d\Gamma_0 - \int_{\Omega_0} \delta u_i \rho_0 \ddot{u}_i d\Omega_0 . \tag{2.34}$$

For quasi-static problems, the last term due to inertial is eliminated and the weak form is

written as

$$\int_{\Omega_0} \delta u_{i,J} P_{iJ} d\Omega_0 = \int_{\Omega_0} \delta u_i \rho_0 b_i d\Omega_0 + \int_{\Gamma_{t_i}^0} \delta u_i \overline{t}_i^{\,0} d\Gamma_0 . \tag{2.35}$$

The left-hand side of the preceding is the virtual work done by the internal force, which is

denoted as δW^{int}, and it could be verified that

$$\delta W^{int} = \int_{\Omega_0} \delta F_{iJ} P_{iJ} d\Omega_0 = \int_{\Omega_0} \delta E_{IJ} S_{IJ} d\Omega_0 , \tag{2.36}$$

where $F_{iJ} = x_{i,J}$ is the deformation gradient; $E_{IJ} = \left(F_{kI} F_{kJ} - \delta_{IJ} \right)/2$ is the Green strain

tensor; and $S_{IJ} = F_{Ik}^{-1} P_{kJ}$ is the second Piola-Kirchhoff stress tensor.

2.3.1.2 Geometry and kinematics

The geometrical description of the shell element follows Hughes's work [32]. The initial global position vector of a material point (ξ, η, ζ) in a shell element is defined by the following relation:

$$\mathbf{X}(\xi, \eta, \zeta) = \sum_{A=1}^{nen} N_A(\xi, \eta) \overline{\mathbf{X}}_A + \sum_{A=1}^{nen} N_A(\xi, \eta) z_A(\zeta) \hat{\mathbf{X}}_A , \qquad (2.37)$$

where $\overline{\mathbf{X}}_A$ is the initial position vector of node a; $\hat{\mathbf{X}}_A$ is the fiber director emanating from node A in the fiber direction; $z_A(\zeta)$ is a thickness function; $N_A(\xi, \eta)$ denotes a two-dimensional shape function associated with node A and nen is the number of element nodes. Given the coordinates of the top and bottom surfaces of the shell along each nodal fiber, i.e. $\mathbf{X}_A^+$ and $\mathbf{X}_A^-$, and a parameter $\overline{\zeta} \in [-1, +1]$ designating the natural coordinate of the reference surface, in which shell nodes locate, the quantities in Equation (2.37) can be determined as follows

$$\begin{aligned}
\overline{\mathbf{X}}_A &= \frac{1}{2}(1 - \overline{\zeta})\mathbf{X}_A^- + \frac{1}{2}(1 + \overline{\zeta})\mathbf{X}_A^+ \\
\hat{\mathbf{X}}_A &= (\mathbf{X}_A^+ - \mathbf{X}_A^-)/|\mathbf{X}_A^+ - \mathbf{X}_A^-| \\
z_A(\zeta) &= \frac{1}{2}(1 + \zeta)z_A^+ + \frac{1}{2}(1 - \zeta)z_A^- \\
z_A^+ &= \frac{1}{2}(1 - \overline{\zeta})|\mathbf{X}_A^+ - \mathbf{X}_A^-| \\
z_A^- &= -\frac{1}{2}(1 + \overline{\zeta})|\mathbf{X}_A^+ - \mathbf{X}_A^-|
\end{aligned} \qquad (2.38)$$

where $|\bullet|$ denotes the Euclidean norm. For example, to choose middle surface of the shell as reference, one sets $\overline{\zeta} = 0$ and the nodal position $\overline{\mathbf{X}}_A = (\mathbf{X}_A^+ + \mathbf{X}_A^-)/2$ while the thickness function $z_A(\zeta) = \zeta |\mathbf{X}_A^+ - \mathbf{X}_A^-|/2$ with $\zeta \in [-1, +1]$. The construct is sketched in Figure 2-7. At each node a local coordinate system $(\mathbf{e}_{A1}^f, \mathbf{e}_{A2}^f, \mathbf{e}_{A3}^f)$, named fiber coordinate system, is constructed and nodal rotation is specified with respect to the frame. In the initial configuration $\mathbf{e}_{A3}^f$ is chosen to coincide with the fiber direction $\hat{\mathbf{X}}_A$ and the other two legs are constructed using the algorithm given in [32].
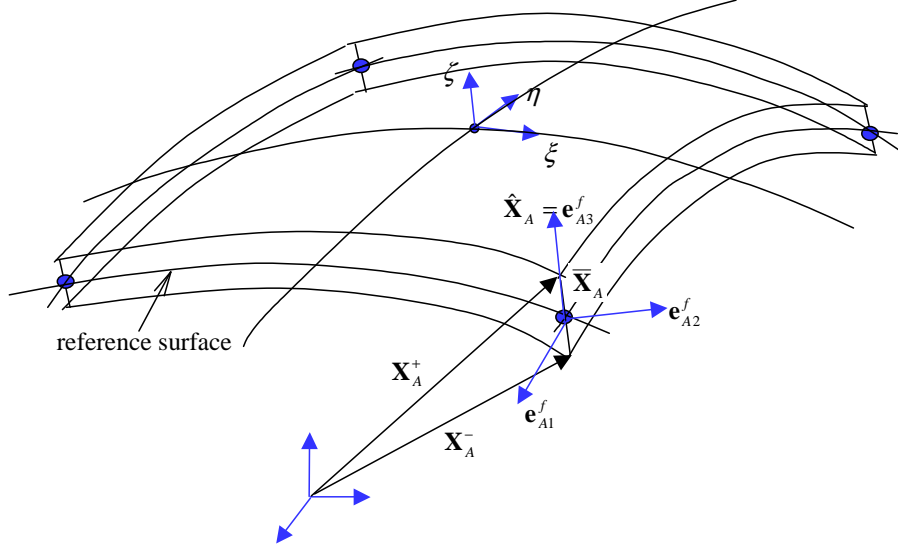
Figure 9: Geometrical description of the shell element

The updated configuration of the shell is defined in a similar manner

$$\mathbf{x}(\xi,\eta,\zeta) = \sum_{A=1}^{nen} N_A(\xi,\eta)\overline{\mathbf{x}}_A + \sum_{A=1}^{nen} N_A(\xi,\eta)z_A(\zeta)\hat{\mathbf{x}}_A \,, \tag{2.39}$$

where $\overline{\mathbf{x}}_A$ and $\hat{\mathbf{x}}_A$ denote the current nodal position and fiber orientation, respectively. For finite deformation, these nodal quantities are related to the initial ones as

$$\overline{\mathbf{x}}_A = \overline{\mathbf{X}}_A + \overline{\mathbf{u}}_A \text{ and } \hat{\mathbf{x}}_A = \mathbf{R} \cdot \hat{\mathbf{X}}_A, \tag{2.40}$$

where $\overline{\mathbf{u}}_A$ denotes the nodal translation and $\mathbf{R}$ is an orthogonal matrix describing a finite rotation of the nodal fiber director. Suppose vector $\hat{\mathbf{x}}_A$ is obtained by rotating $\hat{\mathbf{X}}_A$ by an angle θ about an axis defined by unit vector $\mathbf{n}$. According to Euler's theorem, one has following relation

$$\hat{\mathbf{x}}_A = \hat{\mathbf{X}}_A + \sin\theta\,\mathbf{n}\times\hat{\mathbf{X}}_A + (1-\cos\theta)\mathbf{n}\times(\mathbf{n}\times\hat{\mathbf{X}}_A)\,, \tag{2.41}$$

or

$$\hat{\mathbf{x}}_A = \hat{\mathbf{X}}_A + \frac{\sin\theta}{\theta}\boldsymbol{\theta}\times\hat{\mathbf{X}}_A + \frac{1-\cos\theta}{\theta^2}\boldsymbol{\theta}\times(\boldsymbol{\theta}\times\hat{\mathbf{X}}_A)\,,$$

where $\boldsymbol{\theta} = \theta\,\mathbf{n} = (\theta_1, \theta_2, \theta_3)^T$ is the axial vector of the rotation. By defining a skew-symmetric tensor such that $\boldsymbol{\theta} \times \hat{\mathbf{X}}_A = \boldsymbol{\Omega}(\boldsymbol{\theta}) \cdot \hat{\mathbf{X}}_A$, the rotation matrix can be written as

$$\mathbf{R}(\boldsymbol{\theta}) = \mathbf{I} + \frac{\sin\theta}{\theta}\boldsymbol{\Omega}(\boldsymbol{\theta}) + \frac{1-\cos\theta}{\theta^2}\boldsymbol{\Omega}^2(\boldsymbol{\theta}), \tag{2.42}$$

with

$$\boldsymbol{\Omega}(\boldsymbol{\theta}) = \begin{bmatrix} 0 & -\theta_3 & \theta_2 \\ \theta_3 & 0 & -\theta_1 \\ -\theta_2 & \theta_1 & 0 \end{bmatrix} \text{ and } \theta = (\boldsymbol{\theta} \cdot \boldsymbol{\theta})^{1/2}.$$

In shell kinematics, nodal rotations are permitted about the first two axes of the fiber basis (e.g. $\boldsymbol{\theta}_A = \theta_{A1}^f \mathbf{e}_{A1}^f + \theta_{A2}^f \mathbf{e}_{A2}^f$), which excludes the drilling degree of freedom (DOF) about $\mathbf{e}_{A3}^f$, and the new orientation of fiber director $\hat{\mathbf{X}}_A$ is thus given by

$$\hat{\mathbf{x}}_A = \hat{\mathbf{X}}_A + \frac{\sin\theta}{\theta}\left(\theta_{A2}^f \mathbf{e}_{A1}^f - \theta_{A1}^f \mathbf{e}_{A2}^f\right) + \left(1-\cos\theta\right)\mathbf{e}_{A3}^f. \tag{2.43}$$

The fiber director tip, i.e. $\hat{\mathbf{u}}_A = \hat{\mathbf{x}}_A - \hat{\mathbf{X}}_A$, is

$$\hat{\mathbf{u}}_A = \frac{\sin\theta}{\theta}\left(\theta_{A2}^f \mathbf{e}_{A1}^f - \theta_{A1}^f \mathbf{e}_{A2}^f\right) + \left(1-\cos\theta\right)\mathbf{e}_{A3}^f,$$

which recovers the infinitesimal rotation case $\hat{\mathbf{u}}_A = \theta_{A2}^f \mathbf{e}_{A1}^f - \theta_{A1}^f \mathbf{e}_{A2}^f$ given in [32] when $\theta \to 0$.

To summarize, according to (2.39) and (2.40), the shell configuration is a nonlinear function of nodal translation $\bar{\mathbf{u}}_A$ and rotation $\boldsymbol{\theta}_A$. By defining a nodal displacement vector $\mathbf{d}_A = (\bar{\mathbf{u}}_A, \boldsymbol{\theta}_A)$, it can be written as

$$\mathbf{x} = \mathbf{x}(\mathbf{d}_A) = \sum_{A=1}^{nen} N_A\left(\bar{\mathbf{X}}_A + \bar{\mathbf{u}}_A\right) + \sum_{A=1}^{nen} N_A z_A \mathbf{R}(\boldsymbol{\theta}_A)\hat{\mathbf{X}}_A. \tag{2.44}$$

2.3.1.3 Linearized kinematics

In general, Equation (2.34) and (2.35) are nonlinear and are solved iteratively using Newton's method. In the following, the shell geometry in (2.44) is linearized in the

context of the solution method. Suppose that a trial configuration has been obtained and is given as

$$\mathbf{x}^* = \mathbf{x}(\mathbf{d}_A^*) = \sum_{A=1}^{nen} N_A (\overline{\mathbf{X}}_A + \overline{\mathbf{u}}_A^*) + \sum_{A=1}^{nen} N_A z_A \mathbf{R}(\boldsymbol{\theta}_A^*) \hat{\mathbf{X}}_A . \tag{2.45}$$

An updated configuration $\mathbf{x} = \mathbf{x}(\mathbf{d}_A)$ as given in (2.44) can be linearized about $\mathbf{x}^*$ as follows

$$L[\mathbf{x}]_{\mathbf{d}_A^*} = \mathbf{x}^* + \Delta\mathbf{x}, \tag{2.46}$$

where $\Delta\mathbf{x}$ is the directional derivative of $\mathbf{x}$ along an incremental nodal displacement $\Delta\mathbf{d}_A = (\Delta\overline{\mathbf{u}}_A, \Delta\boldsymbol{\theta}_A)$ and it is computed as

$$\Delta\mathbf{x} = \frac{d}{d\varepsilon} \Big[\mathbf{x}(\mathbf{d}_A^* + \varepsilon\Delta\mathbf{d}_A) \Big] \Big|_{\varepsilon=0}$$

$$= \sum_{A=1}^{nen} N_A \Delta\overline{\mathbf{u}}_A + \sum_{A=1}^{nen} N_A z_A \left[\frac{\partial\mathbf{R}}{\partial\boldsymbol{\theta}_A} \Big|_{\boldsymbol{\theta}_A=\boldsymbol{\theta}_A^*} \Delta\boldsymbol{\theta}_A \right] \cdot \hat{\mathbf{X}}_A \tag{2.47}$$

A nodal rotation is usually specified with respect to the local nodal fiber basis $\mathbf{e}_{Ai}^f, (i = 1,2,3)$ as $\boldsymbol{\theta}_A = \theta_{A1}^f \mathbf{e}_{A1}^f + \theta_{A2}^f \mathbf{e}_{A2}^f$. As the fiber basis in general differs from the global basis $\mathbf{e}_i, (i = 1,2,3)$, a transformation is defined as

$$T_{ij} = \mathbf{e}_{Ai}^f \cdot \mathbf{e}_j . \tag{2.48}$$

The directional derivative of $\mathbf{R}$ in (2.47) is thus expanded as follows

$$\left[\frac{\partial\mathbf{R}}{\partial\boldsymbol{\theta}_A} \Delta\boldsymbol{\theta}_A \right] \cdot \hat{\mathbf{X}}_A = \frac{\partial R_{ij}}{\partial\theta_{A\alpha}^f} \Delta\theta_{A\alpha}^f \hat{X}_{Aj}$$

$$= \left(T_{mi} \frac{\partial R_{mn}^f}{\partial\theta_{A\alpha}^f} T_{nj} \right) \Delta\theta_{A\alpha}^f T_{rj} \hat{X}_{Ar}^f , \quad (\alpha = 1,2) \tag{2.49}$$

$$= T_{mi} \left(\frac{\partial R_{mn}^f}{\partial\theta_{A\alpha}^f} \hat{X}_{An}^f \right) \Delta\theta_{A\alpha}^f$$

where nodal index A is not summed and

$$\frac{\partial \mathbf{R}^f}{\partial \theta_{A1}^f} \hat{\mathbf{X}}_A^f = \begin{pmatrix} \dfrac{\theta_{A1}^f \theta_{A2}^f \cos\theta}{\theta^2} - \dfrac{\theta_{A1}^f \theta_{A2}^f \sin\theta}{\theta^3} \\[2ex] -\dfrac{\left(\theta_{A1}^f\right)^2 \cos\theta}{\theta^2} - \dfrac{\left(\theta_{A2}^f\right)^2 \sin\theta}{\theta^3} \\[2ex] -\dfrac{\theta_{A1}^f \sin\theta}{\theta} \end{pmatrix} \qquad (2.50)$$

$$\frac{\partial \mathbf{R}^f}{\partial \theta_{A2}^f} \hat{\mathbf{X}}_A^f = \begin{pmatrix} \dfrac{\left(\theta_{A2}^f\right)^2 \cos\theta}{\theta^2} + \dfrac{\left(\theta_{A1}^f\right)^2 \sin\theta}{\theta^3} \\[2ex] -\dfrac{\theta_{A1}^f \theta_{A2}^f \cos\theta}{\theta^2} + \dfrac{\theta_{A1}^f \theta_{A2}^f \sin\theta}{\theta^3} \\[2ex] -\dfrac{\theta_{A2}^f \sin\theta}{\theta} \end{pmatrix}$$

Two auxiliary vectors $D\hat{\mathbf{u}}_\alpha^A, (\alpha = 1,2)$ can be defined as follows

$$D\hat{u}_{\alpha i}^A = T_{mi} \frac{\partial R_{mn}^f}{\partial \theta_{A\alpha}^f} \hat{X}_{An}^f \quad (A \text{ not summed}), \qquad (2.51)$$

which can be interpreted as the linearized displacement of fiber director tip. According to (2.50) and (2.48), the vectors $D\hat{\mathbf{u}}_\alpha^A$ depend on both the reference nodal fiber basis $\mathbf{e}_{Ai}^f$ and the rotation angle $\boldsymbol{\theta}_A$. For an infinitesimal rotation, i.e. $\theta_{A1}^f \to 0$ and $\theta_{A2}^f \to 0$,

$$\frac{\partial \mathbf{R}^f}{\partial \theta_{A1}^f} \hat{\mathbf{X}}_A^f \to \begin{pmatrix} 0 & -1 & 0 \end{pmatrix}^T \text{ and } \frac{\partial \mathbf{R}^f}{\partial \theta_{A2}^f} \hat{\mathbf{X}}_A^f \to \begin{pmatrix} 1 & 0 & 0 \end{pmatrix}^T,$$

which yields $D\hat{\mathbf{u}}_1^A = -\mathbf{e}_{A2}^f$ and $D\hat{\mathbf{u}}_2^A = \mathbf{e}_{A1}^f$.

The linearized change of configuration given in Equation (2.47) can thus be written as

$$\Delta x_i = \sum_{A=1}^{nen} N_A \Delta \bar{u}_{Ai} + \sum_{A=1}^{nen} N_A z_A D\hat{u}_{\alpha i}^A \Delta \theta_{A\alpha}^f. \qquad (2.52)$$

By introducing a generalized interpolation matrix $\mathbf{H}^A$, the equation above can be written as follows

$$\Delta \mathbf{x} = \mathbf{H}^A \cdot \Delta \mathbf{d}_A, \qquad (2.53)$$

where

$$\Delta \mathbf{d}_A = \begin{Bmatrix} \Delta \bar{u}_{A1} \\ \Delta \bar{u}_{A2} \\ \Delta \bar{u}_{A3} \\ \Delta \theta_{A1}^f \\ \Delta \theta_{A2}^f \end{Bmatrix} \text{ and } \mathbf{H}^A = \begin{bmatrix} N_A & 0 & 0 & N_A z_A D\hat{u}_{11}^A & N_A z_A D\hat{u}_{21}^A \\ 0 & N_A & 0 & N_A z_A D\hat{u}_{12}^A & N_A z_A D\hat{u}_{22}^A \\ 0 & 0 & N_A & N_A z_A D\hat{u}_{13}^A & N_A z_A D\hat{u}_{23}^A \end{bmatrix},$$

or in a component form as

$$\Delta x_i = H_i^{A\chi} \Delta d_{A\chi}, \quad (i = 1, 2, 3 \text{ and } \chi = 1, 2, \dots 5). \tag{2.54}$$

As $D\hat{\mathbf{u}}_\alpha^A$ is a nonlinear function of $\boldsymbol{\theta}_A$, the interpolation is deformation dependant, which is different from that of a continuum element. The variation of shell configuration due to a virtual nodal displacement is computed in a similar manner as

$$\delta x_i = H_i^{A\chi} \delta d_{A\chi}. \tag{2.55}$$

And the variation of the deformation gradient and Green Lagrangian strain are

$$\delta F_{iI} = \delta x_{i,I} \tag{2.56}$$

and

$$\delta E_{IJ} = \left(\delta x_{k,I} F_{kJ} + F_{kI} \delta x_{k,J} \right) / 2, \tag{2.57}$$

respectively. The linearized variational strain is

$$\Delta \delta E_{IJ} = \left(\delta x_{k,I} \Delta x_{k,J} + \Delta x_{k,I} \delta x_{k,J} \right) / 2. \tag{2.58}$$

2.3.1.4 Force vectors and tangential matrices

In Newton's iteration, the internal virtual work defined in (2.36) is linearized at the current trial solution $\mathbf{d}^*$ as

$$L\left[\delta W^{int} \right]\Big|_{\mathbf{d}^*} = \int_{\Omega_0} \delta E_{IJ} S_{IJ} d\Omega_0 + \int_{\Omega_0} \Delta \delta E_{IJ} S_{IJ} d\Omega_0 + \int_{\Omega_0} \delta E_{IJ} \Delta S_{IJ} d\Omega_0. \tag{2.59}$$

Due to the symmetry of the second Piola-Kirchhoff stress, the first term in (2.59) can be written as

$$\int_{\Omega_0} \delta E_{IJ} S_{IJ} d\Omega_0 = \delta d_{A\chi} \int_{\Omega_0} B_{IJ}^{A\chi} S_{IJ} d\Omega_0,$$

where $B_{IJ}^{A\chi} = H_{k,I}^{A\chi} F_{kJ}$, and the internal force is obtained as

$$f_{A\chi}^{int} = \int_{\Omega_0} B_{IJ}^{A\chi} S_{IJ} d\Omega_0 \, . \tag{2.60}$$

The second term in Equation (2.59) is expanded as follows

$$\int_{\Omega_0} \Delta \delta E_{IJ} S_{IJ} d\Omega_0 = \int_{\Omega_0} \delta x_{k,I} \Delta x_{k,J} S_{IJ} d\Omega_0$$

$$= \delta d_{A\chi} \left(\int_{\Omega_0} H_{k,I}^{A\chi} H_{k,J}^{B\mu} S_{IJ} d\Omega_0 \right) \Delta d_{B\mu}$$

which yields the geometric stiffness

$$K_{A\chi B\mu}^{G} = \int_{\Omega_0} H_{k,I}^{A\chi} H_{k,J}^{B\mu} S_{IJ} d\Omega_0 \, . \tag{2.61}$$

Assume that the material response

$$\Delta S_{IJ} = \mathbb{D}_{IJKL} : \Delta E_{KL} , \tag{2.62}$$

where $\mathbb{D}$ is the tangent material tensor, the last term of (2.59) is expanded as follows

$$\int_{\Omega_0} \delta E_{IJ} \Delta S_{IJ} d\Omega_0 = \int_{\Omega_0} \left(\delta x_{m,I} F_{mJ} \right) \mathbb{D}_{IJKL} \left(\Delta x_{n,K} F_{nL} \right) d\Omega_0$$

$$= \delta d_{A\chi} \left(\int_{\Omega_0} B_{IJ}^{A\chi} \mathbb{D}_{IJKL} B_{KL}^{B\mu} d\Omega_0 \right) \Delta d_{B\mu}$$

which yields the material stiffness

$$K_{A\chi B\mu}^{M} = \int_{\Omega_0} B_{IJ}^{A\chi} \mathbb{D}_{IJKL} B_{KL}^{B\mu} d\Omega_0 \, . \tag{2.63}$$

The external force vector is contributed by the body force and applied surface tractions, which can be written as

$$f_{A\chi}^{ext} = \int_{\Omega_0} H_i^{A\chi} \rho_0 b_i d\Omega_0 + \int_{\Gamma_{t_i}^0} H_i^{A\chi} \bar{t}_i^0 d\Gamma_0 \, . \tag{2.64}$$

Assuming that the external load is independent of the deformation, linearization of the external force is not performed.

The inertial term in Equation (2.34) is complex due to the shell kinematics. Recall that the reference and the current configurations of a shell element are given by (2.37) and (2.39), respectively. The displacement is thus

$$\mathbf{u} = \mathbf{x} - \mathbf{X} = \sum_{A=1}^{nen} N_A \overline{\mathbf{u}}_A + \sum_{A=1}^{nen} N_A z_A \mathbf{R} \cdot \hat{\mathbf{X}}_A ,$$

and the acceleration becomes

$$\ddot{\mathbf{u}} = \sum_{A=1}^{nen} N_A \ddot{\overline{\mathbf{u}}}_A + \sum_{A=1}^{nen} N_A z_A \left(\frac{\partial \mathbf{R}}{\partial \boldsymbol{\theta}} \ddot{\boldsymbol{\theta}} + \dot{\boldsymbol{\theta}} \cdot \frac{\partial^2 \mathbf{R}}{\partial \boldsymbol{\theta}^2} \dot{\boldsymbol{\theta}} \right) \cdot \hat{\mathbf{X}}_A , \tag{2.65}$$

The last term of (2.65) is proportional to the square of the angular velocity, which complicates the solution algorithm, and is usually neglected. The acceleration is then interpolated from nodal quantities based on the same relation for linearized displacement given in (2.54) and it is written in component form as

$$\ddot{u}_i = H_i^{A\chi} \Delta \ddot{d}_{A\chi}, \quad . \tag{2.66}$$

The inertial term in the weak form (2.34) becomes

$$\int_{\Omega_0} \delta u_i \rho_0 \ddot{u}_i d\Omega_0 = \delta d_{A\chi} \left(\int_{\Omega_0} \rho_0 H_i^{A\chi} H_i^{B\mu} d\Omega_0 \right) \Delta \ddot{d}_{B\mu} ,$$

which yields the mass matrix

$$M_{A\chi B\mu} = \int_{\Omega_0} \rho_0 H_i^{A\chi} H_i^{B\mu} d\Omega_0 . \tag{2.67}$$

As the generalized interpolation functions $H_i^{A\chi}$ are deformation dependant, so is the mass matrix. Consistent linearization of this term is necessary when a solution algorithm, e.g. Newmark method, is considered, and the development is presented in the solution algorithm section.

The forces and stiffness can be organized into vector and matrix notations and assembled to form a global linear equation system in the following form

$$\mathbf{f}^{int}\left(\mathbf{d}^*\right) + \mathbf{K}\left(\mathbf{d}^*\right) \cdot \Delta \mathbf{d} = \mathbf{f}^{ext} - \mathbf{M} \cdot \ddot{\mathbf{d}} , \tag{2.68}$$

where $\mathbf{d}^*$ denotes the current trial solution; $\Delta\mathbf{d}$ is the incremental solution to be

determined; $\ddot{\mathbf{d}}$ is nodal acceleration, which is dependant upon the specific time

integration scheme; and $\mathbf{K}$ is the tangential stiffness, which includes both geometrical

and material contribution from (2.61) and (2.63). For static or quasi-static problems, the

inertia term is neglected and the equation system becomes

$$\mathbf{f}^{int}(\mathbf{d}^*) + \mathbf{K}(\mathbf{d}^*) \cdot \Delta\mathbf{d} = \mathbf{f}^{ext}. \tag{2.69}$$

2.3.1.5 Constitutive model

The material properties of fabrics are extremely complex. Nonlinearity,

anisotropy and hysteresis are generally observed and many factors, such as the

constituent yarn properties, the weave patterns, the geometry of yarn structures and the

interactions of interwoven yarns, affect the overall material properties of fabrics. A

detailed study on this subject is presented in Chapter 4. In this chapter, the constitutive

model is considered in the context of the shell formulation and some simplification

assumptions are introduced.

Most shell theories adopt the so-called plane stress condition, which assumes that

the stress normal to a lamina surface, which is defined by fixing ζ in the interpolation

given in Equation (2.37) and (2.39), vanishes. To enforce the constraint, a corotational

lamina basis is usually constructed at each quadrature points such that one base vector

say $\mathbf{e}_3^l$ is always orthogonal to the other two $\mathbf{e}_1^l$ and $\mathbf{e}_2^l$ as shell deforms, and the Cauchy

stress component $\sigma_{33}^l = 0$ is invoked to condense the material tangent moduli. Details

can be found in Hughes et al. [32] and Belytschko et al. [33].

In this work, similar approach is adopted but formulated with a Lagrangian

description. A lamina basis $\mathbf{E}_i^l, (i = 1,2,3)$ is constructed at each quadrature point in the

reference configuration and the plane stress condition is specified in terms of the 2nd

Piola-Kirchhoff stress as $S_{33}^l = 0$, which in general is different from $\sigma_{33}^l = 0$ unless the

lamina normal remains normal after deformation, i.e. $\mathbf{F} \cdot \mathbf{E}_3^l$ coincides with $\mathbf{e}_3^l$. For

fabrics, which are usually quite thin and transverse shear is negligible, the condition $S_{33}^l = 0$ closely enforces the plane stress constraint.

As the shell formulation is based on total Lagrangian description, hyperelastic constitutive models can be naturally incorporated. For hyperelastic materials, a strain energy function $\psi(\mathbf{C})$ exists and the following relation holds

$$\mathbf{S} = 2\frac{\partial \psi(\mathbf{C})}{\partial \mathbf{C}}, \tag{2.70}$$

where $\mathbf{S}$ denotes the 2nd Piola-Kirchhoff stress and $\mathbf{C} = \mathbf{F}^T\mathbf{F}$ is the right Cauchy-Green deformation tensor, which relates to Green strain as $\mathbf{E} = (\mathbf{C} - \mathbf{1})/2$. The material elasticity tensor is defined as

$$\mathbb{D} = 4\frac{\partial^2 \psi}{\partial \mathbf{C}\partial \mathbf{C}}, \tag{2.71}$$

which relates the rate of $\mathbf{S}$ to that of $\mathbf{E}$ as $\dot{\mathbf{S}} = \mathbb{D} : \dot{\mathbf{E}}$.

In this work, St. Venant model, which is a simple extension of linear elasticity, is considered and it is given as follows

$$\mathbf{S} = \mathbb{D} : \mathbf{E} \quad \text{or} \quad S_{IJ} = \mathbb{D}_{IJKL}E_{KL}. \tag{2.72}$$

Since the Green strain $\mathbf{E}$ vanishes in rigid body motion, the constitutive model can be applied to problems with large rotations, which is the case in macroscale fabric modeling. On the other hand, even though the material properties of fabrics are nonlinear, the material model is still valid assuming that under normal wearing condition the strains in clothing fabrics are small and linear. With the assumption, St. Venant model is used as a placeholder for the constitutive model of the macroscale fabric modeling framework.

The St. Venant model includes anisotropy and can be easily incorporated in the nonlinear shell formulation. Using Voigt notation as introduced in Belytschko et al [33], Equation (2.72) can be written in the following form

$$\begin{Bmatrix} S_{11} \\ S_{22} \\ S_{33} \\ S_{23} \\ S_{13} \\ S_{12} \end{Bmatrix} = \begin{bmatrix} D_{11} & D_{12} & D_{13} & D_{14} & D_{15} & D_{16} \\ & D_{22} & D_{23} & D_{24} & D_{25} & D_{26} \\ & & D_{33} & D_{34} & D_{35} & D_{36} \\ & & & D_{44} & D_{45} & D_{46} \\ & sym & & & D_{55} & D_{56} \\ & & & & & D_{66} \end{bmatrix} \begin{Bmatrix} E_{11} \\ E_{22} \\ E_{33} \\ 2E_{23} \\ 2E_{13} \\ 2E_{12} \end{Bmatrix}$$ (2.73)

for fully anisotropic materials. For an orthotropic material, only 9 moduli are independent and the stress-strain relation is

$$\begin{Bmatrix} S_{11} \\ S_{22} \\ S_{33} \\ S_{23} \\ S_{13} \\ S_{12} \end{Bmatrix} = \begin{bmatrix} D_{11} & D_{12} & D_{13} & 0 & 0 & 0 \\ & D_{22} & D_{23} & 0 & 0 & 0 \\ & & D_{33} & 0 & 0 & 0 \\ & & & D_{44} & 0 & 0 \\ & sym & & & D_{55} & 0 \\ & & & & & D_{66} \end{bmatrix} \begin{Bmatrix} E_{11} \\ E_{22} \\ E_{33} \\ 2E_{23} \\ 2E_{13} \\ 2E_{12} \end{Bmatrix}.$$ (2.74)

And the plane stress constraints, as discussed before, can be enforced using the condition $S_{33}^l = 0$.

2.3.1.6 Solution algorithm

Newton's method is applied to solve quasi-static problems (2.69). For a trial solution $\mathbf{d}^*$, the residual is calculated and the incremental displacement is solved. The procedure is summarized in Box.1.

For dynamic problems, the spatially discretized system in form of (2.68) is further discretized in temporal domain using time integration algorithms. A widely used method is the Newmark method, which is stated as follows: Given a solution at time step n as $(\mathbf{d}^n, \mathbf{v}^n, \mathbf{a}^n)$, where $\mathbf{d}$, $\mathbf{v}$ and $\mathbf{a}$ denote nodal vectors of displacement, velocity and acceleration, respectively, the solution at next time step $n+1$ satisfies

$$\mathbf{f}^{int}(\mathbf{d}^{n+1}) = \mathbf{f}^{ext} - \mathbf{M}(\mathbf{d}^{n+1}) \cdot \mathbf{a}^{n+1},$$ (2.75)

where

$$\mathbf{a}^{n+1} = \mathbf{a}^* + \Delta\mathbf{a};$$

$$\mathbf{v}^{n+1} = \mathbf{v}^* + \alpha\Delta t \Delta\mathbf{a}, \ \mathbf{v}^* = \mathbf{v}^n + (1-\alpha)\Delta t \mathbf{a}^n + \alpha\Delta t \mathbf{a}^*; \qquad (2.76)$$

$$\mathbf{d}^{n+1} = \mathbf{d}^* + \beta\Delta t^2 \Delta\mathbf{a}, \ \mathbf{d}^* = \mathbf{d}^n + \Delta t \mathbf{v}^n + (1-2\beta)\frac{\Delta t^2}{2}\mathbf{a}^n + \beta\Delta t^2 \mathbf{a}^*.$$

The internal force is linearized as

$$L\left[\mathbf{f}^{int}\right]_{\mathbf{a}^*} = \mathbf{f}^{int}\left(\mathbf{d}^*\right) + \mathbf{K}\left(\mathbf{d}^*\right)\cdot\beta\Delta t^2 \Delta\mathbf{a} . \qquad (2.77)$$

As the consistent mass matrix is deformation dependent, the inertial force $\mathbf{f}^{ine} = \mathbf{M}(\mathbf{d})\cdot\mathbf{a}$ is linearized about a trial $\mathbf{a}^*$ as

$$L\left[\mathbf{f}^{ine}\right]_{\mathbf{a}^*} = \mathbf{M}\left(\mathbf{d}^*\right)\cdot\mathbf{a}^* + \mathbf{M}\left(\mathbf{d}^*\right)\cdot\Delta\mathbf{a} + \beta\Delta t^2\left(\frac{\partial\mathbf{M}\left(\mathbf{d}^*\right)}{\partial\mathbf{d}}\cdot\mathbf{a}^*\right)\cdot\Delta\mathbf{a} . \qquad (2.78)$$

The external force is assumed to be deformation independent and the linearization is skipped. The linearized equation of (2.75) is

$$\left(\mathbf{M}\left(\mathbf{d}^*\right) + \beta\Delta t^2\mathbf{K}\left(\mathbf{d}^*\right) + \beta\Delta t^2\frac{\partial\mathbf{M}\left(\mathbf{d}^*\right)}{\partial\mathbf{d}}\cdot\mathbf{a}^*\right)\cdot\Delta\mathbf{a} = \mathbf{f}^{ext} - \mathbf{f}^{int}\left(\mathbf{d}^*\right) - \mathbf{M}\left(\mathbf{d}^*\right)\cdot\mathbf{a}^* . \qquad (2.79)$$

By defining an effective tangential operator and residual, the equation is simplified as

$$\tilde{\mathbf{K}}^* \cdot \Delta\mathbf{a} = -\tilde{\mathbf{r}}^* , \qquad (2.80)$$

where

$$\begin{cases} \tilde{\mathbf{K}}^* = \mathbf{M}\left(\mathbf{d}^*\right) + \beta\Delta t^2\mathbf{K}\left(\mathbf{d}^*\right) + \beta\Delta t^2\dfrac{\partial\mathbf{M}\left(\mathbf{d}^*\right)}{\partial\mathbf{d}}\cdot\mathbf{a}^* \\ \tilde{\mathbf{r}}^* = -\mathbf{f}^{ext} + \mathbf{f}^{int}\left(\mathbf{d}^*\right) + \mathbf{M}\left(\mathbf{d}^*\right)\cdot\mathbf{a}^* \end{cases} . \qquad (2.81)$$

The equation is similar to that of a continuum element except for the term $\partial\mathbf{M}/\partial\mathbf{d}$.

Mass lumping is usually adopted to construct a diagonal mass matrix. The motivation is to reduce the computation expense for explicit solution. By setting $\beta = 0$ in Newmark method, the tangential operator in (2.79) consists of only the mass matrix. If the mass matrix is diagonal, the equation system can thus be solved without factorizing the tangential operator. Various mass lumping schemes have been proposed to construct

a diagonal mass matrix, as [32]. In this work, a physical based lumping technique for shell is proposed and it is summarized as follows:

$$M_{\chi\mu} = \begin{cases} \lambda\delta_{\chi\mu}\int_{\Omega_0^e}\rho_0 N_A^2 d\Omega_0^e, & (\chi,\mu=1,2,3) \\ \lambda\delta_{\chi\mu}\dfrac{t^2}{12}\int_{\Omega_0^e}\rho_0 N_A^2 d\Omega_0^e, & (\chi,\mu=4,5) \end{cases} \qquad (2.82)$$

where

$$\lambda = \int_{\Omega_0^e}\rho_0 d\Omega_0^e \Bigg/ \left(\sum_{A=1}^{nen}\int_{\Omega_0^e}\rho_0 N_A^2 d\Omega_0^e\right)$$

and t denotes the shell thickness. As the lumped mass is a constant, no linearization is performed and the effective tangential operator and residual are reduced to

$$\begin{cases} \tilde{\mathbf{K}}^* = \mathbf{M} + \beta\Delta t^2 \mathbf{K}(\mathbf{d}^*) \\ \tilde{\mathbf{r}}^* = -\mathbf{f}^{ext} + \mathbf{f}^{int}(\mathbf{d}^*) + \mathbf{M}\cdot\mathbf{a}^* \end{cases}. \qquad (2.83)$$

---

1. Initialization: set increment count $n=0$ and initial trial solution $\mathbf{d}^n = \mathbf{0}$
2. Solve for load/time increment $n+1$
   a. Form a trial solution $\mathbf{d}^* = \mathbf{d}^n$
   b. Compute residual $\mathbf{r} = \mathbf{f}^{int}(\mathbf{d}^*) - \mathbf{f}^{ext}$
   c. Construct tangential stiffness $\mathbf{K}(\mathbf{d}^*)$
   d. Solve incremental displacement $\Delta\mathbf{d} = -\mathbf{K}(\mathbf{d}^*)^{-1}\cdot\mathbf{r}$
   e. Update the trial $\mathbf{d}^* = \mathbf{d}^* + \Delta\mathbf{d}$
   f. Check convergence:
      ▪ Update residual $\mathbf{r} = \mathbf{f}^{int}(\mathbf{d}^*) - \mathbf{f}^{ext}$
      ▪ If $|\mathbf{r}(\mathbf{d}^*)| \geq RTOL$ then go to 2c.
3. Update solution $\mathbf{d}^{n+1} = \mathbf{d}^*$
4. Set $n=n+1$ and go to 2.

Box 1: Newton's method

In structural dynamics, damping is usually introduced to represent the energy dissipation in a system. A common practice is to add a viscous damping matrix $\mathbf{C}$ into (2.75) and the system reads

$$\mathbf{f}^{int}\left(\mathbf{d}^{n+1}\right)+\mathbf{C}\cdot\mathbf{v}^{n+1}=\mathbf{f}^{ext}-\mathbf{M}\left(\mathbf{d}^{n+1}\right)\cdot\mathbf{a}^{n+1}. \tag{2.84}$$

Rayleigh damping is assumed to be proportional to the mass and stiffness, i.e. $\mathbf{C}=a\mathbf{M}+b\mathbf{K}$. In general, realistic damping is related to the material properties and the damping matrix should be derived based on the constitutive model adopted. For example, Rayleigh damping can be derived from a Kelvin-Voigt viscoelastic constitutive model for linear problems as illustrated by Hughes in [32]. In this work, Rayleigh damping is adopted as a placeholder before a fabric constitutive model with realistic dissipation feature is available. A modification is that the damping is assumed to be proportional to the material stiffness part $\mathbf{K}_M$ only and the geometrical part $\mathbf{K}_G$ is not damped. In addition, the mass matrix and material stiffness matrix are assumed to be fixed based on the converged solution of the previous time step and are not linearized in the current solution phase. The damping matrix is given as $\mathbf{C}=a\mathbf{M}+b\mathbf{K}_M\left(\mathbf{d}^n\right)$ and the effective tangential operator and residual in (2.74) are given as follows

$$\begin{cases}\tilde{\mathbf{K}}^*=\mathbf{M}+\beta\Delta t^2\mathbf{K}\left(\mathbf{d}^*\right)+\alpha\Delta ta\mathbf{M}+\alpha\Delta tb\mathbf{K}_M\left(\mathbf{d}^n\right)\\\tilde{\mathbf{r}}^*=\mathbf{f}^{ext}-\mathbf{f}^{int}\left(\mathbf{d}^*\right)-\mathbf{M}\cdot\mathbf{a}^*-a\mathbf{M}\cdot\mathbf{v}^*-b\mathbf{K}_M\left(\mathbf{d}^n\right)\cdot\mathbf{v}^*\end{cases}. \tag{2.85}$$

Various assumptions on mass, damping and linearization yield various effective tangential operators and residual vectors as given in (2.81), (2.83) and (2.85). The linearized equation (2.80) is then solved in the framework of the Newmark method, which is outlined in Box 2.

The stability conditions of the Newmark method are considered and they constraint the maximum allowable time step for time integration. A detailed discussion on the subject is presented by Hughes [32]. For central difference time integration, i.e. $\alpha=1/2$ and $\beta=0$, the critical time step is given by

$$\Delta t_{crit} \le \frac{2}{\omega_{max}^h} \,. \tag{2.86}$$

ω_{max}^h is bounded by the maximum frequency of the individual elements and an estimate is given by

$$\omega_{max}^h = \frac{2c}{h}, \tag{2.87}$$

where h is the element dimension and $c = \sqrt{E/\rho}$ is the bar-wave velocity, in which E is Young's modulus and ρ is density.

---

1. Initialization: set increment count $n=0$ and initial state $\mathbf{d}^0$, $\mathbf{v}^0$ and $\mathbf{a}^0$
2. Solve for load/time increment $n+1$
    a. Form predictors
        $$\mathbf{a}^* = \mathbf{0}$$
        $$\mathbf{v}^* = \mathbf{v}^n + (1-\alpha)\Delta t \mathbf{a}^n + \alpha \Delta t \mathbf{a}^*$$
        $$\mathbf{d}^* = \mathbf{d}^n + \Delta t \mathbf{v}^n + (1-2\beta)\frac{\Delta t^2}{2}\mathbf{a}^n + \beta \Delta t^2 \mathbf{a}^*$$
    b. Compute residual $\tilde{\mathbf{r}}^*$
    c. Construct tangential stiffness $\tilde{\mathbf{K}}^{**}$
    d. Solve incremental displacement
        $$\Delta \mathbf{a} = -\left(\tilde{\mathbf{K}}^*\right)^{-1} \cdot \tilde{\mathbf{r}}^*$$
    e. Update predictors
        $$\mathbf{a}^* = \mathbf{a}^* + \Delta \mathbf{a}; \, \mathbf{v}^* = \mathbf{v}^* + \alpha \Delta t \Delta \mathbf{a}; \, \mathbf{d}^* = \mathbf{d}^* + \beta \Delta t^2 \Delta \mathbf{a}$$
    f. Check convergence:
        - Update residual $\tilde{\mathbf{r}}^*$
        - If $\left|\tilde{\mathbf{r}}^*\right| \ge RTOL$ then go to 2c.
3. Update solution $\mathbf{a}^{n+1} = \mathbf{a}^*$, $\mathbf{v}^{n+1} = \mathbf{v}^*$, $\mathbf{d}^{n+1} = \mathbf{d}^*$
4. Set $n = n+1$ and go to 2.

Box 2: Newmark method

2.3.2 Test problems

The shell element developed above has been tested with some benchmark

problems and the results are summarized here.

2.3.2.1 Clamped square elastic plate with point load

A square plate of thickness $t = 0.1m$ is modeled in quarter-symmetry. A point

load is applied at the center of the plate. An exact analytical solution using thin plate

theory gives the vertical deflection at the plate center as

$$\delta_c = -\frac{0.611b^2 P}{Et^3} \rightarrow -5.60 \times 10^{-3} m$$

where $E = 1.092 Mpa$, $P = 1N$, $b = 10m$ is the edge length. The plate is modeled by 64

shell elements and the result is $-5.62 \times 10^{-3} m$. The deformation is shown in Fig.10a.

(a) Clamped square plate problem

(b) Beam "roll-up" problem
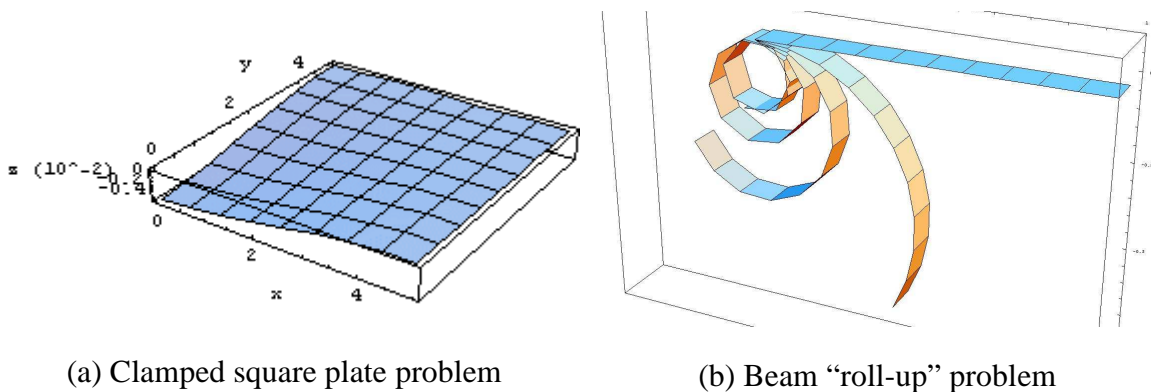
Figure 10: Test problems for the shell element

2.3.2.2 "Roll-up" problem

In this problem, a cantilever beam modeled by the shell element is rolled up by a

monotonically increasing rotational angle prescribed on the free end. The resultant

moment is monitored and it is compared well with the analytical solution. Circular curvature is observed in the deformed configuration as shown in Fig.10b.

<u>2.4 Particle methods vs. finite element methods</u>

Two alternative macroscale fabric modeling techniques have been implemented and tested in our clothing modeling framework: The first is a particle-based method that starts directly with a discrete representation of fabric as a system of mass points and springs. The second is based on finite element methods, where the local equilibrium conditions and constitutive relations are employed as a point of depart. Although the two techniques boil down to similar global equation systems in terms of nodal forces and displacements, the difference in their specifications on discretization implies distinct mechanics phenomena.

In essence, with particle methods fabric is treated as a fish-net, while with finite element methods the contribution from the entire surface is considered. Consequently, for particle methods, as the spatial "fish-net" discretization of a garment is refined, the masses and spring stiffness must be adjusted accordingly, and this is not necessarily a trivial matter when dealing with fabric patches of irregular shape and size. The vague physical meaning of spring stiffness in particle methods also makes it difficult to translate between fabric spring forces in such models and the actual stress level in the fabric being modeled. Ad-hoc assumptions need to be made to answer these types of questions.

Finite element methods follow a more rigorous mathematical development by considering the local equilibrium conditions and constitutive relations. The global discrete system is derived using the well-defined Galerkin approximation, where the solution space is approximated by the linear combination of nodal shape functions. The nodal force and displacement relation in the discretized model is derived by exact spatial integration of the local constitutive relations. The physical significance of the spatial integration is that the nodal forces include the contribution of the entire surface or domain

rather than the vaguely-defined "fishnet" representation. Moreover, as the spatial integration explicitly defines the relation between the local constitutive behaviors and the global nodal forces, the fabric stresses and strains can be handled more rigorously and straightforwardly than in particle models. On the other hand, since finite element methods are continuously performing spatial integrations of stresses and strains, such methods are more computationally intensive than particle methods, which do not require any spatial integration at all.

Depending on the objective, both techniques can be applied to macroscale fabric modeling. As illustrated in Fig.8, by experimenting with the spring stiffness and mass properties in a particle model, simulations of clothing that appear visually realistic can be achieved. However, if the objective of the modeling is to realistically quantify the mechanical resistance that the clothing exerts on the wearer, visual realism alone will not be sufficient. For this reason, the continuum degenerated shell formulation implemented and tested in the current framework is somewhat more attractive to the authors. Specifically, one can insert realistic constitutive material models for fabrics into the continuum shell framework, thereby increasing the likelihood of calculating more realistic mechanical resistance parameters. Indeed, mechanical realism is paramount in a clothing modeling framework used in designing protective systems for defense and security applications.

It is arguable that fabrics possess discrete mesoscale yarn structures and that it is not appropriate to model fabrics using degenerated shell theory, which assumes material continuity and models the bending behavior by integration through the thickness. This argument could well be true and deserves further investigation. However, the advantage of finite element methods is their unambiguous specification on the discretization scheme, which is required when realistic material responses are being investigated. The material discontinuity issue, if it were indeed a problem, can be treated by appropriate constitutive models and/or resultant shell formulations.

CHAPTER 3

CONTACT COMPUTATION

A major component in fabric/clothing modeling is contact computation, which enforces the impenetrability and friction constraints associated with contact surfaces and calculates the mutual tractions between them. In fabric/clothing modeling, contact problems can be found on both macroscale and mesoscale. On the macroscale, clothing cannot penetrate the skin of a wearer and it interacts with the wearer by exerting tractions on the contact surface. On the mesoscale, many fabrics are structures of interwoven yarns and the interactions between contacting yarns significantly affect the overall mechanical properties of the fabrics. Contact computation is thus needed on both scales for the fabric modeling framework.

In this chapter, contact computation approaches utilized in this study are discussed. A general formulation for multi-body contact problems is presented first. The kinematics of contact surfaces and the contact constraints, such as impenetrability and friction, are introduced and regularization techniques to enforce these constraints are described. Then details on contact computation for the fabric modeling framework are presented. Since the foci of the macroscale and mesoscale contact computations are slightly different, they employ different solution approaches. An explicit approach is developed to solve the macroscale contact problem, where the whole framework is based on a dynamic shell formulation and robustness is the major concern. An implicit approach is adopted for the study of mesoscale yarn interactions, where quasi-static responses of the model are the main focus.

Another topic associated with contact computation is collision detection, which in general, detects penetration between two surfaces. Depending on the specific surface descriptions, the cost for collision detection varies. In finite element computation, where surfaces are usually described as meshes composed of quadrilaterals and triangles, the

collision detection can be expensive. Some surfaces can alternatively be defined as scalar functions of spatial coordinates, i.e. implicit surface. The cost for collision detection with implicit surfaces is much lower but the tradeoff is that these surfaces are relatively simple and may not be able to realistically represent complex shapes. Efficient collision detection still remains its own challenge and an active research topic, e.g. [36,37]. It is thus not pursued in this study, and instead, standard collision detection techniques are adopted as placeholders. However, the idea of using implicit surfaces is explored here to make the macroscale contact computation more affordable.

3.1 Contact computation

3.1.1 Problem statement

To keep the discussion general, contact between multiple deformable bodies is considered. Special cases, such as the rigid obstacle problem, where a deformable body interacts with a rigid surface, and the self-contact problem, where different portions of a deformable body interact, can be readily included in this formulation. The discussion here follows mostly Laursen and Simo's work [38].

Consider two deformable bodies, denoted in their respective reference configurations by $\Omega_0^{(i)} \subset \mathbb{R}^{nsd}$, where *nsd* denotes the number of spatial dimensions and the superscript $i = 1, 2$ indicates one of the two bodies. Subsequent configurations in a time interval $[0, T]$ are given by mapping $\boldsymbol{\varphi}^{(i)} : \Omega^{(i)} \times [0, T] \rightarrow \mathbb{R}^{nsd}$. The motions of the two bodies are given by $\boldsymbol{\varphi}^{(i)}(\bullet, t)$. At any time instant $t \in [0, T]$ the configurations can be denoted as $\boldsymbol{\varphi}_t^{(i)}, (i = 1, 2)$. For a material point $\mathbf{X} \in \Omega_0^{(i)}$, its spatial counterpart at *t* is given by $\mathbf{x} = \boldsymbol{\varphi}_t^{(i)}(\mathbf{X})$. Assume that a pair of potential contact boundaries is designated $\Gamma^{(1)} \subset \partial\Omega_0^{(1)}$ and $\Gamma^{(2)} \subset \partial\Omega_0^{(2)}$, which includes all material points where contact might occur. The current positions of the contact boundaries are given by $\gamma^{(i)} = \boldsymbol{\varphi}_t^{(i)}\left(\Gamma^{(i)}\right)$, $(i = 1, 2)$.

The equilibrium of each body is governed by the same local equations for a single body as those given in Chapter 2. For body i, the equations are summarized as follows:

$$\left.\begin{array}{c} P_{kJ,J}^{(i)} + \rho_0^{(i)}b_k^{(i)} = \rho_0^{(i)}\ddot{u}_k^{(i)} \text{ in } \Omega_0^{(i)} \\ P_{kJ}^{(i)}N_J^{(i)} = \overline{t}_k^{(i)} \text{ on } \Gamma_t^{(i)} \\ u_k^{(i)} = \overline{u}_k^{(i)} \text{ on } \Gamma_u^{(i)} \end{array}\right\}, \quad (i \text{ not summed}) \quad (3.1)$$

where $P_{kJ}^{(i)}$ is the 1$^{\text{st}}$ Piola-Kirchhoff stress in body i; $\Gamma_t^{(i)}$ and $\Gamma_u^{(i)}$ denote the natural boundary and the essential boundary of the body, respectively. In addition, tractions also develop on the contact boundaries $\Gamma^{(i)}$ when the two bodies are in contact and interact with each other.

By introducing an admissible variation of the configuration $\delta\boldsymbol{\varphi}^{(i)} \in \mathcal{U}^{(i)}$ for each body i, with $\mathcal{U}^{(i)}$ consisting all smooth admissible variations which vanish on the essential boundaries, (i.e. $\delta\boldsymbol{\varphi}^{(i)} = \mathbf{0}$ on $\Gamma_u^{(i)}$), and by integrating the product of the variation and $(3.1)_1$ over $\Omega_0^{(i)}$, the weak form of each body i can be derived following integration by parts as follows:

$$\delta W^{(i)}\left(\boldsymbol{\varphi}_t^{(i)}, \delta\boldsymbol{\varphi}^{(i)}\right) = \delta W_{int}^{(i)} - \delta W_{ext}^{(i)} + \delta W_{ine}^{(i)} = \delta W_{cnt}^{(i)} \quad (3.2)$$

with

$$\delta W_{int}^{(i)} = \int_{\Omega_0^{(i)}} \delta\varphi_{k,J}^{(i)} P_{kJ}^{(i)} d\Omega_0^{(i)}, \text{ internal virtual work;}$$

$$\delta W_{ext}^{(i)} = \int_{\Omega_0^{(i)}} \delta\varphi_k^{(i)} \rho_0^{(i)} b_k^{(i)} d\Omega_0^{(i)} + \int_{\Gamma_t^{(i)}} \delta\varphi_k^{(i)} \overline{t}_k^{(i)} d\Gamma_t^{(i)}, \text{ external virtual work;}$$

$$\delta W_{ine}^{(i)} = \int_{\Omega_0^{(i)}} \delta\varphi_k^{(i)} \rho_0^{(i)} \ddot{u}_k^{(i)} d\Omega_0^{(i)}, \text{ inertial virtual work;}$$

$$\delta W_{cnt}^{(i)} = \int_{\Gamma^{(i)}} \delta\varphi_k^{(i)} \overline{t}_k^{(i)} d\Gamma^{(i)}, \text{ contact virtual work.}$$

$\delta W^{(i)}\left(\boldsymbol{\varphi}_t^{(i)}, \delta\boldsymbol{\varphi}^{(i)}\right)$ is the sum of internal virtual work and the virtual work due to inertial forces minus the external virtual work and it should vanish if no contact tractions exist as was true for the single body case in Chapter 2. For contact problems, the total virtual work $\delta W^{(i)}\left(\boldsymbol{\varphi}_t^{(i)}, \delta\boldsymbol{\varphi}^{(i)}\right)$ is equal to the virtual work done by the contact tractions on

boundary $\Gamma^{(i)}$, $\delta W_{cnt}^{(i)}$. Equation (3.2) must therefore hold for each body i at any instant of time t.

The weak equilibrium condition of two bodies in contact is obtained by combining (3.2) for both bodies and is written as:

$$\delta W\left(\boldsymbol{\varphi}_t, \delta\boldsymbol{\varphi}\right) = \delta W^{(1)}\left(\boldsymbol{\varphi}_t^{(1)}, \delta\boldsymbol{\varphi}^{(1)}\right) + \delta W^{(2)}\left(\boldsymbol{\varphi}_t^{(2)}, \delta\boldsymbol{\varphi}^{(2)}\right)$$
$$= \int_{\Gamma^{(1)}} \delta\boldsymbol{\varphi}^{(1)} \cdot \overline{\mathbf{t}}^{(1)} d\Gamma^{(1)} + \int_{\Gamma^{(2)}} \delta\boldsymbol{\varphi}^{(2)} \cdot \overline{\mathbf{t}}^{(2)} d\Gamma^{(2)} \ ,$$
(3.3)

the right hand side represents the contact virtual work integrated over the contact boundary $\Gamma^{(1)}$ and $\Gamma^{(2)}$. The notation $\boldsymbol{\varphi}_t$ indicates the collection of $\boldsymbol{\varphi}_t^{(i)}, (i = 1, 2)$ and likewise for $\delta\boldsymbol{\varphi}$. Considering the fact that $\overline{\mathbf{t}}^{(2)} d\Gamma^{(2)} = -\overline{\mathbf{t}}^{(1)} d\Gamma^{(1)}$ at the contact point, the right hand side of Equation (3.3) can be combined as a single integral over one surface and Equation (3.3) can be written as

$$\delta W\left(\boldsymbol{\varphi}_t, \delta\boldsymbol{\varphi}\right) + \delta W_C\left(\boldsymbol{\varphi}_t, \delta\boldsymbol{\varphi}\right) = 0 \ ,$$
(3.4)

where

$$\delta W_C\left(\boldsymbol{\varphi}_t, \delta\boldsymbol{\varphi}\right) = -\int_{\Gamma^{(1)}} \overline{\mathbf{t}}^{(1)} \cdot \left(\delta\boldsymbol{\varphi}^{(1)} - \delta\boldsymbol{\varphi}^{(2)}\right) d\Gamma^{(1)}$$
(3.5)

Utilizing the arbitrariness of the variation $\delta\boldsymbol{\varphi}$, Equation (3.4) can be solved for $\boldsymbol{\varphi}_t$ provided that the contact traction $\overline{\mathbf{t}}^{(1)}$ is known.

The key to contact computation is determination of the contact boundary and the contact traction $\overline{\mathbf{t}}^{(1)}$, which are both unknown prior to solving the problem. The traction is determined by considering the impenetrability and friction constraints of the contact boundaries $\gamma^{(i)}, (i = 1, 2)$.

3.1.2 Frictionless contact problems

For frictionless contact, the contact traction involves only the normal component and it can be written as

$$\overline{\mathbf{t}}^{(1)} = t_N \mathbf{n} \ ,$$
(3.6)

where $\mathbf{n}$ denotes the inward normal to the surface $\gamma^{(1)}$ and t_N depends on the interpenetration of the two bodies. It should be noted that as a point of contact, the inward normal to $\gamma^{(1)}$ coincides with the outward normal of $\gamma^{(2)}$.

3.1.2.1 Impenetrability constraint

In the contact computation literature, a contact pair is usually designated as a slave surface $\Gamma^{(1)}$ and a master surface $\Gamma^{(2)}$, and the impenetrability constraint is enforced such that no material point on the slave surface, i.e. $\mathbf{X} \in \Gamma^{(1)}$, is allowed to penetrate any part of the master surface $\gamma^{(2)} = \boldsymbol{\varphi}_t^{(2)}\left(\Gamma^{(2)}\right)$ at any time t. The master-slave designation does introduce bias by allowing master nodes to penetrate the slave surface. However, this unsymmetrical behavior can be eliminated by alternating the roles of master and slave of the surfaces.

The penetration is usually quantified by identifying the closest projection point of a slave node onto the penetrated master surface. For example, in [38] the penetration is defined by a gap function as follows:

$$g\left(\mathbf{X}_s, t\right) = \text{sign}\left(g\left(\mathbf{X}_s, t\right)\right)\left|g\left(\mathbf{X}_s, t\right)\right|, \tag{3.7}$$

where

$$\left|g\left(\mathbf{X}_s, t\right)\right| = \min_{\mathbf{X}_m \in \Gamma^{(2)}} \left\|\boldsymbol{\varphi}^{(1)}\left(\mathbf{X}_s, t\right) - \boldsymbol{\varphi}^{(2)}\left(\mathbf{X}_m, t\right)\right\| \tag{3.8}$$

and

$$\text{sign}\left(g\left(\mathbf{X}_s, t\right)\right) = \begin{cases} -1, & \text{if } \boldsymbol{\varphi}^{(1)}\left(\mathbf{X}_s, t\right) \text{ is admissible;} \\ 1, & \text{otherwise.} \end{cases}$$

For any point $\mathbf{X}_s \in \Gamma^{(1)}$, the point $\mathbf{X}_m \in \Gamma^{(2)}$ achieving the minimum, which is denoted by $\bar{\mathbf{X}}_m$, is obtained by finding the closest projection of $\mathbf{x}_s = \boldsymbol{\varphi}_t^{(1)}\left(\mathbf{X}_s\right)$ onto $\gamma^{(2)}$. Since the identification of $\bar{\mathbf{X}}_m$ depends implicitly on the material point $\mathbf{X}_s$ and time t, it can be written as $\bar{\mathbf{X}}_m = \bar{\mathbf{X}}_m\left(\mathbf{X}_s, t\right)$. The gap function can be rewritten as follows

$$g\left(\mathbf{X}_{s},t\right)=-\left[\boldsymbol{\varphi}^{(1)}\left(\mathbf{X}_{s},t\right)-\boldsymbol{\varphi}^{(2)}\left(\overline{\mathbf{X}}_{m}\left(\mathbf{X}_{s},t\right),t\right)\right]\cdot\mathbf{n}\,,\tag{3.9}$$

where $\mathbf{n}$ is the outward normal to $\gamma^{(2)}$ at the material point $\overline{\mathbf{X}}_{m}$. The impenetrability constraint is mathematically stated as

$$g\left(\mathbf{X}_{s},t\right)\le0\,.\tag{3.10}$$

Since the contact surfaces are usually not bonded and free to separate, no tensile normal contact traction is permitted, which yields the condition

$$t_{N}\left(\mathbf{X}_{s},t\right)\ge0\,.\tag{3.11}$$

The normal contact traction depends on the interpenetration of the two bodies. When $t_{N}>0$, no penetration is allowed and $g=0$; while when $g<0$, i.e. the two bodies are not in contact, there is no contact traction and $t_{N}=0$. This relationship can be summarized as follows

$$t_{N}\left(\mathbf{X}_{s},t\right)g\left(\mathbf{X}_{s},t\right)=0\,.\tag{3.12}$$

In addition, a persistency condition is written as

$$t_{N}\left(\mathbf{X}_{s},t\right)\dot{g}\left(\mathbf{X}_{s},t\right)=0\,,\tag{3.13}$$

which implies that when the two bodies interact, i.e. $t_{N}>0$, the change of the penetration remains zero, i.e. $\dot{g}=0$. The equations (3.10)~(3.13) are usually called the Kuhn-Tucker conditions for normal contact and the normal contact traction magnitude can be determined from them.

According to the gap function expression given in (3.9), it can be verified as in [38] that for a variation in configuration $\delta\boldsymbol{\varphi}$, the variational penetration is

$$\delta g=-\mathbf{n}\cdot\left(\delta\boldsymbol{\varphi}^{(1)}\left(\mathbf{X}_{s}\right)-\delta\boldsymbol{\varphi}^{(2)}\left(\overline{\mathbf{X}}_{m}\right)\right),\tag{3.14}$$

which when substituted in (3.5) and combined with (3.6) yields a compact form for the contact virtual work as follows

$$\delta W_{C}\left(\varphi_{t},\delta\boldsymbol{\varphi}\right)=\int_{\Gamma^{(1)}}t_{N}\delta g\,d\Gamma^{(1)}\,.\tag{3.15}$$

3.1.2.2 Discretization

In finite element computation, the surfaces are usually discretized as meshes and the discrete forms of the gap function (3.9) are thus considered. For example, a master surface can be represented by a mesh of quadrilaterals. Assume that each quadrilateral or *segment*, a term commonly adopted in the literature of contact computation, is defined by bi-linear isoparametric mapping as

$$\mathbf{x}_m = \sum_{I=1}^{4} N_I(\boldsymbol{\xi})\,\mathbf{x}_{mI}\,,\qquad(3.16)$$

where $\boldsymbol{\xi} = \left(\xi^1, \xi^2\right)$ denotes the natural coordinates bounded as $\xi^1, \xi^2 \in [-1,1]$ and $N_I(\boldsymbol{\xi})$ is the nodal interpolation function

$$N_I(\boldsymbol{\xi}) = \frac{1}{4}\left(1 + \xi_I^1 \xi^1\right)\left(1 + \xi_I^2 \xi^2\right).\qquad(3.17)$$

According to (3.16), the closest projection point $\bar{\mathbf{x}}_m = \boldsymbol{\varphi}^{(2)}\left(\bar{\mathbf{X}}_m\right)$ can then be interpolated as

$$\bar{\mathbf{x}}_m = \sum_{I=1}^{4} N_I\left(\bar{\boldsymbol{\xi}}\right)\mathbf{x}_{mI}\,,\qquad(3.18)$$

where $\bar{\boldsymbol{\xi}}$ denotes the natural coordinates of the projection point. $\bar{\boldsymbol{\xi}}$ in general is a function of the current configuration $\boldsymbol{\varphi}_t$ and in the discrete setting it depends on the current positions of the slave node and associated master nodes. The details on the determination of $\bar{\boldsymbol{\xi}}$ are presented in Section 3.2.1.

With the discretization, the gap function can be written as

$$g = -\mathbf{N}_e^T \cdot \mathbf{x}^e\,,\qquad(3.19)$$

where

$$\mathbf{N}_e = \begin{bmatrix} \mathbf{n} \\ -N_1(\overline{\xi})\mathbf{n} \\ -N_2(\overline{\xi})\mathbf{n} \\ -N_3(\overline{\xi})\mathbf{n} \\ -N_4(\overline{\xi})\mathbf{n} \end{bmatrix} \text{ and } \mathbf{x}^e = \begin{bmatrix} \mathbf{x}_s \\ \mathbf{x}_{m1} \\ \mathbf{x}_{m2} \\ \mathbf{x}_{m3} \\ \mathbf{x}_{m4} \end{bmatrix}, \tag{3.20}$$

Likewise, the variation of the gap function in discrete form reads as

$$\delta g = -\mathbf{N}_e^T \cdot \delta \mathbf{\Phi}^e \tag{3.21}$$

where $\delta \mathbf{\Phi}^e$ denotes the nodal variation

$$\delta \mathbf{\Phi}^e = \begin{bmatrix} \delta \boldsymbol{\varphi}^{(1)}(\mathbf{X}_s) \\ \delta \boldsymbol{\varphi}^{(2)}(\mathbf{X}_{m1}) \\ \delta \boldsymbol{\varphi}^{(2)}(\mathbf{X}_{m2}) \\ \delta \boldsymbol{\varphi}^{(2)}(\mathbf{X}_{m3}) \\ \delta \boldsymbol{\varphi}^{(2)}(\mathbf{X}_{m4}) \end{bmatrix}.$$

A schematic of the impenetrability condition for bilinear master segment interpolation is shown in Fig.11.
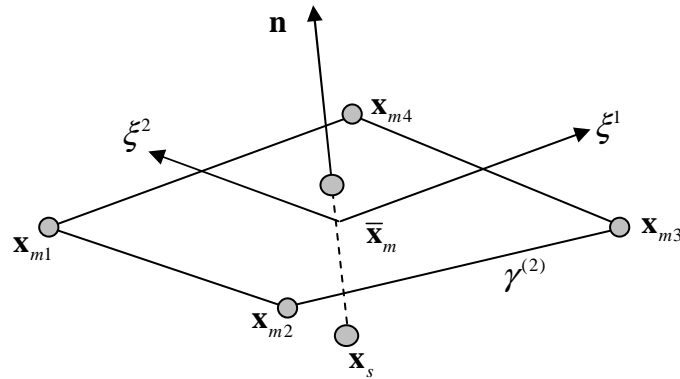
Figure 11: A schematic of the impenetrability constraint for a bilinearly interpolated quadrilateral

Each slave node and the master segment it penetrates can be treated as a contact element and the contact virtual work given in (3.15) is calculated as a sum of contributions from all the contact elements as

$$\delta W_C = \sum_e \delta W_C^e \quad \text{with} \quad \delta W_C^e = \int_{\Gamma_e^{(1)}} t_N \delta g \, d\Gamma_e^{(1)} \,, \tag{3.22}$$

where $\Gamma_e^{(1)}$ is the domain associated with a slave node. For each element, if it is assumed that t_N is known, a contact force vector can be constructed by invoking the arbitrariness of $\delta \boldsymbol{\Phi}_e$ as

$$\mathbf{f}_e^{cnt} = -\int_{\Gamma_e^{(1)}} t_N \mathbf{N}_e \, d\Gamma_e^{(1)} \,. \tag{3.23}$$

Since the vector $\mathbf{N}_e$ depends on the configuration through the identification of $\bar{\xi}$ and $\mathbf{n}$, the contact force vector is a function of both configuration and t_N. A global contact force vector can be constructed by assembling the contribution from each element as

$$\mathbf{f}^{cnt} = \mathbb{A}_e \left(\mathbf{f}_e^{cnt} \right). \tag{3.24}$$

Likewise, by assembling the gap function (3.19) for each contact element as a vector, the impenetrability constraint in discrete form can be written as

$$\mathbf{g} = \mathbf{G} \cdot \mathbf{x} \leq \mathbf{0}, \tag{3.25}$$

where $\mathbf{x} = \mathbf{d} + \mathbf{X}$ is the updated nodal position vector and

$$\mathbf{G} = \mathbb{A}_e \left(-\mathbf{N}_e^T \right) \tag{3.26}$$

is usually called contact constraint matrix, which is assembled from the vector $\mathbf{N}_e$ given in (3.20) for each contact element. Since $\mathbf{N}_e$ depends on the updated nodal position through the identification of $\bar{\xi}$, the contact constraint matrix is a function of $\mathbf{d}$, i.e. $\mathbf{G} = \mathbf{G}(\mathbf{d})$.

3.1.2.3 Penalty formulation

In penalty formulation, a penalty parameter ε_N is introduced to penalize a violated constraint. The normal traction is assumed to be

$$t_N = \varepsilon_N \left\langle g \right\rangle, \tag{3.27}$$

where $\left\langle \circ \right\rangle = \left(\circ + \left| \circ \right| \right)/2$ is the Macauley bracket function. For an admissible position, i.e. $g \le 0$, $t_N = 0$. While when $g > 0$, where a penetration occurs, a penalty normal traction $t_N = \varepsilon_N g > 0$ is applied to push the penetrating pair apart. Compared to the Kuhn-Tucker conditions, the penalty method is exact only when $\varepsilon_N \to \infty$. For a finite penalty parameter, penetration is allowed.

The advantage of the penalty formulation is that since the normal contact traction t_N is a function of deformation as indicated by (3.27), the only unknown in (3.4) is $\boldsymbol{\varphi}_t$. By introducing a finite element discretization and considering the arbitrariness of $\delta\boldsymbol{\varphi}$, a nonlinear equation system in terms of the nodal displacement vector $\mathbf{d}$ can be derived as follows:

$$\mathbf{f}^{int}\left(\mathbf{d}\right) + \mathbf{M} \cdot \mathbf{a} + \mathbf{f}^{cnt}\left(\mathbf{d}\right) = \mathbf{f}^{ext}, \tag{3.28}$$

where $\mathbf{f}^{cnt}$ is a force vector contributed by contact traction and $\mathbf{a} = \ddot{\mathbf{d}}$ is the nodal acceleration vector. For simplicity, the external force and the mass matrix above are assumed to be deformation independent. The nonlinear system of equations can be solved by the Newton's method or some variation thereof. For dynamic problems, the accelerations can be integrated by a Newmark time integration scheme. Consistent linearization of the contact forces is needed for implicit solution methods and some development on this issue is presented in [38,39].

3.1.2.4 Lagrange multiplier methods

Instead of assuming that normal contact tractions are functionally dependent on the penetration as is done in penalty formulations, Lagrange multiplier methods treat the

traction t_N as an unknown independent of the deformation $\boldsymbol{\varphi}_t$. The unknown is usually

denoted as a Lagrange multiplier λ_N. By assembling the Lagrange multiplier for each

contact element as a vector $\boldsymbol{\lambda}$, the discrete equilibrium equation can be written as follows

$$\mathbf{f}^{int}\left(\mathbf{d}\right)+\mathbf{M}\cdot\mathbf{a}+\left[\mathbf{G}\left(\mathbf{d}\right)\right]^{T}\cdot\boldsymbol{\lambda}=\mathbf{f}^{ext}, \tag{3.29}$$

where $\mathbf{G}$ is given by (3.26). The operation $\mathbf{G}^{T}\cdot\boldsymbol{\lambda}$ distributes the Lagrange multipliers

λ_N to the associated master and slave nodes and yields an equivalent nodal force vector

due to contact.

As the Lagrange multipliers introduce additional unknowns to the system of

(3.29), the impenetrability constraint (3.25) is considered to augment the system. A slave

node can either be in contact with the master surface, which corresponds to the equality

constraint $g=0$, or free from contact, which corresponds to the inequality constraint

$g<0$. Assuming that the set of the slave nodes in contact is available, (i.e. those with

equality constraint activated), the impenetrability constraint given in Equation (3.25) is

equivalent to the following discrete equality constraint

$$\mathbf{G}\left(\mathbf{d}\right)\cdot\mathbf{x}=\mathbf{0}. \tag{3.30}$$

Given $\overline{\boldsymbol{\xi}}$, Equation (3.30) literally projects a slave node from its penetrating position $\mathbf{x}_s$

to $\overline{\mathbf{x}}_m$, and the procedure can be conceptually written as $\overline{\mathbf{x}}_m = proj\left(\mathbf{x}_s\right)$.

To determine the active slave node set, a trial-and-error procedure is usually

adopted. By assuming an initial trial set and constructing $\mathbf{G}$ based on the trial, Equations

(3.29) and (3.30) are solved simultaneously for the nodal displacements and the Lagrange

multipliers. If a Lagrange multiplier is negative, which indicates a tensile traction

developed at the slave node, the slave node is removed from the active set. A new

computation is restarted with the modified active slave node set. The trial-and-error

procedure iterates until both the equilibrium conditions and the impenetrability

constraints are satisfied.

3.1.3 Frictional contact

Friction usually exists between contact surfaces and in general the tangential components of contact tractions are nonzero. The frictional traction depends on the relative motion of the contact surfaces. Static friction occurs when there is no relative motion between the two surfaces while kinetic friction occurs when the surfaces slide against each other. Friction laws are formulated to describe the relationships of the frictional traction and the relative motion of the contact surfaces. A simple example is the Coulomb friction law, where the static friction is assumed to be bounded by a critical value and the kinetic friction is proportional to the magnitude of the normal traction with its direction opposite to the slip direction.

In this work, the frictional contact formulation proposed by Simo and Laursen [38] is adopted. In their formulation, a convected basis is constructed to describe the frictional traction and the slip rate and the friction law is frame indifferent. Their work is based on a continuum framework and can be readily extended for a spatial discretization.

3.1.3.1 Surface parametrization and convected basis

The contact surfaces $\Gamma^{(i)}$ and $\gamma^{(i)}, (i=1,2)$ can be parameterized as follows

$$\Gamma^{(i)} = \mathbf{\Psi}_0^{(i)}\left(\mathcal{A}^{(i)}\right) \text{ and } \gamma^{(i)} = \mathbf{\Psi}_t^{(i)}\left(\mathcal{A}^{(i)}\right),\tag{3.31}$$

where $\mathcal{A}^{(i)} \subset \mathbb{R}^{nsd-1}$ and $\mathbf{\Psi}_t^{(i)} = \boldsymbol{\varphi}_t^{(i)} \circ \mathbf{\Psi}_0^{(i)}$ with $\circ$ denoting composition. According to the parametrization, for any point $\mathbf{X}_m \in \Gamma^{(2)}$, one has $\mathbf{X}_m = \mathbf{\Psi}_0^{(2)}(\boldsymbol{\xi})$ where $\boldsymbol{\xi} \in \mathcal{A}^{(2)}$ denotes the natural coordinates. Likewise for $\mathbf{x}_m \in \gamma^{(2)}$, one has $\mathbf{x}_m = \mathbf{\Psi}_t^{(2)}(\boldsymbol{\xi})$. The bi-linear isoparametric mapping given in (3.16) can be viewed as a special case of the parametrization.

With the parametrization, convected bases are defined as partial derivatives of the mapping with respect to the natural coordinates:

$$\mathbf{E}_\alpha(\boldsymbol{\xi}) = \frac{\partial \mathbf{\Psi}_0^{(2)}(\boldsymbol{\xi})}{\partial \xi^\alpha}\tag{3.32}$$

and
$$\mathbf{e}_\alpha(\xi) = \frac{\partial \mathbf{\Psi}_t^{(2)}(\xi)}{\partial \xi^\alpha} = \mathbf{F}_t^{(2)}\left(\mathbf{\Psi}_0^{(2)}(\xi)\right)\mathbf{E}_\alpha(\xi), \quad (\alpha = 1, 2), \tag{3.33}$$

where $\mathbf{F}_t^{(2)}$ is the deformation gradient corresponding to $\mathbf{\varphi}_t^{(2)}$. By introducing the notation $\bar{\xi}$, the material point achieving the minimum in (3.8) can be written as

$$\bar{\mathbf{X}}_m = \mathbf{\Psi}_0^{(2)}\left(\bar{\xi}\right) \tag{3.34}$$

and its spatial counterpart, i.e. the closest projection of $\mathbf{x} = \mathbf{\varphi}_t^{(1)}(\mathbf{X})$ on $\gamma^{(2)}$, is obtained similarly as

$$\bar{\mathbf{x}}_m = \mathbf{\Psi}_t^{(2)}\left(\bar{\xi}\right). \tag{3.35}$$

The convected base vectors at $\bar{\xi}$ are denoted by

$$\mathbf{T}_\alpha = \mathbf{E}_\alpha\left(\bar{\xi}\right) \tag{3.36}$$

and
$$\mathbf{\tau}_\alpha = \mathbf{e}_\alpha\left(\bar{\xi}\right). \tag{3.37}$$

The outward normal used in the previous section can be readily obtained by

$$\mathbf{n} = \frac{\mathbf{\tau}_1 \times \mathbf{\tau}_2}{\left|\mathbf{\tau}_1 \times \mathbf{\tau}_2\right|}. \tag{3.38}$$

3.1.3.2 Frictional kinematics

The slip rate is derived by considering the time rate of the change of the relative position between $\mathbf{x}_s = \mathbf{\varphi}_t^{(1)}(\mathbf{X}_s)$ and $\bar{\mathbf{x}}_m = \mathbf{\varphi}_t^{(2)}(\bar{\mathbf{X}}_m)$. When $t_N > 0$, according to (3.12) and (3.13), one has $g = 0$ and $\dot{g} = 0$, which indicates that

$$\frac{d}{dt}\left[\mathbf{\varphi}^{(1)}(\mathbf{X}_s, t) - \mathbf{\varphi}^{(2)}\left(\bar{\mathbf{X}}_m(\mathbf{X}_s, t), t\right)\right] = 0. \tag{3.39}$$

Using the chain rule, the time derivative yields the following expression for the relative velocity

$$\mathbf{V}^{(1)}(\mathbf{X}_s, t) - \mathbf{V}^{(2)}\left(\bar{\mathbf{X}}_m(\mathbf{X}_s, t), t\right) = \mathbf{F}_t^{(2)}\left(\bar{\mathbf{X}}_m\right)\frac{d}{dt}\left[\bar{\mathbf{X}}_m(\mathbf{X}_s, t)\right], \tag{3.40}$$

where the right hand side is related to the change of material point $\overline{\mathbf{X}}_m$ due to the relative sliding of the contact surface. A geometric object is defined as

$$\boldsymbol{\mathcal{V}}_T\left(\mathbf{X}_s,t\right) = \frac{d}{dt}\left[\overline{\mathbf{X}}_m\left(\mathbf{X}_s,t\right)\right] = \dot{\overline{\xi}}^{\alpha}\mathbf{T}_{\alpha}, \tag{3.41}$$

which represents the relative velocity in the convected description. The dual of the object can be written as

$$\boldsymbol{\mathcal{V}}_T^b\left(\mathbf{X}_s,t\right) = M_{\alpha\beta}\dot{\overline{\xi}}^{\beta}\mathbf{T}^{\alpha}, \tag{3.42}$$

where $M_{\alpha\beta} = \mathbf{T}_{\alpha}\cdot\mathbf{T}_{\beta}$ is the metric and $\mathbf{T}^{\alpha}\cdot\mathbf{T}_{\beta} = \delta_{\beta}^{\alpha}$. Pushing forward the dual yields the spatial relative velocity, i.e. the slip rate

$$\mathbf{v}_T^b\left(\mathbf{X}_s,t\right) = M_{\alpha\beta}\dot{\overline{\xi}}^{\beta}\boldsymbol{\tau}^{\alpha}. \tag{3.43}$$

3.1.3.3 Frictional contact constraints

The frictional contact traction includes both normal and tangential components and it can be written as

$$\overline{\mathbf{t}}^{(1)} = t_N\mathbf{n} - \mathbf{t}_T^b, \tag{3.44}$$

where the tangential traction $\mathbf{t}_T^b$ can be expressed in terms of the convected basis as

$$\mathbf{t}_T^b = t_{T_{\alpha}}\boldsymbol{\tau}^{\alpha}. \tag{3.45}$$

Assuming the Coulomb friction law for the frictional traction and the slip rate, the following conditions hold:

$$\left.\begin{aligned}
\Phi &:= \left|\mathbf{t}_T^b\right| - \mu t_N \leq 0 \\
\mathbf{v}_T^b &- \zeta\frac{\mathbf{t}_T^b}{\left|\mathbf{t}_T^b\right|} = 0 \\
\zeta &\geq 0 \\
\Phi\zeta &= 0
\end{aligned}\right\} \tag{3.46}$$

where μ is the friction coefficient and ζ is the magnitude of the slip rate. According to the friction law, slip occurs along the direction of $\mathbf{t}_T^b$ when $\left|\mathbf{t}_T^b\right| = \mu t_N$; Otherwise stick is found if $\left|\mathbf{t}_T^b\right| < \mu t_N$.

With contact tractions expressed as (3.44), the contact virtual work (3.5) can be written as

$$\delta W_C\left(\boldsymbol{\varphi}_t, \delta\boldsymbol{\varphi}\right) = -\int_{\Gamma^{(1)}} \left(t_N \mathbf{n} - t_{T_\alpha}\boldsymbol{\tau}^\alpha\right) \cdot \left(\delta\boldsymbol{\varphi}^{(1)} - \delta\boldsymbol{\varphi}^{(2)}\right) d\Gamma^{(1)}. \tag{3.47}$$

It can be verified (as in [1] or Appendix A) that when $g = 0$,

$$\delta\overline{\xi}^\alpha = \boldsymbol{\tau}^\alpha \cdot \left(\delta\boldsymbol{\varphi}^{(1)}\left(\mathbf{X}_s\right) - \delta\boldsymbol{\varphi}^{(2)}\left(\overline{\mathbf{X}}_m\right)\right), \tag{3.48}$$

which together with (3.14) yields

$$\delta W_C\left(\boldsymbol{\varphi}_t, \delta\boldsymbol{\varphi}\right) = \int_{\Gamma^{(1)}} \left(t_N \delta g + t_{T_\alpha}\delta\overline{\xi}^\alpha\right) d\Gamma^{(1)}. \tag{3.49}$$

3.1.3.4 Penalty regularization

The tangential frictional tractions $\mathbf{t}_T^b$ are determined by the friction law (3.46). The analogy of the friction law (3.46) with plasticity can be easily identified. $(3.46)_1$ is analogous to the yield condition and $(3.46)_2$ can be interpreted as a flow rule. By introducing a tangential penalty ε_T, (3.46) can be regularized as

$$\left.\begin{array}{l} \Phi := \left|\mathbf{t}_T^b\right| - \mu t_N \leq 0 \\[2mm] \mathbf{v}_T^b - \zeta\dfrac{\mathbf{t}_T^b}{\left|\mathbf{t}_T^b\right|} = \dfrac{1}{\varepsilon_T}\mathcal{L}_v\mathbf{t}_T^b \\[2mm] \zeta \geq 0 \\[1mm] \Phi\zeta = 0 \end{array}\right\}, \tag{3.50}$$

where in $(3.50)_2$ $\mathcal{L}_v\mathbf{t}_T^b = \dot{t}_{T_\alpha}\boldsymbol{\tau}^\alpha$ is the Lie derivative of the tangential traction $\mathbf{t}_T^\alpha$. When $\Phi < 0$, one has $\zeta = 0$ and Equation $(3.50)_2$ becomes $\mathcal{L}_v\mathbf{t}_T^b = \varepsilon_T\mathbf{v}_T^b$, which is similar to elastic loading in plasticity.

With (3.50), a return mapping algorithm can be derived to integrate the friction law. Given an incremental displacement from time step n to the next step $n+1$, a trial state is first constructed by assuming that the stick condition is satisfied. If $(3.46)_1$ is violated with the trial, a return mapping is applied. Assume that the normal component of the contact traction is regularized by penalty formulation (3.27), the equations for return mapping can be summarized as follows:

$$
\text{Trial state:} \quad
\begin{aligned}
t_{N_{n+1}} &= \varepsilon_N \left\langle g_{n+1} \right\rangle \\
t^*_{T_{n+1_\alpha}} &= t_{T_{n_\alpha}} + \varepsilon_T M_{\alpha\beta} \left[\bar{\xi}^{\beta}_{n+1} - \bar{\xi}^{\beta}_{n} \right] \\
\Phi^*_{n+1} &= \left| \mathbf{t}^{b*}_{T_{n+1}} \right| - \mu t_{N_{n+1}}
\end{aligned}
\qquad (3.51)
$$

$$
\text{Return mapping:} \quad
t_{T_{n+1_\alpha}} =
\begin{cases}
t^*_{T_{n+1_\alpha}}, & \text{if } \Phi^*_{n+1} \leq 0 \ \ \text{(stick);} \\[2ex]
\mu t_{N_{n+1}} \dfrac{t^*_{T_{n+1_\alpha}}}{\left| \mathbf{t}^{b*}_{T_{n+1}} \right|}, & \text{otherwise \ (slip).}
\end{cases}
\qquad (3.52)
$$

The details of the algorithm were presented by Simo and Laursen in [38]. Consistent linearization of the algorithm produces unsymmetrical tangent operators and the reason is due to the nonassociativity of $(3.46)_2$. More discussions on this were also made in [38]. An algorithmic symmtrization technique based on augmented Lagrange multiplier method was proposed in [40] and the technique is adopted for the mesoscale yarn interaction study, which will be introduced in Section 3.4.

3.2 Collision detection

3.2.1 General mesh-to-mesh collision detection

For contact computations, given the position of a slave node, $\mathbf{x}_s$, it is necessary to identify its closest projection point $\bar{\mathbf{x}}_m$ on a master segment, based on which the penetration and the relative sliding between the slave node and the master segment are calculated. The identification procedure is usually called collision detection. For a

general mesh-to-mesh contact scenario, the collision detection usually takes three steps as outlined by Hallquist et al. [44,45]:

3.2.1.1 Nearest neighbor searching

In this step, the master node that is closest to a given node is identified. For a problem with M master nodes and N slave nodes, the total complexity of the global search involves a complexity of $O(MN)$. Spatial locality may be utilized to reduce the cost to $O(N)$ by assuming that the nearest neighbor at the next time step is in the neighborhood of the current closest node. However, this assumption is not valid if contact surfaces are highly distorted.

3.2.1.2 Master segment searching

Multiple master segments surround the master node and the objective of this step is to determine the active segment which contains the projection of the slave node. Assume that the position of the slave node and the master node is denoted by $\mathbf{x}_s$ and $\mathbf{y}$, respectively. The following conditions were proposed by Hallquist et al. [44,45] to identify which of the segment if any contains the projection

$$(\mathbf{c}_1 \times \mathbf{s}) \cdot (\mathbf{c}_1 \times \mathbf{c}_2) > 0 \text{ and } (\mathbf{c}_1 \times \mathbf{s}) \cdot (\mathbf{s} \times \mathbf{c}_2) > 0, \tag{3.53}$$

where $\mathbf{c}_1$ and $\mathbf{c}_2$ denote the edges of the segment as shown in Fig.12. Assuming that the position vector of $\mathbf{x}_s$ relatively to $\mathbf{y}$ is denoted by $\mathbf{p} = \mathbf{x}_s - \mathbf{y}$, the vector $\mathbf{s}$ is the projection of the relative position vector onto the segment. It is determined as follows

$$\mathbf{s} = \mathbf{p} - (\mathbf{p} \cdot \mathbf{t})\mathbf{t}, \tag{3.54}$$

with

$$\mathbf{p} = \mathbf{x}_s - \mathbf{y} \quad \text{and} \quad \mathbf{t} = \frac{\mathbf{c}_1 \times \mathbf{c}_2}{|\mathbf{c}_1 \times \mathbf{c}_2|}, \tag{3.55}$$

where vector $\mathbf{t}$ is the outward normal to the segment considered at point $\mathbf{y}$.

For a pair of slave and master nodes determined from the nearest neighbor searching in the previous step, the conditions given in (3.53) are applied to each master segment that connects the master node. Depending on the local convexity and/or concavity of the master surface, the conditions in (3.53) can be satisfied by multiple segments or none and thus become inconclusive. In these cases, the slave node is usually projected onto the intersections of segments. A detailed discussion on this issue is presented in Section 3.2.2.
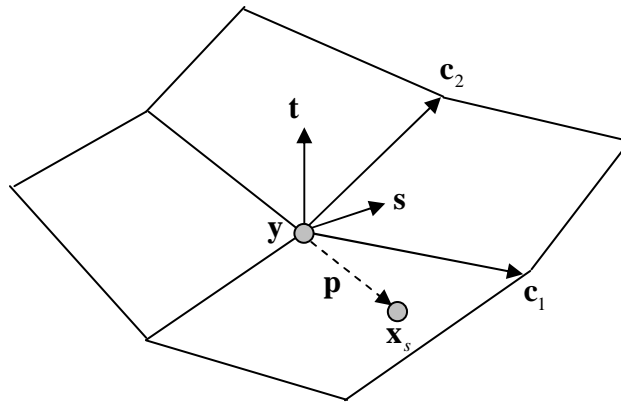
Figure 12: A schematic for master segment searching conditions

3.2.1.3 Projection point calculation

In this step, the closest projection point of the slave node point $\mathbf{x}_s$ onto the master segment is calculated. For a slave penetrating a quadrilateral master segment, the gap function definition shown in Fig.11 and expressed in Equation (3.9) is used. If the quadrilateral is defined by a bi-linear isoparametric mapping, i.e. (3.16) and (3.17), the natural coordinates of the projection point, $\overline{\boldsymbol{\xi}} = \left(\overline{\xi}^1, \overline{\xi}^2 \right)$ will satisfy the following conditions:

$$\mathbf{x}_{m,\xi^1}\left(\overline{\xi}\right)\cdot\left(\mathbf{x}_s - \mathbf{x}_m\left(\overline{\xi}\right)\right) = 0$$
$$\mathbf{x}_{m,\xi^2}\left(\overline{\xi}\right)\cdot\left(\mathbf{x}_s - \mathbf{x}_m\left(\overline{\xi}\right)\right) = 0$$

(3.56)

These equations are nonlinear and can be solved iteratively using Newton's method for $\overline{\xi}$. The tangent vectors $\boldsymbol{\tau}_\alpha, (\alpha = 1, 2)$ and the normal vector $\mathbf{n}$ are then determined by Equation (3.37) and (3.38), respectively. Based on them, the element level contact contributions to the global residual force vector and the global tangent stiffness matrix can be computed and assembled.

3.2.2 Improvements on master segment searching

3.2.2.1 Segment searching conditions

The conditions given in Equation (3.53) can be inconclusive in that, for a convex master surface, multiple segments may satisfy the conditions, while for a concave master surface it is possible that none of the segments satisfies the conditions. When these uncertainties occurs, algorithms specifying which master segment to be considered for the subsequent contact computations can significantly affect the final results and even the convergence of the solutions. This issue has been discussed by Laursen in [41] for two-dimensional problems. In this section, the discussion is extended to three-dimensional problems and a new segment searching algorithm is developed.

First, a set of conditions is devised, which is equivalent to those in Equation (3.53) but with less associated computation expense. As $\mathbf{c}_1$, $\mathbf{c}_2$ and $\mathbf{t}$ are linearly independent, the vector $\mathbf{p} = \mathbf{x}_s - \mathbf{y}$ can be written as

$$\mathbf{p} = (\mathbf{p}\cdot\mathbf{c}_1)\mathbf{c}_1 + (\mathbf{p}\cdot\mathbf{c}_2)\mathbf{c}_2 + (\mathbf{p}\cdot\mathbf{t})\mathbf{t},$$

from which one has

$$\mathbf{s} = \mathbf{p} - (\mathbf{p}\cdot\mathbf{t})\mathbf{t} = (\mathbf{p}\cdot\mathbf{c}_1)\mathbf{c}_1 + (\mathbf{p}\cdot\mathbf{c}_2)\mathbf{c}_2.$$

(3.57)

Substituting (3.57) into (3.53) yields

$$\left(\mathbf{c}_1 \times \mathbf{s}\right) \cdot \left(\mathbf{c}_1 \times \mathbf{c}_2\right) = \left(\mathbf{p} \cdot \mathbf{c}_2\right)\left|\mathbf{c}_1 \times \mathbf{c}_2\right|^2 > 0,$$
$$\left(\mathbf{c}_1 \times \mathbf{s}\right) \cdot \left(\mathbf{s} \times \mathbf{c}_2\right) = \left(\mathbf{p} \cdot \mathbf{c}_2\right)\left(\mathbf{p} \cdot \mathbf{c}_1\right)\left|\mathbf{c}_1 \times \mathbf{c}_2\right|^2 > 0.$$

(3.58)

Since $\left|\mathbf{c}_1 \times \mathbf{c}_2\right|^2 > 0$, one has

$$\mathbf{p} \cdot \mathbf{c}_1 > 0 \text{ and } \mathbf{p} \cdot \mathbf{c}_2 > 0. \tag{3.59}$$

These conditions are equivalent to those of (3.53) but involve only two dot product operations, eliminating the need for four cross-product operations.

3.2.2.2 Two-dimensional problems

In two-dimensional space, a master node can have up to two surrounding segments. Assume that the two segments are $\mathbf{c}_1$ and $\mathbf{c}_2$, and the projection of $\mathbf{p} = \mathbf{x}_s - \mathbf{y}$ on the segments are denoted by $p_i = \mathbf{p} \cdot \mathbf{c}_i, (i = 1, 2)$. Depending on the relative position of the slave node and the master segments, four cases (illustrated in Fig.13) are possible:

1. $p_1 > 0$ and $p_2 > 0$, both segments may be active;

2. $p_1 > 0$ and $p_2 \leq 0$, segment $\mathbf{c}_1$ is active;

3. $p_1 \leq 0$ and $p_2 > 0$, segment $\mathbf{c}_2$ is active;

4. $p_1 \leq 0$ and $p_2 \leq 0$, the intersection of $\mathbf{c}_1$ and $\mathbf{c}_2$ is the projection and both segments are active.
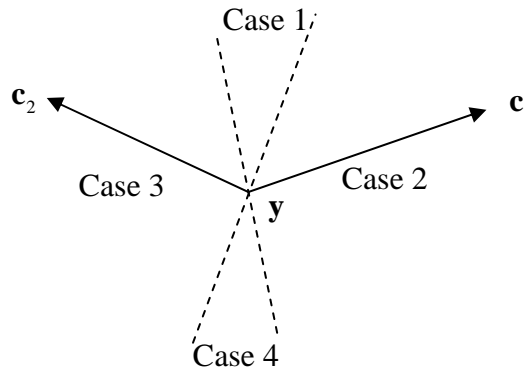
Figure 13: Four cases to determine active master segment

In Case 1, both segments are candidates, posing uniqueness problems. A common practice is to choose the segment involving the minimum penetration as mentioned in [41]. An even simpler practice, as introduced in [45], is to choose whichever segment that satisfies the condition $p_i > 0$ first. These practices can introduce algorithmically biased artifacts to the computations. By following the time history of the slave node's position relative to the master surface, a better estimate on the actual master segment may be obtained. However, this idea is not further explored here.

Another issue is associated with Case 4, where both segments are active. If only one constraint is applied as [45], the solution may oscillate as the constraints are alternatively activated and deactivated and thus fail to converge. For example, in the following problem (Fig.14) an elastic block is pressed onto a concave rigid surface. Node 1 penetrates both segments $\mathbf{c}_1$ and $\mathbf{c}_2$ as the block deforms. If only one constraint, say $\mathbf{c}_1$, is activated, the solution may oscillate between position 1 and 2. Penetration persists and convergence is affected. To avoid this problem, active constraints should be applied simultaneously.
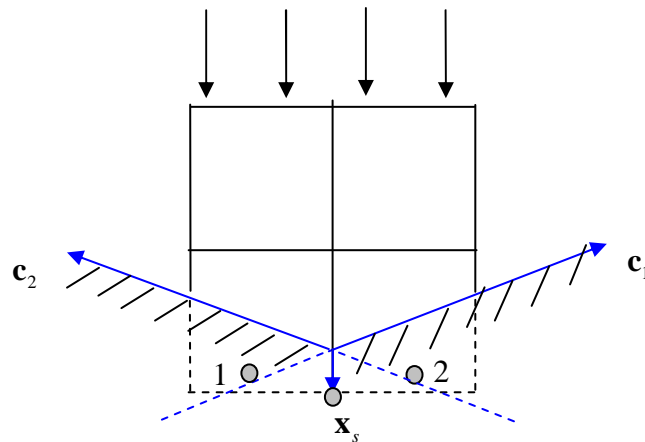
Figure 14: Solution oscillates if only one constraint is applied

3.2.2.3 Three dimensional problems

In three-dimensional space, assume that a master node is surrounded by four segments. The four intersections of the segments are denoted by $\mathbf{c}_i, (i=1,2,...4)$ and the projection of $\mathbf{p} = \mathbf{x}_s - \mathbf{y}$ on the intersections are $p_i = \mathbf{p} \cdot \mathbf{c}_i, (i=1,2,...4)$. Depending on the combinations of the signs of p_i, there are sixteen possible cases, which can be summarized as follows:

1. $p_i \leq 0, (i=1,2,...4)$, the slave node projected onto the master node;

2. $p_i > 0$ and $p_j \leq 0, (i, j = 1,2,...4$ and $j \neq i)$, edge $\mathbf{c}_i$ is active;

3. $p_1, p_3 > 0$ and $p_2, p_4 \leq 0$, both edge $\mathbf{c}_1$ and $\mathbf{c}_3$ may be active;

   $p_2, p_4 > 0$ and $p_1, p_3 \leq 0$, both edge $\mathbf{c}_2$ and $\mathbf{c}_4$ may be active

4. $p_1, p_2 > 0$ and $p_3, p_4 \leq 0$, segment $(\mathbf{c}_1, \mathbf{c}_2)$ is active;

   $p_2, p_3 > 0$ and $p_1, p_4 \leq 0$, segment $(\mathbf{c}_2, \mathbf{c}_3)$ is active;

   $p_3, p_4 > 0$ and $p_1, p_2 \leq 0$, segment $(\mathbf{c}_3, \mathbf{c}_4)$ is active;

   $p_4, p_1 > 0$ and $p_2, p_3 \leq 0$, segment $(\mathbf{c}_4, \mathbf{c}_1)$ is active;

5. $p_1, p_2, p_3 > 0$ and $p_4 \leq 0$, both $(\mathbf{c}_1, \mathbf{c}_2)$ and $(\mathbf{c}_2, \mathbf{c}_3)$ may be active;

   $p_2, p_3, p_4 > 0$ and $p_1 \leq 0$, both $(\mathbf{c}_2, \mathbf{c}_3)$ and $(\mathbf{c}_3, \mathbf{c}_4)$ may be active;

   $p_3, p_4, p_1 > 0$ and $p_2 \leq 0$, both $(\mathbf{c}_3, \mathbf{c}_4)$ and $(\mathbf{c}_4, \mathbf{c}_1)$ may be active;

   $p_4, p_1, p_2 > 0$ and $p_3 \leq 0$, both $(\mathbf{c}_4, \mathbf{c}_1)$ and $(\mathbf{c}_1, \mathbf{c}_2)$ may be active;

6. $p_i > 0, (i=1,2,...4)$, all four segments may be active.

If multiple segments or edges are active, it is necessary to apply the constraints simultaneously to avoid solution oscillation.

3.2.3 Collision detection with implicit surfaces

General mesh-to-mesh collision detection as described in Section 3.2.1 can be computationally intensive and a major portion of the expense is due to the global nearest neighbor searching, which has a complexity proportional to the number of nodes in both surface meshes. Locality may be utilized by assuming that candidates for nearest

neighbors at a time step $n+1$ belong to the neighborhood of the current nearest neighbors at step n. However, as noted previously, this assumption can be invalid for problems where the contact surface meshes are highly distorted. The other significant bottleneck of collision detection is the projection point calculation, where a nonlinear equation system such as (3.56) is solved with Newton's iterations. Efficient collision detection algorithms for general mesh-to-mesh contact still remain an active research topic, e.g.[36,37]. A discussion of these algorithms is beyond the scope of this study and thus not presented here.

Some surfaces can alternatively be represented by closed mathematical forms instead of discrete polygonal meshes. Such a surface is usually named as an implicit surface, which is defined by a scalar function of spatial coordinates as $f(\mathbf{x}) = 0$. Given a spatial point $\mathbf{x}$, the sign of the function value indicates the position of the point relative to the surface.

$$\text{If } f(\mathbf{x}) > 0, \ \mathbf{x} \text{ lies outside of the surface and is thus admissible;}$$
$$\text{If } f(\mathbf{x}) = 0, \ \mathbf{x} \text{ is on the surface;} \tag{3.60}$$
$$\text{If } f(\mathbf{x}) < 0, \ \mathbf{x} \text{ lies inside of the surface and is thus inadmissible.}$$

An example of an implicit surface is an ellipsoid, which is defined by a scalar function as

$$f(\mathbf{x}) = \sum_{i=1,2,3} \left[\left(x_i - x_i^c \right)^2 / r_i^2 \right] - 1 = 0, \tag{3.61}$$

where $x_i^c, (i = 1, 2, 3)$ denotes the center of an ellipsoid and r_i are the radii along the principal axes. With an ellipsoid, the expense of collision detection is significantly reduced.

3.3 Contact computation for macroscale clothing modeling

3.3.1 General considerations

Methods for modeling mechanical interactions between clothing and a wearer are studied in this section. Clothing can interact with a wearer in various aspects, such as

weight, size, fit and stretchiness of fabrics etc. The study here concentrates on the contact tractions that clothing exerts on a wearer. The tractions are treated as fundamental quantities, which can be further related to other interaction measures. To quantify the contact tractions between clothing and a wearer, the contact computation techniques outlined in Section 3.1 can be utilized although the solution method can be simplified somewhat based on the considerations described in the following subsections.

3.3.1.1 Signorini's problem

The problem is to calculate the time history of the contact tractions that clothing exerts when a wearer goes through given motions. For simplification, two assumptions are adopted. First, the body surface of the wearer is assumed to be rigid, which excludes the possibility of body deformation introduced by clothing. Second, the motions of the wearer are prescribed and do not change in response to the clothing interactions. These two assumptions limit the problem to a unilateral scenario, where clothing passively responds to the evolutions of a rigid body surface, which in contact literature is classified as a "rigid obstacle problem" or a Signorini problem. These assumptions can be removed if a deformable human body model is available and if the sensitivity of human motions to clothing resistance is understood. However, these assumptions are currently invoked to reduce the complexity of the problem.

3.3.1.2 Expense of collision detection

As mentioned in Section 3.2, mesh-to-mesh collision detection is computationally intensive. A coarse approximation of a complete human body surface mesh may require thousands of polygons and that number multiplied by the size of the clothing mesh makes the collision detection quite expensive. To limit the expense, a placeholder human body surface definition based on the concept of implicit surfaces is adopted. In this study, the human body surface is approximated by an assemblage of ellipsoids undergoing prescribed rigid-body motions and contact computation for macroscale clothing modeling

is discussed in the context of a discrete finite element clothing mesh interacting with these ellipsoids.

3.3.1.3 Robustness of solution methods

The macroscale clothing model is based on the time integration of a dynamic, flexible clothing system. Both explicit and implicit solution methods can be used to solve the problem. In general, explicit methods are capable of capturing transient response with very small time steps and are thus preferred for high-velocity problems. In such methods, the nonlinear global equations can be solved at each time increment without Newton iterations. Implicit time integration methods, which are more stable and thus allow larger time increments, are mostly applied to solve quasi-static and low-velocity problems. Implicit methods generally require Newton iterations to solve the global equations at each increment.

However, for clothing contact problems, an important factor to be considered is the robustness of the solution method. The convergence of an implicit solution scheme relies on the consistency between the residual vector and the linearized tangential operator. For problems where complex contact is involved and very large deformations occur, the discontinuities in the contact conditions can affect the consistency and thus yield convergence difficulties. For this reason, an explicit solution method is chosen to study the clothing-wearer interaction problems.

3.3.1.4 Penalty formulation

For a contact problem based on a penalty formulation, variations of the system in Equation (3.28) are solved. As no extra unknowns are introduced, the penalty formulation can be readily incorporated into standard finite element solution algorithms, such as the Newton's method (Box 1) and Newmark integration methods (Box 2). For central difference time integration, i.e. $\alpha = 1/2$ and $\beta = 0$ in the Newmark methods given in Equation (2.76), one has

$$\mathbf{v}^{n+1} = \mathbf{v}^n + \frac{\Delta t}{2}\mathbf{a}^n + \frac{\Delta t}{2}\mathbf{a}^{n+1};$$

$$\mathbf{d}^{n+1} = \mathbf{d}^n + \Delta t\mathbf{v}^n + \frac{\Delta t^2}{2}\mathbf{a}^n.$$

(3.62)

The solution algorithm is as follows, (Box 3), where the Step 2.c is the only modification introduced to the original integration scheme.

---

1. Initialization: set increment count $n=0$ and initial state $\mathbf{d}^0$, $\mathbf{v}^0$ and $\mathbf{a}^0$
2. Solve for load/time increment $n+1$
   a. Form predictors
   $$\mathbf{v}^* = \mathbf{v}^n + \frac{\Delta t}{2}\mathbf{a}^n; \quad \mathbf{d}^* = \mathbf{d}^n + \Delta t\mathbf{v}^n + \frac{\Delta t^2}{2}\mathbf{a}^n$$
   b. Compute residual
   $$\tilde{\mathbf{r}}^* = \mathbf{f}^{ext} - \mathbf{f}^{int}\left(\mathbf{d}^*\right)$$
   c. Call collision detection module to identify penetration; calculate penalty force $\mathbf{f}^{cnt}\left(\mathbf{d}^*\right)$ and update the residual vector $\tilde{\mathbf{r}}^* = \tilde{\mathbf{r}}^* - \mathbf{f}^{cnt}\left(\mathbf{d}^*\right)$.
   d. Construct tangent stiffness, i.e. mass matrix in this case
   $$\tilde{\mathbf{K}}^* = \mathbf{M}$$
   e. Solve for the incremental acceleration
   $$\mathbf{a}^{n+1} = -\left(\tilde{\mathbf{K}}^*\right)^{-1}\cdot\tilde{\mathbf{r}}^*$$
   f. Update the velocity
   $$\mathbf{v}^{n+1} = \mathbf{v}^* + \frac{\Delta t}{2}\mathbf{a}^{n+1}; \quad \mathbf{d}^{n+1} = \mathbf{d}^*$$
3. Set $n = n+1$ and go to 2.

Box 3: Penalty formulation using central difference integration

While the penalty formulation has the benefit of not introducing any additional unknowns to the analysis problem, a major disadvantage of the penalty formulation is ambiguity in the choice of a penalty parameter. If chosen too small, unacceptable penetration results, and if chosen too large, the critical time step size of an explicit time

integrator can be significantly reduced. Some guidelines on choosing appropriate penalty parameters were given by Belytschko and Neal in [43]. Another issue in applying a penalty formulation in clothing-wearer interaction models is that since the penalty force changes discontinuously as penetration occurs and then disappears, a contact node tends to bounce on the contact boundary under the influence of the penalty force. This oscillatory response can be intuitively explained by interpreting a contact boundary as a stiff cushion of penalty springs, which pushes penetrating nodes away and then releases when penetration disappears. Since the clothing is quite flexible and provides little restitution, such oscillatory responses should be avoided. For these reasons, an explicit solution based on Lagrange multiplier methods is developed for the macroscale clothing modeling.

3.3.2 Explicit Lagrange multiplier methods

For explicit Lagrange multiplier methods, the contact surface can be determined directly by projection of the overlapped volume of the bodies updated by uncoupled integration without iteration needed. It was shown by Belytschko and Neal [43] that in this case the Lagrange multipliers with correct sign can be determinable directly. A similar approach, namely 'forward increment Lagrange multiplier' method was proposed by Carpenter et al. [42]. In their approach, a predictor state is first constructed using central difference time integration on both bodies neglecting the contact interaction and then the Lagrange multipliers that enforce the impenetrability constraints on the predictor state are solved. Consider time stepping from t^n to t^{n+1}, the equations can be summarized as follows

$$\left.\begin{array}{c} \mathbf{f}^{int}\left(\mathbf{d}^n\right) + \mathbf{M} \cdot \mathbf{a}^n + \mathbf{G}^T \cdot \boldsymbol{\lambda}^n = \mathbf{f}^{ext}\left(t^n\right) \\ \mathbf{G} \cdot \left(\mathbf{d}^{n+1} + \mathbf{X}\right) = 0 \end{array}\right\} \tag{3.63}$$

where the acceleration at time step t^n is decomposed into a predictor part and a corrector part as $\mathbf{a}^n = \mathbf{a}^* + \mathbf{a}^c$ with

$$\mathbf{a}^* = \mathbf{M}^{-1} \cdot \left[\mathbf{f}^{ext}\left(t^n\right) - \mathbf{f}^{int}\left(\mathbf{d}^n\right) \right] \text{ and } \mathbf{a}^c = -\mathbf{M}^{-1} \cdot \mathbf{G}^T \cdot \boldsymbol{\lambda}^n. \tag{3.64}$$

According to the central difference integration scheme

$$\mathbf{a}^n = \frac{1}{\left(\Delta t\right)^2}\left(\mathbf{d}^{n+1} - 2\mathbf{d}^n + \mathbf{d}^{n-1}\right),$$

the displacement can be written as

$$\mathbf{d}^{n+1} = \mathbf{d}^* + \mathbf{d}^c, \tag{3.65}$$

with a predictor and a corrector displacement, respectively as

$$\mathbf{d}^* = \left(\Delta t\right)^2 \mathbf{a}^* + 2\mathbf{d}^n - \mathbf{d}^{n-1} \text{ and } \mathbf{d}^c = \left(\Delta t\right)^2 \mathbf{a}^c. \tag{3.66}$$

If the impenetrability constraint is violated for the predictor displacement $\mathbf{d}^*$, the contact constraint matrix is constructed as $\mathbf{G} = \mathbf{G}\left(\mathbf{d}^*\right)$ and the corrector can be solved by $(3.63)_2$

$$\mathbf{G} \cdot \mathbf{d}^c + \mathbf{G} \cdot \left(\mathbf{d}^* + \mathbf{X}\right) = 0,$$

which combined with (3.66) and (3.64) yields the Lagrange multiplier

$$\boldsymbol{\lambda}^n = \left[\left(\Delta t\right)^2 \mathbf{G}\mathbf{M}^{-1}\mathbf{G}^T\right]^{-1} \mathbf{G} \cdot \left(\mathbf{d}^* + \mathbf{X}\right). \tag{3.67}$$

The velocity is then calculated using

$$\mathbf{v}^n = \left(\mathbf{d}^{n+1} - \mathbf{d}^{n-1}\right)\big/\left(2\Delta t\right). \tag{3.68}$$

The procedure above essentially prevents a slave node from penetrating the master surface at time instant t^{n+1} by applying a brake force vector $\boldsymbol{\lambda}^n$, i.e. the Lagrange multipliers, at t^n.

Written according to the framework of Newmark time integration, the procedure can be summarized in Box 4. If no penetration is identified, the procedure is identical to the Newmark integration with $\alpha = 1/2$ and $\beta = 0$.

1. Initialization: set increment count $n=0$ and initial state $\mathbf{d}^0$, $\mathbf{v}^0$ and $\mathbf{a}^0$
2. Solve for load/time increment $n+1$
   a. Form predictors

$$\mathbf{v}^* = \mathbf{v}^n + \frac{\Delta t}{2}\mathbf{a}^n; \quad \mathbf{d}^{n+1} = \mathbf{d}^n + \Delta t\mathbf{v}^n + \frac{\Delta t^2}{2}\mathbf{a}^n$$

   b. Solve for predictor acceleration

$$\mathbf{a}^* = \mathbf{M}^{-1}\cdot\left[\mathbf{f}^{ext}\left(t^{n+1}\right)-\mathbf{f}^{int}\left(\mathbf{d}^{n+1}\right)\right]$$

   c. Update velocity

$$\mathbf{v}^* = \mathbf{v}^* + \frac{\Delta t}{2}\mathbf{a}^*$$

   d. Construct the trial displacement for $n+2$ by

$$\mathbf{d}^* = \mathbf{d}^{n+1} + \Delta t\mathbf{v}^* + \frac{\Delta t^2}{2}\mathbf{a}^*$$

   If penetration is identified for the trial $\mathbf{d}^*$, solve for the Lagrange multipliers and the corrector

$$\boldsymbol{\lambda}^{n+1} = \left[\left(\Delta t\right)^2 \mathbf{G}\mathbf{M}^{-1}\mathbf{G}^T\right]^{-1}\mathbf{G}\cdot\left(\mathbf{d}^* + \mathbf{X}\right);$$

$$\mathbf{a}^c = -\mathbf{M}^{-1}\cdot\mathbf{G}^T\cdot\boldsymbol{\lambda}^{n+1} \text{ and } \mathbf{d}^c = \left(\Delta t\right)^2\mathbf{a}^c.$$

   Otherwise

$$\boldsymbol{\lambda}^{n+1} = \mathbf{0}, \mathbf{a}^c = \mathbf{0} \text{ and } \mathbf{d}^c = \mathbf{0}$$

   e. Update the solution at $n+1$

$$\mathbf{a}^{n+1} = \mathbf{a}^* + \mathbf{a}^c \text{ and } \mathbf{v}^{n+1} = \mathbf{v}^* + \frac{\Delta t}{2}\mathbf{a}^c$$

3. Set $n = n+1$ and go to 2.

Box 4: Forward increment Lagrange multiplier method for contact computation using Newmark integration

3.3.3 Simplifications

The algorithm in Box 4 is a general explicit solution method for multi-body contact, where both bodies can deform and move. Since the macroscale clothing modeling is currently formulated as a Signorini problem, where the interaction is unilateral, the algorithm can be simplified. The wearer's body surface is treated as a

master surface with its evolution prescribed and completely independent of the contact interaction. The clothing surfaces are treated as slaves and they are driven by the evolution of the master.

---

1. Initialization: set increment count $n=0$ and initial state $\mathbf{d}^0$, $\mathbf{v}^0$ and $\mathbf{a}^0$
2. Solve for load/time increment $n+1$
    f. Form predictors
    $$\mathbf{v}^* = \mathbf{v}^n + \frac{\Delta t}{2}\mathbf{a}^n; \quad \mathbf{d}^{n+1} = \mathbf{d}^n + \Delta t\mathbf{v}^n + \frac{\Delta t^2}{2}\mathbf{a}^n$$
    g. Solve for predictor acceleration
    $$\mathbf{a}^* = \mathbf{M}^{-1} \cdot \left[\mathbf{f}^{ext}\left(t^{n+1}\right) - \mathbf{f}^{int}\left(\mathbf{d}^{n+1}\right)\right]$$
    h. Update velocity
    $$\mathbf{v}^* = \mathbf{v}^* + \frac{\Delta t}{2}\mathbf{a}^*$$
    i. Construct the trial displacement and position for $n+2$ by
    $$\mathbf{d}^* = \mathbf{d}^{n+1} + \Delta t\mathbf{v}^* + \frac{\Delta t^2}{2}\mathbf{a}^* \text{ and } \mathbf{x}^* = \mathbf{d}^* + \mathbf{X}$$

    If penetration is identified for the trial $\mathbf{x}^*$, construct correctors
    $$\mathbf{d}^c = proj\left(\mathbf{x}^*\right) - \mathbf{x}^*, \; \mathbf{a}^c = \mathbf{d}^c/\left(\Delta t\right)^2 \text{ and } \boldsymbol{\lambda}^{n+1} = -\mathbf{M} \cdot \mathbf{a}^c$$

    Otherwise
    $$\boldsymbol{\lambda}^{n+1} = \mathbf{0}, \; \mathbf{a}^c = \mathbf{0} \text{ and } \mathbf{d}^c = \mathbf{0}$$
    j. Update the solution at $n+1$
    $$\mathbf{a}^{n+1} = \mathbf{a}^* + \mathbf{a}^c \text{ and } \mathbf{v}^{n+1} = \mathbf{v}^* + \frac{\Delta t}{2}\mathbf{a}^c$$
3. Set $n = n+1$ and go to 2.

Box 5: Simplification of forward increment Lagrange multiplier algorithm

Following the algorithm in Box 4, a predictor state is constructed by integrating the projectiles of clothing nodes without considering the contact effect. In the meantime, the master surface is independently updated based on the prescribed human motion

kinematics. If the impenetrability constraint is violated, the predictor positions of the clothing nodes are corrected by projecting them onto the updated master surface. Unlike the multi-body contact case, where Equation $(3.63)_2$ needs to be solved, the corrector displacement can be directly obtained by projecting a penetrating slave node onto the master surface. The projection direction may not be unique and a natural approach is to find the closest projection point. For ellipsoidal surfaces, however, the gradient at the penetrating trial position is chosen as the projection direction, which does not yield the closest projection point but gives a fairly close approximation. The simplified algorithm for unilateral clothing-wearer contact interaction can be summarized in Box 5:

3.4 Contact computation for mesoscale yarn

interaction study

The objective of mesoscale yarn interaction studies is to understand the effects that such interactions have on the macroscopic mechanical response properties of woven fabrics. The details of the study are presented in the next chapter, but here the discussion is focused on an implicit contact algorithm for the study. Due to its ready accommodation of frictional contact constraints by using return mapping algorithm, a penalty formulation is chosen.

There are two major difficulties in solving contact problems with a penalty formulation. One is the choice of proper penalty parameters, which should effectively enforce the contact constraints while not significantly impacting the convergence of the solution algorithm. The other difficulty is the asymmetry of the tangent operator resulting from consistent linearization of the friction law. To address these two issues, Laursen and Simo [40,41] proposed an augmented Lagrangian method, which allows small penalty parameters while still enforcing the contact constraints to a high precision through an iterative augmentation procedure. Symmetrical tangent operators are also made possible within this method by fixing the normal traction when integrating the

friction law. Their method is adopted for the yarn interaction study and a brief summary is provided as below.

The mesh-to-mesh collision detection technique outlined in Section 3.2 is adopted for the yarn contact computations since yarns in this study are modeled with hexahedral trilinear finite elements. The spatial locality assumption is applied as the contact surfaces of yarns are usually not distorted excessively under ordinary loading conditions in woven fabrics. A global nearest neighbor search is conducted only once at the beginning of the analysis and subsequent searching is confined to the neighborhoods of the current closest nodes. The improvements discussed in Section 3.2.2 are implemented for master segment searching to reduce the possibility of a slave node trapped on the intersections of multiple master segments.

3.4.1 Augmented Lagrangian regularization

In the augmented Lagrangian method, Lagrange multipliers are introduced in addition to the penalty terms. The constraints are written as follows.

Impenetrability constraint:

$$t_N := \langle \lambda_N + \varepsilon_N g \rangle. \tag{3.69}$$

Friction constraints:

$$\left. \begin{aligned} \Phi &:= \left(t_{T_\alpha} M^{\alpha\beta} t_{T_\beta} \right)^{1/2} - \mu t_N \leq 0 \\ M_{\alpha\beta}\dot{\bar{\xi}}^\beta - \zeta \frac{t_{T_\alpha}}{\left(t_{T_\beta} M^{\beta\gamma} t_{T_\gamma} \right)^{1/2}} &= \frac{1}{\varepsilon_T}\left(\dot{t}_{T_\alpha} - \dot{\lambda}_{T_\alpha} \right) \\ \zeta &\geq 0 \\ \Phi\zeta &= 0 \end{aligned} \right\}. \tag{3.70}$$

Above, λ_N and λ_{T_α} denote the Lagrange multipliers for normal and tangential contact traction components, respectively. For clarity, the component form of the friction contact is given. The only difference between (3.70) and (3.50) is that the frictional traction is expressed in terms of the convected basis in the reference configuration as

$$\mathcal{T}_T^b = t_{T_a} \mathbf{T}^\alpha ,\tag{3.71}$$

which is a pull-back of the spatial quantity (3.45). With the definition (3.71), the norm can be written in terms of the material metric

$$M^{\alpha\beta} = \mathbf{T}^\alpha \cdot \mathbf{T}^\beta \tag{3.72}$$

instead of its spatial counterpart, which introduces further complication for the symmetrization of the tangential operators.

3.4.2 Solution algorithm

3.4.2.1 Global solution algorithm

The global problem is to find $\boldsymbol{\varphi}_t$, λ_N and λ_{T_α} such that

$$\delta W\left(\boldsymbol{\varphi}_t, \delta\boldsymbol{\varphi}\right) + \int_{\Gamma^{(1)}} \left(t_N \delta g + t_{T_\alpha} \delta\bar{\xi}^\alpha\right) d\Gamma^{(1)} = 0 ,\tag{3.73}$$

where t_N and t_{T_α} are given by (3.69) and (3.70), respectively. Equation (3.73) is solved by the following nested iterative procedure. First the configuration $\boldsymbol{\varphi}_t$ is solved by holding the values of the Lagrange multipliers λ_N and λ_{T_α} fixed. Then the Lagrange multipliers are updated by the penalty terms associated with the $\boldsymbol{\varphi}_t$. The procedure is repeated until the contact constraints are enforced with expected precision. The whole solution algorithm consists of two iterative loops, where in the outer loop the Lagrange multipliers are updated iteratively while in the inner loop the configuration/deformation is solved with fixed estimate of the Lagrange multipliers. Assuming that the solution of the global problem at time step n has been determined, the algorithm to find the solution for the next step $n+1$ is summarized in Box 6.

3.4.2.2 Return mapping algorithm

Equation (3.77) in Box 6 is obtained by applying backward Euler time integration scheme to the rate-form constraints (3.69) and (3.70). It is very similar to backward Euler integration algorithms of constitutive relationships in elasto-plasticity. The

procedure is displacement driven in that given an incremental displacement and the current estimate of the Lagrange multipliers, $\lambda_{N_{n+1}}^{(k)}$ and $\lambda_{T_{n+1_\alpha}}^{(k)}$, the contact tractions, $t_{N_{n+1}}^{(k)}$ and $t_{T_{n+1_\alpha}}^{(k)}$, are solved. Equation (3.77) can be solved by a return mapping algorithm as follows:

Trial state:

$$
\begin{aligned}
t_{N_{n+1}}^{(k)} &:= \left\langle \lambda_{N_{n+1}}^{(k)} + \varepsilon_N g_{n+1}^{(k)} \right\rangle \\
t_{T_{n+1_\alpha}}^{(k)*} &= \lambda_{T_{n+1_\alpha}}^{(k)} + \varepsilon_T M_{\alpha\beta} \left[\overline{\xi}_{n+1}^{\beta^{(k)}} - \overline{\xi}_n^\beta \right] \\
\Phi_{n+1}^{(k)*} &= \left[t_{T_{n+1_\alpha}}^{(k)*} M^{\alpha\beta} t_{T_{n+1_\beta}}^{(k)*} \right]^{1/2} - \mu t_{N_{n+1}}^{(k)}
\end{aligned}
\tag{3.74}
$$

Return mapping:

$$
t_{T_{n+1_\alpha}}^{(k)} =
\begin{cases}
t_{T_{n+1_\alpha}}^{(k)*}, & \text{if } \Phi_{n+1}^{(k)*} \leq 0 \;\; \text{(stick)} \\[2ex]
\mu t_{N_{n+1}}^{(k)} \dfrac{t_{T_{n+1_\alpha}}^{(k)*}}{\left[t_{T_{n+1_\beta}}^{(k)*} M^{\beta\gamma} t_{T_{n+1_\gamma}}^{(k)*} \right]^{1/2}}, & \text{otherwise} \;\; \text{(slip)}
\end{cases}
\tag{3.75}
$$

3.4.2.3 Symmetrization

The tangent operator associated with frictional contact is derived by linearizing the frictional virtual work as

$$
\Delta \left(\int_{\Gamma^{(1)}} t_{T_\alpha} \delta \overline{\xi}^\alpha d\Gamma^{(1)} \right) = \int_{\Gamma^{(1)}} \Delta t_{T_\alpha} \delta \overline{\xi}^\alpha d\Gamma^{(1)} + \int_{\Gamma^{(1)}} t_{T_\alpha} \Delta \left(\delta \overline{\xi}^\alpha \right) d\Gamma^{(1)},
\tag{3.76}
$$

where Δt_{T_α} is obtained by linearizing the return mapping algorithm (3.75). Since the slip frictional traction $t_{T_{n+1_\alpha}}^{(k)}$ depends on $g_{n+1}^{(k)}$ through $t_{N_{n+1}}^{(k)}$, linearization of $t_{T_{n+1_\alpha}}^{(k)}$ generates a term related to Δg, which when combined with $\delta \overline{\xi}^\alpha$ yields an unsymmetrical tangent operator.

It is observed that if the normal traction $t_{N_{n+1}}^{(k)}$ is fixed in the solution phase, i.e. Step 2. in Box 6, the asymmetry can be removed. A symmetrical augmented Lagrangian algorithm was designed by Laursen [41]. And the procedure is briefly summarized in

Box 7. In Step 2, the stick/slip condition $\tilde{\Phi}_{n+1}^{(k)}$ is defined in terms of the current estimate of the Lagrange multiplier of the normal traction $\lambda_{N_{n+1}}^{(k)}$, which is fixed throughout the solution phase and thus yields symmetrical tangential operators. And then in Step 3 an additional return map is applied to enforce the frictional contact constraints with the updated normal traction $\lambda_{N_{n+1}}^{(k+1)}$.

---

1. Initialize the Lagrange multipliers and the augmentation count k
    $$\lambda_{N_{n+1}}^{(0)} = \lambda_{N_n}, \lambda_{T_{n+1_\alpha}}^{(0)} = \lambda_{T_{n_\alpha}} \text{ and } k = 0.$$

2. Solve for nodal displacement $\mathbf{d}_{n+1}^{(k)}$ such that
    $$\mathbf{f}^{int}\left(\mathbf{d}_{n+1}^{(k)}\right) + \mathbf{f}^{cnt}\left(\mathbf{d}_{n+1}^{(k)}\right) = \mathbf{f}_{n+1}^{ext},$$
    where $\mathbf{f}^{cnt}$ is deduced from $\int_{\Gamma^{(1)}} \left(t_N \delta g + t_{T_\alpha} \delta \overline{\xi}^\alpha\right) d\Gamma^{(1)}$ with contact traction given by

    $$\left.\begin{aligned}
    t_{N_{n+1}}^{(k)} &:= \left\langle \lambda_{N_{n+1}}^{(k)} + \varepsilon_N g_{n+1}^{(k)} \right\rangle \\[4pt]
    \Phi_{n+1}^{(k)} &:= \left(t_{T_{n+1_\alpha}}^{(k)} M^{\alpha\beta} t_{T_{n+1_\beta}}^{(k)}\right)^{1/2} - \mu t_{N_{n+1}}^{(k)} \le 0 \\[4pt]
    t_{T_{n+1_\alpha}}^{(k)} &= \lambda_{T_{n+1_\alpha}}^{(k)} + \varepsilon_T \left[M_{\alpha\beta}\left(\overline{\xi}_{n+1}^{\beta^{(k)}} - \overline{\xi}_n^{\beta}\right) - \zeta \frac{t_{T_{n+1_\alpha}}^{(k)}}{\left(t_{T_{n+1_\beta}}^{(k)} M^{\beta\gamma} t_{T_{n+1_\gamma}}^{(k)}\right)^{1/2}} \right] \\[4pt]
    \zeta &\ge 0 \\[4pt]
    \Phi_{n+1}^{(k)} \zeta &= 0
    \end{aligned}\right\} \qquad (3.77)$$

3. Update the Lagrange multipliers and the augmentation count k
    $$\lambda_{N_{n+1}}^{(k+1)} = t_{N_{n+1}}^{(k)}, \lambda_{T_{n+1_\alpha}}^{(k+1)} = t_{T_{n+1_\alpha}}^{(k)} \text{ and } k = k+1.$$

4. Return to Step 2. until the solution (displacement and multipliers) converges.

Box 6: Solution algorithm of the augmented Lagrangian method

1. Initialize the Lagrange multipliers and the augmentation count k

$$\lambda_{N_{n+1}}^{(0)} = \lambda_{N_n}, \lambda_{T_{n+1_\alpha}}^{(0)} = \lambda_{T_{n_\alpha}} \text{ and } k = 0.$$

2. Solve for nodal displacement $\mathbf{d}_{n+1}^{(k)}$ such that

$$\mathbf{f}^{int}\left(\mathbf{d}_{n+1}^{(k)}\right) + \mathbf{f}^{cnt}\left(\mathbf{d}_{n+1}^{(k)}\right) = \mathbf{f}_{n+1}^{ext},$$

where

$$
\left.
\begin{aligned}
&t_{N_{n+1}}^{(k)} := \left\langle \lambda_{N_{n+1}}^{(k)} + \varepsilon_N g_{n+1}^{(k)} \right\rangle \\[6pt]
&\tilde{\Phi}_{n+1}^{(k)} := \left(t_{T_{n+1_\alpha}}^{(k)} M^{\alpha\beta} t_{T_{n+1_\beta}}^{(k)} \right)^{1/2} - \mu \lambda_{N_{n+1}}^{(k)} \leq 0 \\[6pt]
&t_{T_{n+1_\alpha}}^{(k)} = \lambda_{T_{n+1_\alpha}}^{(k)} + \varepsilon_T \left[M_{\alpha\beta}\left(\overline{\xi}_{n+1}^{\beta^{(k)}} - \overline{\xi}_n^\beta \right) - \tilde{\zeta} \frac{t_{T_{n+1_\alpha}}^{(k)}}{\left(t_{T_{n+1_\beta}}^{(k)} M^{\beta\gamma} t_{T_{n+1_\gamma}}^{(k)} \right)^{1/2}} \right] \\[6pt]
&\tilde{\zeta} \geq 0 \\[6pt]
&\tilde{\Phi}_{n+1}^{(k)} \tilde{\zeta} = 0
\end{aligned}
\right\} \qquad (3.78)
$$

3. Update the Lagrange multipliers and the augmentation count k

$$
\left.
\begin{aligned}
&\lambda_{N_{n+1}}^{(k+1)} = t_{N_{n+1}}^{(k)} \\[6pt]
&\Phi_{n+1}^{(k+1)} := \left(\lambda_{T_{n+1_\alpha}}^{(k+1)} M^{\alpha\beta} \lambda_{T_{n+1_\beta}}^{(k+1)} \right)^{1/2} - \mu \lambda_{N_{n+1}}^{(k+1)} \leq 0 \\[6pt]
&\lambda_{T_{n+1_\alpha}}^{(k+1)} = t_{T_{n+1_\alpha}}^{(k)} + \varepsilon_T \left(\tilde{\zeta} - \zeta \right) \frac{t_{T_{n+1_\alpha}}^{(k)}}{\left(t_{T_{n+1_\beta}}^{(k)} M^{\beta\gamma} t_{T_{n+1_\gamma}}^{(k)} \right)^{1/2}} \\[6pt]
&\zeta \geq 0 \\[6pt]
&\Phi_{n+1}^{(k+1)} \zeta = 0
\end{aligned}
\right\} \qquad (3.79)
$$

4. Set $k = k+1$ and return to Step 2. until the solution (displacement and multipliers) converges.

Box 7: Symmetrical augmented Lagrangian algorithm by Laursen [41]

CHAPTER 4

MECHANICAL PROPERTIES OF WOVEN FABRICS AND

MESOSCALE FABRIC MODELING

Woven fabrics exhibit complex material behaviors that typically feature nonlinearity, anisotropy and hysteresis. In addition, the response behaviors of woven fabrics are sensitive to changes in load conditions and deformation. For example, the biaxial extension property of a fabric differs significantly from that of biaxial compression or uniaxial extension. Consequently, it is a challenge to formulate constitutive models for fabrics that successfully represent all these complex behaviors and automatically adapt to various load conditions.

Woven fabrics are constructed by weaving yarns in certain regular patterns. The yarns themselves are typically loose bundles of individual fibers that are more or less aligned. The material properties of fabrics are largely determined by the properties of individual yarns, the topology of the yarn structure, and the interactions between the interwoven yarns. Previous efforts have been made and reported in the literature to relate yarn topology, properties, and interactions to the overall fabric properties. Most such models adopt simplified geometric descriptions and yarn interaction assumptions, and the generality of these models is thus limited.

In this chapter, a general three-dimensional textile mechanics model equipped with multi-body frictional contact computations is constructed. The length scales of the models generally correspond to the dimensions of the unit cells associated with the relevant weave patterns. Since this length scale is typically much larger than the diameters of the fibers that comprise the yarns, but much smaller than length scale on which human-clothing interactions are modeled, it is hereafter called the mesoscale. The relationship between the mesoscale textile mechanics model and the macroscopic fabrics properties is investigated by following computational homogenization theory and unit

cell analysis techniques. The organization of this chapter is as follows: First, the mechanical properties of woven fabrics are briefly introduced and some preceding fabric constitutive models are reviewed. Then the computational homogenization approach and the unit cell problem are presented. Finally, multiscale modeling approaches to incorporate realistic fabric properties into the macroscale fabric model framework are discussed.

4.1 Constitutive models of woven fabrics

4.1.1 Mechanical properties of woven fabrics

In general, woven fabrics are constructed by weaving together yarns along two orthogonal directions, i.e. warp and weft, following certain periodic weave patterns. The mechanical properties of fabrics are mostly determined by the properties of constituent yarns, the configuration of the yarn structures and the interactions between interwoven yarns.

Fabrics exhibit highly nonlinear and anisotropic behaviors. A typical load-stretch curve of a biaxial extension test of fabrics is shown in Fig.15a, which can be obtained by Kawabata Evaluation System for Fabrics (KES-F) [16]. The initial part of the curve is relatively compliant and it corresponds to the yarn decrimping, i.e. the curvatures of yarns decreasing as the yarns are being straightened by the tension. Then the fabric shows much stiffer responses in which the yarns are actually stretched. In addition, since the yarn densities along the warp and the weft direction generally differ, the tensile behaviors along the two directions are generally different and exhibit anisotropy.

In addition to nonlinearity, woven fabrics also exhibit hysteresis. A load-deformation curve of a fabric bending test is sketched in Fig.15c, from which one may notice that energy is dissipated when the fabric is subjected to a loading and unloading loop. Similar behavior can also be observed in the in-plane shear test as shown in Fig.15b. The dissipative behavior of woven fabrics is due to the frictions between and

within yarns. From Fig.15b, one may also notice that the fabric stiffens as the shear

angle increases. This is due to a phenomenon called locking, where yarns jam against

each other and further loading induces deformation of yarns' cross sections.

According to the brief introduction given above, we know that factors on the

mesoscale such as decrimping, locking and friction, significantly affect macroscale fabric

behaviors. Ideally, a realistic fabric constitutive relationship should include all these

factors and a complete mesoscale yarn structure model is the key in predicting the

complex fabric behaviors. In the following sections, some of these models are reviewed.

Most of them are confined to the prediction of elastic behaviors and the plain weave

pattern is considered for simplicity.
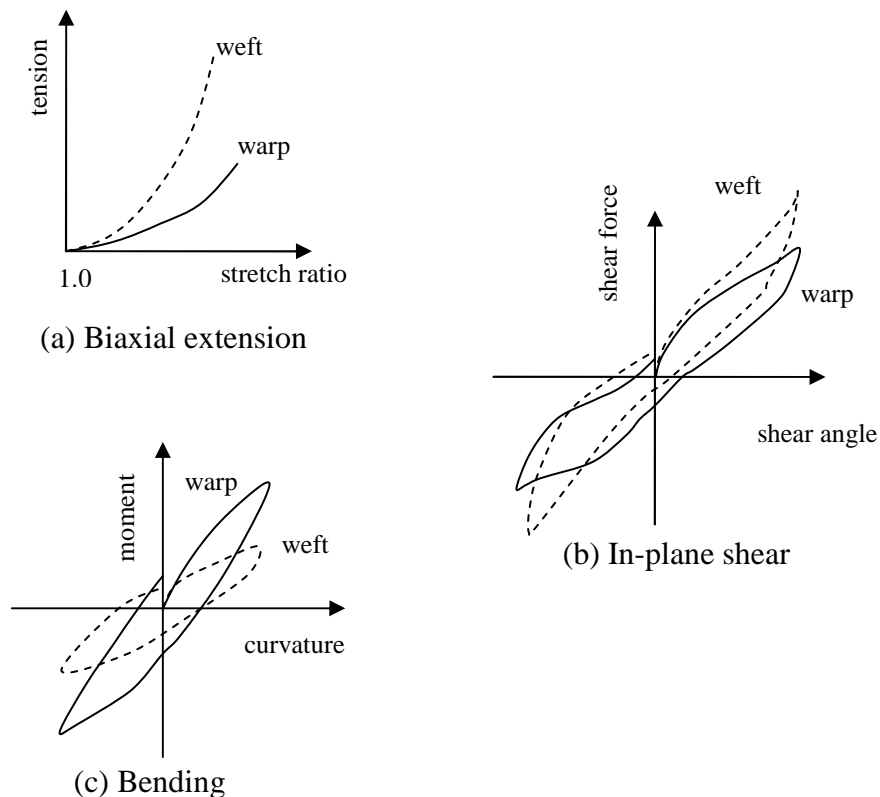
Figure 15: Typical fabric behaviors

4.1.2 Simplified mesoscale fabric models

4.1.2.1 Spatial structure models

In 1973, Kawabata et al [46-48] constructed a three-dimensional structural model to predict the mechanical properties of plain-weave fabrics made of various types of yarns. In their model, the mechanical properties of constituent yarns and the geometrical parameters characterizing the weave structures are taken as input and the fabric in-plane deformation behaviors, such as the biaxial extension, the uniaxial extension and the in-plane shear, are computed. Good agreement between their predictions and experiment data were achieved.

A unit structure as shown in Fig.16b was chosen to approximate the actual yarn structure at the crossing point (Fig.16a). The curvature and the cross section of yarns were neglected and yarns were modeled as straight segments joined at the cross points. A coordinate system was set at a cross point of two yarns with axes X_1 and X_2 align with the yarn directions and axis X_3 perpendicular to the plane OX_1X_2. The initial configuration of the structure was described by the following parameters:

- y_{0i} initial yarn spacing,
- l_{0i} initial yarn length,
- θ_{0i} the angle between yarn i and X_3 axis at initial configuration,
- h_{mi} crimp height, i.e. the amplitude of the wave of yarn i at initial configuration,

where $i = 1,2$ indicating the warp and the weft direction respectively. These parameters can be determined by yarn densities and crimp ratios, two sets of parameters measured from fabric specimens.

Suppose a fabric specimen is loaded by biaxial extension with stretch ratios of λ_1 and λ_2 along X_1 and X_2 directions, respectively. Due to decrimping, the yarns deflect

by h_1 and h_2 at the crossing point, as shown in Fig.17. From the deformed

configuration, one can compute the stretch ratios of yarns as follows:

$$\lambda_{y1} = \frac{\sqrt{4(h_{m1} - h_1)^2 + (\lambda_1 y_{01})^2}}{\sqrt{4h_{m1}^2 + y_{01}^2}}$$

$$\lambda_{y2} = \frac{\sqrt{4(h_{m2} + h_2)^2 + (\lambda_2 y_{02})^2}}{\sqrt{4h_{m2}^2 + y_{02}^2}} \tag{4.1}$$

The angles between yarns and X_3 axis change due to the decrimping as well and the new

angles can be evaluated as follows

$$\cos\theta_1 = \frac{2(h_{m1} - h_1)}{\sqrt{4(h_{m1} - h_1)^2 + (\lambda_1 y_{01})^2}}$$

$$\cos\theta_2 = \frac{2(h_{m2} + h_2)}{\sqrt{4(h_{m2} + h_2)^2 + (\lambda_2 y_{02})^2}} \tag{4.2}$$

(a) A sketch of a realistic yarn structure

(b) Kawabata's yarn structure model
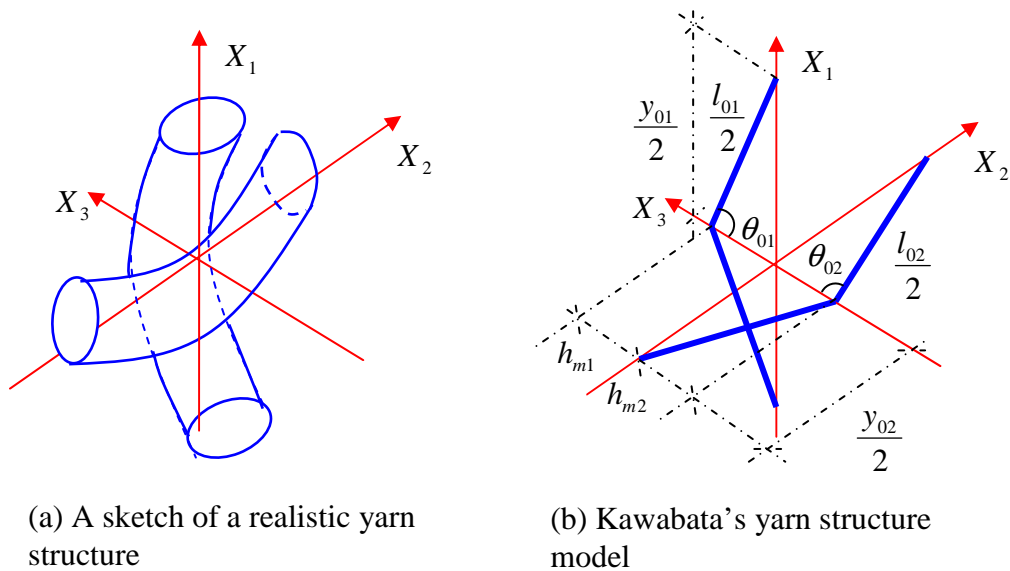
Figure 16: Kawabata's yarn structure model
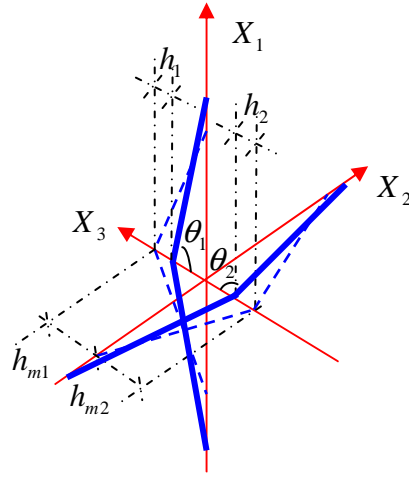
Figure 17: The deformed configuration of Kawabata's yarn structure model

For biaxial extension, Kawataba et al. neglected the bending in the yarns and assumed that the yarns are subjected to axial tension, which were generally written as a function of yarn stretch ratio as

$$F_{Ti} = g_i(\lambda_{yi}). \tag{4.3}$$

With this assumption, the force equilibrium at the cross point yields two equations

$$F_c = 2g_1(\lambda_{y1})\cos\theta_1 = 2g_2(\lambda_{y2})\cos\theta_2, \tag{4.4}$$

where F_c is the compression force between the yarns due to contact. Since this force is related to the deformation of yarn under lateral compression, another yarn property function was introduced, which reads as

$$\delta_{Di} = \phi_i(F_c), \tag{4.5}$$

where δ_{Di} denotes the decrease in the thickness of yarn i under the application of F_c. Then the total change of the crimp height of two contacting yarns are thus evaluated as

$$\Phi(F_c) = \frac{1}{2}\{\phi_1(F_c) + \phi_2(F_c)\}, \tag{4.6}$$

which relates to the yarn deflection as

$$h_2 = h_1 - \Phi(F_c). \tag{4.7}$$

Experiments were proposed and conducted by Kawabata et al. to determine the yarn axial extension and lateral compression behaviors, namely the functions given in (4.3) and (4.5).

For a given biaxial load case (λ_1, λ_2), Equation (4.4) and (4.7) can be solved simultaneously for h_1, h_2 and F_c, with which the yarn tensile forces along X_1 and X_2 axes can be obtained by taking the projections as

$$F_i = F_{Ti} \sin \theta_i, \tag{4.8}$$

and the forces per unit length of fabric are thus given by

$$f_i = n_i F_i, \tag{4.9}$$

where n_i is the number of i-yarns per unit length in the fabric. In their paper, Kawabata et al. proposed a graphical method to solve the equations and good agreements between the model prediction and experiment results were obtained for plain-weave fabrics made of different yarns and various weave structures.

For uniaxial extension, some modifications were made to capture the initial decrimping response of fabrics. The bending and the transverse shear deformation of the yarns in the free direction were included. Yarns were still assumed to remain straight, i.e. an infinite large bending rigidity associated with the yarns and the bending was measured by the change of the angle θ_i. The transverse shear was related to the friction between fibers and the hysteresis was thus included.

In order to model the in-plane shear behavior, the torque required to change the shear angle was considered and it was approximated as a linear function with its

coefficient experimentally determined. Frictional terms were included in the torque definition, which enables the model to predict the hysteresis response of fabrics. The combined biaxial and shear loading was modeled and resultant forces were computed from equilibrium conditions.

In their papers, Kawabata et al. treated different load cases separately and different formulations and solution methods were adopted for each. To be used as a constitutive relationship, Kawabata's model needs to be generalized to include all possible different loadings. One possible solution is to model the yarn structure as a spatial truss system with tension members modeling yarn stretching and compression members modeling lateral yarn compression. To include the yarn bending and the resistance to in-plane shear deformation, bending and tensional springs can be added to the system. When certain fabric strain is applied, based on the equilibrium of the system the resultant forces can be computed, from which the fabric stress can be evaluated.

An example of such an extension based on Kawabata's model was given by King et al. [50], who used the same unit cell as proposed by Kawabata et al. (Fig.16b) was used. In addition to yarn stretch, bending, lateral compression and the friction between yarns, which had been considered in Kawabata's model, locking was captured by using locking trusses. Due to the relative complexity of their structural model, the equilibrium configurations were found by minimizing the total strain energy in the system.

4.1.2.2 Interacting elastica models

Instead of using simplified spatial truss model like Kawabata's model, De Jong and Postle [51-54] proposed a continuous model based on energy analysis and optimal control theory. The strain energy of an interwoven yarn structure was first formulated including the bending, torsion, lateral compression and axial extension of individual yarns, and then the configuration and the internal forces and moments of the structure

were obtained by minimizing the strain energy. In their model, a single yarn is treated as an elastica. The strain energy associated with yarn bending was defined as

$$\psi_b = \frac{B}{2L}\int_0^1(\kappa-\kappa_0)^2 ds,\tag{4.10}$$

where κ is the curvature of the yarn; L and B denote the bending rigidity and the length of the yarn, respectively; and an initial curvature κ_0 is considered. The tensile strain energy is formulated as

$$\psi_t = \frac{EL}{2}\int_0^1(\lambda-1)^2 ds,\tag{4.11}$$

where E denotes the Young's modulus of the yarn and λ is the stretch ratio. The yarn interaction is considered by a compression strain energy as follows

$$\psi_c = C\left(\frac{d_0}{d}\right)^a,\tag{4.12}$$

where C is the yarn transverse compression rigidity, a the yarn compression index, and d_0 an arbitrary constant with the dimensions of length. The variable d is the perpendicular distance between two yarns. The equilibrium state of the interacting elastica structure is determined by minimizing the total strain energy in the system.

A similar energy-based model was introduced by Taban and Luo in [55]. In their model, yarns were assumed to be in sinusoidal shape and the constitutive equations were derived from the strain energy of the yarns, which included axial deformation and flattening of yarns. Fabric properties under uniaxial extension were predicted and good correlation between the predictions and experiments were found.

4.1.2.3 Discussions

The models reviewed above are representative analytical efforts to predict the mechanical properties of fabrics based on the underlying mesoscale yarn structure. They

demonstrate the correlation between the fabric behaviors and the mesoscale yarn structures and indicate the effectiveness of the micromechanical material modeling technique for woven fabrics. Nevertheless, these models lack generality due to their over-simplified representations of yarn geometries and their treatment of yarn interactions. In most of the models, a yarn is represented as either a straight line segment or a curve along the centerline and the yarn interaction is defined simply by a spring component. It is difficult to relate such models to real yarn structures and to identify appropriate model parameters.

In the following, a more sophisticated mesoscale yarn structure is developed, where realistic three-dimensional yarn geometries are considered and the yarn interactions are treated using general multi-body frictional contact computations. And the relationship between the mesoscale yarn interactions and the macroscale fabric behaviors is studied and presented by utilizing computational homogenization and unit cell analysis techniques.

4.2 Computational homogenization

Computational homogenization theory based on two-scale asymptotic expansion is introduced in this section. Since only two scales are considered in the discussion of the two-scale expansion, the terminology *macroscale* and *microscale* will be adopted. However, it should be advised that when applied to study fabrics mechanics the two scales actually correspond to the *macroscale* fabrics and the *mesoscale* yarn structures, respectively.

4.2.1 Two-scale expansion of a one-dimension linear elasticity problem

Consider a one-dimensional linear elasticity problem in a heterogeneous medium. Assume that the heterogeneity is periodic and is observed on a small length scale characterized by parameter λ. The governing equation is

$$\frac{d}{dx}\left[E^{\lambda}(x)\frac{du^{\lambda}(x)}{dx}\right]+\gamma^{\lambda}(x)=0, \tag{4.13}$$

where E^{λ} and γ^{λ} denote the Young's modulus and the body force, respectively. The periodicity of the material heterogeneity admits

$$E^{\lambda}(x)=E^{\lambda}(x+nX) \text{ and } \gamma^{\lambda}(x)=\gamma^{\lambda}(x+nX), \tag{4.14}$$

where n is an arbitrary integer and X denotes the period. Due to the discrepancy between the length scales of the medium and the material heterogeneity, a microscale measure is usually introduced, which is defined as

$$y=x/\lambda. \tag{4.15}$$

All quantities can thus be described in terms of two spatial length scales, the macroscale characterized by x and the microscale characterized by y. Since the material properties are macroscopically uniform and vary only on the microscale, one has

$$E^{\lambda}(x)=E^{\lambda}(x,y)=E(y) \text{ and } \gamma^{\lambda}(x)=\gamma^{\lambda}(x,y)=\gamma(y), \tag{4.16}$$

where both $E(y)$ and $\gamma(y)$ are Y- periodic, i.e.

$$E(y)=E(y+nY) \text{ and } \gamma(y)=\gamma(y+nY) \tag{4.17}$$

with $Y=X/\lambda$.

According to two-scale asymptotic expansion, the displacement field can be written as follows

$$u^{\lambda}(x)=u^{0}(x,y)+\lambda u^{1}(x,y), \tag{4.18}$$

where $u^{0}(x,y)$ gives the macroscopic displacement field while $u^{1}(x,y)$ describes the oscillatory displacement on the microscale. Both $u^{0}(x,y)$ and $u^{1}(x,y)$ are Y- periodic. Substituting Equation (4.18) into (4.13) and collecting the terms of the same scale, i.e. the power of λ, governing equations associated with different length scales are obtained. For λ^{-2}, one has

$$\frac{\partial}{\partial y}\left[E(y)\frac{\partial u^{0}(x,y)}{\partial y}\right]=0, \tag{4.19}$$

which indicates that

$$u^0(x, y) = u^0(x).$$
(4.20)

For the terms associated with λ^{-1}, one has

$$\frac{\partial}{\partial y}\left[E(y)\left(\frac{\partial u^0(x, y)}{\partial x} + \frac{\partial u^1(x, y)}{\partial y}\right)\right] = 0.$$
(4.21)

By introducing the total microscale strain $\varepsilon(x, y)$ and stress $\sigma(x, y)$, a microscale

problem is revealed, which is governed by the following equations

$$\left.\begin{aligned}\frac{\partial \sigma(x, y)}{\partial y} &= 0 \\ \sigma(x, y) &= E(y)\varepsilon(x, y) \\ \varepsilon(x, y) &= \frac{\partial u^0(x, y)}{\partial x} + \frac{\partial u^1(x, y)}{\partial y}\end{aligned}\right\}$$
(4.22)

The terms associated with λ^0 yield

$$\frac{\partial}{\partial x}\left[E(y)\left(\frac{\partial u^0(x, y)}{\partial x} + \frac{\partial u^1(x, y)}{\partial y}\right)\right] + \frac{\partial}{\partial y}\left[E(y)\frac{\partial u^1(x, y)}{\partial x}\right] + \gamma(y) = 0.$$
(4.23)

Integrating both sides over the period Y, the second term in Equation (4.23) vanishes due

to the Y-periodicity of both $E(y)$ and $u^1(x, y)$, and the governing equations for the

macroscale problem are obtained:

$$\left.\begin{aligned}\frac{d\Sigma(x)}{dx} + \tilde{\gamma} &= 0 \\ \Sigma(x) &= \frac{1}{Y}\int_Y \sigma(x, y)dy \\ \tilde{\gamma} &= \frac{1}{Y}\int_Y \gamma(y)dy\end{aligned}\right\},$$
(4.24)

where $\Sigma(x)$ is the macroscale stress, which is determined by the volume average of the

total microscale stress field given by (4.22)$_2$. A macroscale strain is usually defined in a

similar way by the volume average of total microscale strain,

$$\mathrm{E}(x) = \frac{1}{Y}\int_Y \varepsilon(x, y)dy \,. \tag{4.25}$$

As $u^1(x, y)$ is Y-periodic, it can be verified that

$$\mathrm{E}(x) = \frac{\partial u^0}{\partial x} = \frac{du^0}{dx}, \tag{4.26}$$

where the second equation is deduced from Equation (4.20).

With the two-scale expansion, the original problem in the heterogeneous medium given in (4.13) is decomposed into two separate problems: Equation (4.24) for the macroscale and Equation (4.22) for the microscale. On the macroscale, homogenized quantities independent of the microscale measure y are employed and the material heterogeneity thus becomes invisible. The relation between the macroscale stress $\Sigma(x)$ and strain $\mathrm{E}(x)$ is not explicitly given in (4.24). Instead, it is determined by the microscale problem (4.22), in which for a given macroscale strain $\mathrm{E}(x)$, the microscopic displacement field $u^1(x, y)$ is solved and the total microscale stress field $\sigma(x, y)$ is then integrated yielding the macroscopic stress response $\Sigma(x)$.

Combining (4.20) with (4.21), one has

$$\frac{\partial}{\partial y}\left[E(y)\frac{\partial u^1(x, y)}{\partial y}\right] = -\frac{dE(y)}{dy}\frac{du^0}{dx}, \tag{4.27}$$

which implies the following decomposition for the microscale displacement

$$u^1(x, y) = \chi(y)\frac{du^0(x)}{dx} + \xi(x) \tag{4.28}$$

where $\chi(y)$ is called the characteristic displacement. According to (4.27), the characteristic displacement can be determined independent of du^0/dx by solving

$$\frac{d}{dy}\left[E(y)\left(1 + \frac{d\chi(y)}{dy}\right)\right] = 0 \,. \tag{4.29}$$

Once $\chi(y)$ is determined, according to (4.22)$_2$ and (4.22)$_3$, the total microscale stress is given by

$$\sigma(x, y) = E(y)\left(1 + \frac{d\chi(y)}{dy}\right)\frac{du^0(x)}{dx}. \tag{4.30}$$

The volume average of Equation (4.30) yields the following homogenized macroscopic constitutive relation

$$\Sigma(x) = \tilde{E} \cdot \mathrm{E}(x), \tag{4.31}$$

with the homogenized Young's modulus

$$\tilde{E} = \frac{1}{Y}\int_Y E(y)\left(1 + \frac{d\chi(y)}{dy}\right)dy. \tag{4.32}$$

4.2.2 General two-scale expansion

The two-scale expansion can be readily extended to general three-dimensional elasticity problems. The equilibrium of a heterogeneous medium residing in a domain $\Omega^\lambda \subset \mathbb{R}^{nsd}$ is governed by the following equations:

$$\left.\begin{aligned}
\operatorname{div}\boldsymbol{\sigma}^\lambda + \rho^\lambda \mathbf{b} &= \mathbf{0} \text{ in } \Omega^\lambda \\
\boldsymbol{\sigma}^\lambda \cdot \mathbf{n} &= \overline{\mathbf{t}} \text{ on } \Gamma_t \\
\mathbf{u}^\lambda &= \overline{\mathbf{u}} \text{ on } \Gamma_u
\end{aligned}\right\}, \tag{4.33}$$

where Γ_t and Γ_u denote the natural and essential boundaries, respectively. The superscript λ again indicates the representative dimension of the heterogeneities. Assume that the constitutive law of the heterogeneous medium is elastic, one has

$$\begin{aligned}
\boldsymbol{\sigma}^\lambda &= \frac{\partial W^\lambda}{\partial \boldsymbol{\varepsilon}^\lambda}, \\
\boldsymbol{\varepsilon}^\lambda &= \nabla^s \mathbf{u}^\lambda
\end{aligned} \tag{4.34}$$

where $W^\lambda\left(\mathbf{x}, \boldsymbol{\varepsilon}^\lambda\right)$ is the stored energy and $\nabla^s \mathbf{u}^\lambda = \left[\nabla\mathbf{u}^\lambda + \left(\nabla\mathbf{u}^\lambda\right)^T\right]\Big/2$ is the infinitesimal strain.

By introducing a microscale measure $\mathbf{y} = \mathbf{x}/\lambda$, the displacement field can be written as a two-scale expansion $\mathbf{u}^\lambda(\mathbf{x}) = \mathbf{u}^0(\mathbf{x}) + \lambda\mathbf{u}^1(\mathbf{x}, \mathbf{y})$. The problem can then be decomposed into separate problems on two length scales. On the microscale, the

problem is to determine the field variables $\{\mathbf{u}^1(\mathbf{x},\mathbf{y}), \boldsymbol{\varepsilon}(\mathbf{x},\mathbf{y}), \boldsymbol{\sigma}(\mathbf{x},\mathbf{y})\}$ in a unit cell $\mathbb{Y}$ such that

$$\left.\begin{aligned} \operatorname{div}_\mathbf{y} \boldsymbol{\sigma} &= \mathbf{0} \text{ in } \mathbb{Y} \\ \boldsymbol{\sigma}(\mathbf{x},\mathbf{y}) &= \frac{\partial W(\mathbf{x},\boldsymbol{\varepsilon})}{\partial \boldsymbol{\varepsilon}} \\ \boldsymbol{\varepsilon}(\mathbf{x},\mathbf{y}) &= \nabla_\mathbf{x}^s \mathbf{u}^0 + \nabla_\mathbf{y}^s \mathbf{u}^1 \end{aligned}\right\}. \tag{4.35}$$

On the macroscale, a homogenized version of the original problem (4.33) is constructed. The macroscopic field variables are $\{\mathbf{u}^0(\mathbf{x}), \mathbf{E}(\mathbf{x}), \boldsymbol{\Sigma}(\mathbf{x})\}$ and the governing equations are as follows

$$\left.\begin{aligned} \operatorname{div}_\mathbf{x} \boldsymbol{\Sigma} + \tilde{\rho}\mathbf{b} &= \mathbf{0} \text{ in } \Omega \\ \boldsymbol{\Sigma}(\mathbf{x}) &= \frac{1}{|\mathbb{Y}|} \int_\mathbb{Y} \boldsymbol{\sigma}(\mathbf{x},\mathbf{y})dV \\ \tilde{\rho}(\mathbf{x}) &= \frac{1}{|\mathbb{Y}|} \int_\mathbb{Y} \rho(\mathbf{x},\mathbf{y})dV \end{aligned}\right\}, \tag{4.36}$$

where $|\mathbb{Y}|$ denotes the volume of the unit cell. A macroscale strain can be defined as the volume average of the microscale strain field, i.e.

$$\mathbf{E}(\mathbf{x}) = \frac{1}{|\mathbb{Y}|} \int_\mathbb{Y} \boldsymbol{\varepsilon}(\mathbf{x},\mathbf{y})dV. \tag{4.37}$$

It can be verified that since $\mathbf{u}^1(\mathbf{x},\mathbf{y})$ is Y-periodic the volume average of $\nabla_\mathbf{y}\mathbf{u}^1$ vanishes and

$$\mathbf{E}(\mathbf{x}) = \nabla_\mathbf{x}^s \mathbf{u}^0. \tag{4.38}$$

The microscale problem (4.35) can be treated as the homogenized constitutive law for the macroscale problem (4.36). Given a macroscopic strain $\mathbf{E}(\mathbf{x})$, the microscopic displacement $\mathbf{u}^1(\mathbf{x},\mathbf{y})$ and stress $\boldsymbol{\sigma}(\mathbf{x},\mathbf{y})$ are determined by solving (4.35). The volume average of $\boldsymbol{\sigma}(\mathbf{x},\mathbf{y})$, i.e. the macroscopic stress $\boldsymbol{\Sigma}(\mathbf{x})$, is then returned to the macroscale problem, yielding the stress response to the applied strain $\mathbf{E}(\mathbf{x})$.

For linear elasticity, a *Y*-periodic linear elasticity tensor $\mathbf{c}(\mathbf{y})$ exists and the microscale constitutive relation given in Equation (4.35)$_2$ can be written as

$$\boldsymbol{\sigma}(\mathbf{x},\mathbf{y}) = \mathbf{c}(\mathbf{y}):\boldsymbol{\varepsilon}(\mathbf{x},\mathbf{y}).\tag{4.39}$$

And the microscale problem is thus to find *Y*-periodic displacement field $\mathbf{u}^1(\mathbf{x},\mathbf{y})$ such that

$$\frac{\partial}{\partial y_j}\left[c_{ijkl}(\mathbf{y})\left(\frac{\partial u_k^0(\mathbf{x})}{\partial x_l} + \frac{\partial u_k^1(\mathbf{x},\mathbf{y})}{\partial y_l}\right)\right] = 0,\tag{4.40}$$

or

$$\frac{\partial}{\partial y_j}\left[c_{ijkl}(\mathbf{y})\frac{\partial u_k^1(\mathbf{x},\mathbf{y})}{\partial y_l}\right] = -\frac{\partial c_{ijkl}(\mathbf{y})}{\partial y_j}\frac{\partial u_k^0(\mathbf{x})}{\partial x_l}.\tag{4.41}$$

Equation (4.41) implies that $\mathbf{u}^1(\mathbf{x},\mathbf{y})$ can be decoupled as follows

$$u_k^1(\mathbf{x},\mathbf{y}) = \chi_k^{pq}(\mathbf{y})\frac{\partial u_p^0(\mathbf{x})}{\partial x_q} + \xi_k(\mathbf{x}),\tag{4.42}$$

where $\chi_k^{pq}(\mathbf{y})$ is the characteristic displacement associated with the macroscopic strain component $\partial u_p^0(\mathbf{x})/\partial x_q$ and it is determined by solving

$$\frac{\partial}{\partial y_j}\left[c_{ijkl}(\mathbf{y})\frac{\partial \chi_k^{pq}(\mathbf{y})}{\partial y_l}\right] = -\frac{\partial c_{ijpq}(\mathbf{y})}{\partial y_j}.\tag{4.43}$$

The homogenized constitutive law, i.e. the volume average of Equation (4.39), reads

$$\Sigma_{ij} = \tilde{c}_{ijpq}\mathrm{E}_{pq},\tag{4.44}$$

where

$$\tilde{c}_{ijpq} = \frac{1}{|\mathbb{Y}|}\int_{\mathbb{Y}} c_{ijkl}(\mathbf{y})\left(\delta_{kp}\delta_{lq} + \frac{\partial \chi_k^{pq}(\mathbf{y})}{\partial y_l}\right)dV$$

$$\Sigma_{ij} = \frac{1}{|\mathbb{Y}|}\int_{\mathbb{Y}} \sigma_{ij}(\mathbf{x},\mathbf{y})dV\tag{4.45}$$

$$\mathrm{E}_{pq} = \frac{1}{|\mathbb{Y}|}\int_{\mathbb{Y}} \varepsilon_{pq}(\mathbf{x},\mathbf{y})dV = \frac{\partial u_p^0(\mathbf{x})}{\partial x_q}$$

For the volume average of the microscopic strain $\mathbf{E}$ to be equal to the imposed macroscopic strain $\nabla_{\mathbf{x}}^s \mathbf{u}^0$, i.e.

$$\mathbf{E} = \frac{1}{|\mathbb{Y}|} \int_{\mathbb{Y}} \boldsymbol{\varepsilon}(\mathbf{x}, \mathbf{y}) dV = \frac{1}{|\mathbb{Y}|} \int_{\mathbb{Y}} \left(\nabla_{\mathbf{x}}^s \mathbf{u}^0 + \nabla_{\mathbf{y}}^s \mathbf{u}^1 \right) dV = \nabla_{\mathbf{x}}^s \mathbf{u}^0$$

the volume integral of the gradient of the microscopic displacement has to vanish, i.e.

$$\int_{\mathbb{Y}} \nabla_{\mathbf{y}}^s \mathbf{u}^1 dV = 0. \tag{4.46}$$

The condition (4.46) is satisfied if $\mathbf{u}^1(\mathbf{x}, \mathbf{y})$ is Y- periodic. However, if the periodic boundary condition is not enforced on a unit cell or if there are interior boundaries within a unit cell, (4.46) may not be satisfied. Consider a unit cell with an exterior boundary $\partial \mathbb{Y}^0$ and an interior boundary $\partial \mathbb{Y}^1$ and assume that periodic condition is enforced on $\partial \mathbb{Y}^0$. According to the divergence theorem, the volume integral of the gradient of the microscopic displacement can be written as follows

$$\int_{\mathbb{Y}} \nabla_{\mathbf{y}} \mathbf{u}^1 dV = \int_{\mathbb{Y}} \frac{\partial u_i^1}{\partial y_j} dV = \int_{\partial \mathbb{Y}^0} u_i^1 n_j dS + \int_{\partial \mathbb{Y}^1} u_i^1 n_j dS, \tag{4.47}$$

where the first term on the right hand side vanishes due to the periodic boundary condition on $\partial \mathbb{Y}^0$ while the integral on $\partial \mathbb{Y}^1$ is generally nonzero. The volume average of the microscopic strain is thus equal to the summation of the prescribed macroscopic strain $\nabla_{\mathbf{x}}^s \mathbf{u}^0$ and the contribution of the microscopic displacement along the interior boundary, i.e.

$$\frac{1}{|\mathbb{Y}|} \int_{\mathbb{Y}} \boldsymbol{\varepsilon}(\mathbf{x}, \mathbf{y}) dV = \nabla_{\mathbf{x}}^s \mathbf{u}^0 + \frac{1}{|\mathbb{Y}|} \int_{\partial \mathbb{Y}^1} \frac{1}{2} \left(u_i^1 n_j + n_i u_j^1 \right) dS. \tag{4.48}$$

4.3 Unit cell analysis of mesoscale yarn structures

4.3.1 Computational homogenization with

finite deformation

The computational homogenization approach presented in the previous section is based on infinitesimal strain, which is not applicable for problems with finite deformation and/or rotation. The yarn interaction problem in textiles involves nonlinearities in both kinematic relationships and material properties and thus it is important to include finite deformation in the formulation of the problem. For this purpose, the computational homogenization approach is extended here to include the finite deformation effect.

Consider a medium with periodic heterogeneities of a fine representative size λ. The reference configuration of the heterogamous medium is denoted by Ω^λ and a material point is given by $\mathbf{X}^\lambda \in \Omega^\lambda$. A deformation is a one-to-one mapping $\varphi^\lambda \left(\Omega^\lambda \right)$ and a spatial point is a result of the mapping $\mathbf{x}^\lambda = \varphi^\lambda \left(\mathbf{X}^\lambda \right)$. By introducing a microscale $\mathbf{Y} = \mathbf{X}/\lambda$, the heterogeneous domain Ω^λ can be decomposed as $\Omega \times \mathbb{Y}$, where Ω is a homogenized domain on the original length scale, i.e. macroscale, and $\mathbb{Y}$ represents the microscale, where the heterogeneities are observed. $\mathbb{Y}$ is usually called a unit cell and it corresponds to a material point in Ω. The two-scale expansion of the reference and deformed configuration can be written, respectively, as

$$
\begin{aligned}
\mathbf{X}^\lambda &= \mathbf{X} + \lambda \mathbf{Y}, \\
\mathbf{x}^\lambda \left(\mathbf{X}^\lambda \right) &= \mathbf{x}(\mathbf{X}) + \lambda \mathbf{y}(\mathbf{X}, \mathbf{Y}).
\end{aligned}
\tag{4.49}
$$

The displacement involves both a macro- and a micro- part:

$$
\mathbf{u}^\lambda \left(\mathbf{X}^\lambda \right) = \mathbf{u}^0 (\mathbf{X}) + \lambda \mathbf{u}^1 (\mathbf{X}, \mathbf{Y}),
\tag{4.50}
$$

where $\mathbf{u}^0 (\mathbf{X}) = \mathbf{x}(\mathbf{X}) - \mathbf{X}$ and $\mathbf{u}^1 (\mathbf{X}, \mathbf{Y}) = \mathbf{y}(\mathbf{X}, \mathbf{Y}) - \mathbf{Y}(\mathbf{X})$. Assume that the macroscopic deformation gradient is

$$\mathbf{\Phi}(\mathbf{X}) = \frac{\partial \mathbf{x}(\mathbf{X})}{\partial \mathbf{X}}, \tag{4.51}$$

the microscopic deformed configuration can be written as

$$\mathbf{y}(\mathbf{X}, \mathbf{Y}) = \mathbf{\Phi}(\mathbf{X}) \cdot \mathbf{Y} + \mathbf{u}^*(\mathbf{X}, \mathbf{Y}), \tag{4.52}$$

where $\mathbf{u}^*(\mathbf{X}, \mathbf{Y})$ is a oscillatory displacement field due to the heterogeneity within the unit cell $\mathbb{Y}$. The total microscopic displacement is

$$\mathbf{u}^1(\mathbf{X}, \mathbf{Y}) = \left[\mathbf{\Phi}(\mathbf{X}) - \mathbf{1} \right] \cdot \mathbf{Y} + \mathbf{u}^*(\mathbf{X}, \mathbf{Y}). \tag{4.53}$$

And the microscopic deformation gradient in $\mathbb{Y}$ reads

$$\mathbf{F} = \mathbf{\Phi}(\mathbf{X}) + \mathbf{F}^*(\mathbf{X}, \mathbf{Y}), \tag{4.54}$$

where

$$\mathbf{F}^*(\mathbf{X}, \mathbf{Y}) = \frac{\partial \mathbf{u}^*(\mathbf{X}, \mathbf{Y})}{\partial \mathbf{Y}} \tag{4.55}$$

Since $\mathbf{u}^*$ is Y- periodic, the volume integral of $\mathbf{F}^*$ over $\mathbb{Y}$ vanishes and the volume average of the total deformation given in Equation (4.54) is equal to the macroscopic one, i.e.

$$\frac{1}{|\mathbb{Y}|} \int_{\mathbb{Y}} \mathbf{F} dV = \mathbf{\Phi}. \tag{4.56}$$

However, if periodic boundary conditions are not prescribed on the exterior boundaries or there exist interior boundaries, Equation (4.56) does not hold.

On the microscale, a periodic boundary value problem is solved and the governing equations are summarized below

$$\left. \begin{aligned} \text{DIV } \mathbf{P} &= 0 \text{ in } \mathbb{Y} \\ \mathbf{P} &= \frac{\partial W(\mathbf{Y}, \mathbf{F})}{\partial \mathbf{F}} \\ \mathbf{F} &= \mathbf{\Phi}(\mathbf{X}) + \mathbf{F}^*(\mathbf{X}, \mathbf{Y}) \end{aligned} \right\}, \tag{4.57}$$

where $\mathbf{P}$ is the first Piola-Kirchhoff stress and hyperelasticity is assumed for the constitutive law of the yarns. Equation (4.57) implicitly defines the homogenized

macroscopic constitutive relationship. The computation procedure is similar to that of the infinitesimal strain case. Given a macroscopic strain $\mathbf{\Phi}$, Equation (4.57) is solved for the microscopic displacement $\mathbf{u}^*(\mathbf{X}, \mathbf{Y})$, from which the deformation $\mathbf{F}^*$ and the stress $\mathbf{P}$ are calculated. And the volume average of the stress in the unit cell gives the macroscopic stress in response to $\mathbf{\Phi}$. As a symmetrical stress measure is usually preferred, the averaged second Piola-Kirchhoff stress tensor is adopted

$$\mathbf{S}(\mathbf{X}) = \frac{1}{|\mathbb{Y}|} \int_{\mathbb{Y}} \mathbf{F}^{-1} \cdot \mathbf{P} \, dV \ . \tag{4.58}$$

The conjugate strain measure, as proved in [62], is the macroscopic Green-Lagrangian strain, which is defined by

$$\mathbf{E}(\mathbf{X}) = \frac{1}{2}\left(\mathbf{\Phi}^T \mathbf{\Phi} - \mathbf{1}\right). \tag{4.59}$$

4.3.2 Finite element implementation of the unit cell

problem

Given a macroscopic deformation gradient $\mathbf{\Phi}$, the weak form statement of (4.57) is to find $\mathbf{u}^*(\mathbf{Y})$ such that for any Y-periodic variation $\delta\mathbf{u}^*$

$$\int_{\mathbb{Y}} \mathrm{DIV} \, \mathbf{P} \cdot \delta\mathbf{u}^* \, dV = 0 \tag{4.60}$$

where

$$\mathbf{P} = \frac{\partial W(\mathbf{Y}, \mathbf{F})}{\partial \mathbf{F}} \ \text{and} \ \mathbf{F} = \mathbf{\Phi} + \frac{\partial \mathbf{u}^*}{\partial \mathbf{Y}} \ .$$

Applying the divergence theorem, (4.60) is rewritten as

$$\int_{\mathbb{Y}} \mathbf{P} : \nabla\left(\delta\mathbf{u}^*\right) dV = 0 \ \text{ or } \ \int_{\mathbb{Y}} P_{iI} \frac{\partial \delta u_i^*}{\partial Y_I} \, dV = 0 \ , \tag{4.61}$$

where the boundary integral terms vanish due to the periodicity and/or traction-free boundary conditions. Applying a finite element discretization, the displacement and its variation can be expressed as

$$u_i^* = N_A d_{Ai} \text{ and } \delta u_i^* = N_A \delta d_{Ai}, \qquad (4.62)$$

where N_A and $\mathbf{d}_A$ denote nodal shape functions and displacement, respectively. Since Equation (4.60) must hold for all admissible values of $\delta \mathbf{u}^*$, it leads to a set of discrete nodal force balance equations

$$\int_{\mathbb{Y}} \mathbf{B}^T \cdot \mathbf{P}(\mathbf{d}) dV = 0, \qquad (4.63)$$

where $\mathbf{B}$ are nodal strain displacement matrices with their components given by $B_{AI} = \partial N_A / \partial Y_I$. From Equation (4.63) the nodal displacement can be determined. The periodicity of $\mathbf{u}^*$ is enforced by requiring the displacements of corresponding nodes on opposite faces of the unit cell to be the same and this can be achieved by a nodal enslavement procedure. In the unit cell analysis given in Equation (4.63), loading occurs through a prescribed macroscopic deformation $\mathbf{\Phi}$ and it is applied by a predictor displacement field $\tilde{\mathbf{d}}(\mathbf{Y}) = [\mathbf{\Phi} - \mathbf{1}] \cdot \mathbf{Y}$ in the finite element computations.

4.3.3 Unit cell analysis of mesoscale yarn structures

Computational homogenization provides a systematic framework to study the material properties of heterogeneous media. It relates the macroscopic behaviors of a medium to its microscale heterogeneities and microscale phenomena. In this section, the computational homogenization approach just described is applied to investigate the macroscale stress-strain characteristics of woven fabrics due to the mesoscale yarn interactions. A unit cell is constructed to capture a representative yarn structure and it is loaded by prescribed macroscopic strains. The local deformation and stress in the unit cell are determined by solving the unit cell analysis problem. The relationship between the prescribed deformation and the volume average of the stress over the unit cell is interpreted as the macroscopic constitutive relationship of the woven fabric.

Various weave patterns exist and the basic ones are the *plain*, *twill* and *satin* weaves (Fig.18). Plain weave is the simplest pattern, where the weave is simply over-one and under-one for each yarn, and a cross is formed at the intersection of a warp yarn and

a weft yarn. Twill weave has an over-two and under-two pattern. Satin weave uses as few interlaces as possible and usually forms a loose structure. The fabric properties vary significantly for different weave patterns. For simplicity, the plain weave is considered in this study to illustrate the homogenization approach. However, the method presented here can be readily applied to other patterns by choosing appropriate unit cells.

(a) Plain weave   (b) Twill weave   (c) Satin weave
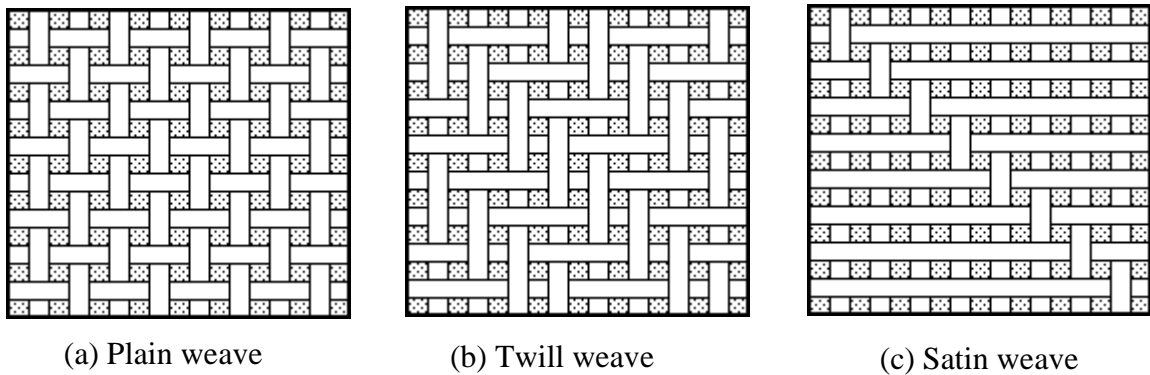
Figure 18: Basic weave patterns

For plain weave, the choice of a unit cell that is representative of the periodic yarn structure is not unique. As sketched in Fig.19a, there are multiple options in choosing a unit cell. Option A has four complete yarns and includes a full period for each yarn. It is identically repeated in space. Option B, which is a quarter of the structure of option A, includes two yarns at a cross point and is repeated anti-symmetrically about the plane. Option C covers half a period and includes four half yarns. The choice of unit cells depends on the deformation investigated and the consideration of the computational cost involved. As it involves less computational expense, option B is adopted in most computations to be presented. And a comparison between option B and A is provided as well. Pictures of the yarn structures are shown in Fig.19b and 19c.

(a) Unit cell options

(b) Unit cell of option A   (c) Unit cell of option B
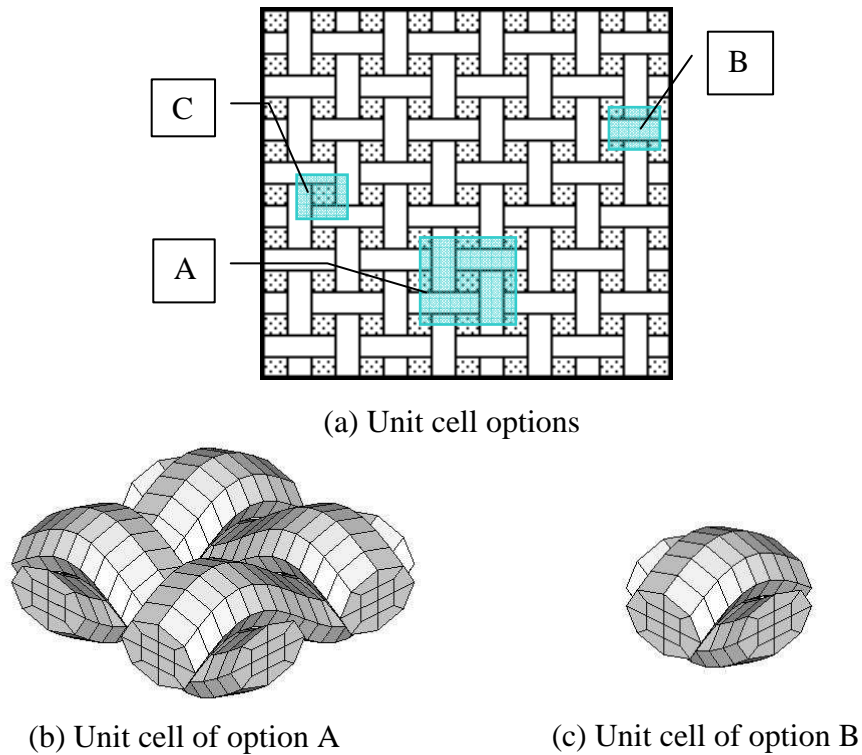
Figure 19: Multiple choices of unit cells

A large amount of voids exists in the mesoscale structures of woven fabrics and these voids make a sound definition of a unit cell quite challenging. Considering the yarn structure shown in Fig.19b, if the unit cell is defined as the bounding box and all of the contents therein, the cell boundary consists of both material boundaries and void boundaries. It is difficult to enforce appropriate boundary conditions on voids and to keep track of the change of the void configuration as the cell is loaded. In this study therefore, some assumptions are adopted to address this issue. First, the homogenized constitutive relationship is formulated using the Lagrangian description and a bounding box is defined at the initial configuration. Based on this, a volume fraction of yarns with respect to the whole cell can be determined. The macroscopic second Piola-Kirchhoff

stress, i.e. the volume average of the second Piola-Kirchhoff stress in the unit cell as given in Equation (4.58), can be calculated as follows

$$\mathbf{S} = \frac{\varphi}{|\mathbb{Y}_S|} \int_{\mathbb{Y}_S} \mathbf{F}^{-1} \cdot \mathbf{P} dV \qquad (4.64)$$

where $\mathbb{Y}_S$ denotes the domain occupied by yarns in the reference configuration and φ is yarn volume fraction in the reference configuration, i.e.

$$\varphi = \frac{|\mathbb{Y}_S|}{|\mathbb{Y}|}. \qquad (4.65)$$

For the volume integral of the microscopic strain field to vanish, periodic boundary conditions need to be specified on the unit cell. To avoid the complication of enforcing the boundary conditions on voids, periodicity is only specified on the end faces of yarns. In addition, since the in-plane behaviors are studied, the top and bottom faces are assumed to be traction-free. These boundary conditions require an extra surface integration for the microscopic strain field to vanish as discussed in (4.48). It is interesting to notice that for the surface integral of the microscopic strain can yield the strain through the thickness. In this study, since only the in-plane properties are investigated, the prescribed macroscopic deformation $\mathbf{\Phi}$ is used and the surface integral is skipped.

4.3.4 Transversely isotropic material model

Each yarn itself possesses a microscopic structure, where long continuous individual fibers are loosely bundled together to form a single continuous element. The mechanical properties of a yarn are determined by the properties of the fibers and their mechanical interactions. While this motivates a new multiscale modeling problem, which relates the microscopic fiber behaviors to the overall yarn properties, such an approach is not pursued here due to the limitation of the scope of this study. Instead, transversely isotropic hyperelastic constitutive models are used to model the yarns.

The yarn exhibits isotropic properties about the yarn longitudinal axis and the transversely isotropic hyperelastic model of Bonet and Burton [60] is adopted to describe the constitutive relation. The strain energy function is defined as a combination of an isotropic component and a transversely isotropic component.

$$\psi(\mathbf{C}) = \psi^{iso} + \psi^{ti}, \tag{4.66}$$

where $\mathbf{C} = \mathbf{F}^T\mathbf{F}$ is the right Cauchy-Green deformation tensor. The isotropic part is assumed to be Neo-Hookean and is defined as

$$\psi^{iso} = \frac{1}{2}\mu(I_1 - 3) - \mu \ln J + \frac{1}{2}\lambda(J-1)^2, \tag{4.67}$$

where $I_1 = \mathrm{tr}(\mathbf{C})$ and $J = \det(\mathbf{F}) = \left[\det(\mathbf{C})\right]^{1/2}$. Assume that the principal material direction in reference configuration is denoted by vector $\mathbf{A}$, the strain energy of the transversely isotropic part is defined as

$$\psi^{ti} = \left[\alpha + \beta \ln J + \gamma(I_4 - 1)\right](I_4 - 1) - \frac{1}{2}\alpha(I_5 - 1) \tag{4.68}$$

with $I_4 = \mathbf{A} \cdot \mathbf{C}\mathbf{A}$ and $I_5 = \mathbf{A} \cdot \mathbf{C}^2\mathbf{A}$.

The second Piola-Kirchhoff stress, $\mathbf{S} = 2\partial\psi/\partial\mathbf{C}$, has contributions from both the isotropic component and the transversely isotropic one and they read as

$$\begin{aligned}
\mathbf{S}^{iso} &= \mu(\mathbf{1} - \mathbf{C}^{-1}) + \lambda J(J-1)\mathbf{C}^{-1}, \\
\mathbf{S}^{ti} &= \beta(I_4 - 1)\mathbf{C}^{-1} + 2\left[\alpha + \beta \ln J + 2\gamma(I_4 - 1)\right]\mathbf{A} \otimes \mathbf{A} \\
&\quad -\alpha(\mathbf{A} \otimes \mathbf{C}\mathbf{A} + \mathbf{C}\mathbf{A} \otimes \mathbf{A}).
\end{aligned} \tag{4.69}$$

The Lagrangian elasticity tensor $\mathbb{D} = 2\partial\mathbf{S}/\partial\mathbf{C}$ is deduced as

$$\begin{aligned}
\mathbb{D}^{iso} &= 2\left[\mu - \lambda J(J-1)\right]\mathbb{G} + \lambda J(2J-1)\mathbf{C}^{-1} \otimes \mathbf{C}^{-1} \\
\mathbb{D}^{ti} &= 8\gamma\mathbf{A} \otimes \mathbf{A} \otimes \mathbf{A} \otimes \mathbf{A} - 2\alpha\mathbb{A} \\
&\quad +2\beta\left[\mathbf{A} \otimes \mathbf{A} \otimes \mathbf{C}^{-1} + \mathbf{C}^{-1} \otimes \mathbf{A} \otimes \mathbf{A} - (I_4 - 1)\mathbb{G}\right],
\end{aligned} \tag{4.70}$$

where

$$\mathbb{A}_{IJKL} = A_I A_L \delta_{JK} + A_J A_L \delta_{IK} \text{ and } \mathbb{G}_{IJKL} = \left(C_{IK}^{-1}C_{JL}^{-1} + C_{IL}^{-1}C_{JK}^{-1}\right)/2. \tag{4.71}$$

The Kirchhoff stress $\boldsymbol{\tau} = \mathbf{F}\mathbf{S}\mathbf{F}^T$ and the Eulerian elasticity tensor $\mathbf{c} = \mathbf{F}\mathbf{F}\mathbb{D}\mathbf{F}^T\mathbf{F}^T$ are

obtained by pushing forward the associated material quantities given in Equations (4.69)

and (4.70). The results are summarized as follows

$$\boldsymbol{\tau}^{iso} = \mu(\mathbf{b}-\mathbf{1}) + \lambda J(J-1)\mathbf{1}$$
$$\boldsymbol{\tau}^{ti} = \beta(I_4-1)\mathbf{1} + 2\left[\alpha + \beta \ln J + 2\gamma(I_4-1)\right]\mathbf{a}\otimes\mathbf{a} \qquad (4.72)$$
$$\quad -\alpha(\mathbf{a}\otimes\mathbf{ba} + \mathbf{ba}\otimes\mathbf{a}),$$

and

$$\mathbf{c}^{iso} = 2\left[\mu - \lambda J(J-1)\right]\mathbf{g} + \lambda J(2J-1)\mathbf{1}\otimes\mathbf{1}$$
$$\mathbf{c}^{ti} = 8\gamma\mathbf{a}\otimes\mathbf{a}\otimes\mathbf{a}\otimes\mathbf{a} - 2\alpha\mathbf{a} \qquad (4.73)$$
$$\quad + 2\beta\left[\mathbf{a}\otimes\mathbf{a}\otimes\mathbf{1} + \mathbf{1}\otimes\mathbf{a}\otimes\mathbf{a} - (I_4-1)\mathbf{g}\right],$$

where $\mathbf{a} = \mathbf{F}\mathbf{A}$ is the principal material direction in the deformed configuration; $\mathbf{b} = \mathbf{F}\mathbf{F}^T$

is the left Cauchy-Green deformation tensor; $\mathbf{a}$ and $\mathbf{g}$ are the push-forward of the tensor

$\mathbb{A}$ and $\mathbb{G}$ and they are given component-wise as

$$\mathbf{a}_{ijkl} = a_i a_l b_{jk} + a_j a_l b_{ik} \text{ and } \mathbf{g}_{ijkl} = \left(\delta_{ik}\delta_{jl} + \delta_{il}\delta_{jk}\right)/2 . \qquad (4.74)$$

4.3.5 Results

The results of unit cell analyses based on the yarn structure shown in Fig.21b are

compiled in this section. The in-plane properties are studied under prescribed

macroscopic deformation gradients associated with biaxial extension, uniaxial extension

and in-plane shear. The local stress fields are determined by solving the unit cell problem

in Equation (4.63) and the macroscopic stresses are obtained by Equation (4.64). Contact

constraints are enforced between the two yarns and the formulation discussed in Section

3.4 is utilized.

In this unit cell model, the centerline of a yarn is represented as a half wave of a

sinusoidal curve and two parameters are needed, i.e. the half period and the amplitude.

As introduced by Kawabata et al [46], these two parameters can be identified using the

yarn density and the crimp ratio, two measures directly taken on a given fabric specimen. The parameters of a warp yarn are usually different from those of a weft yarn, which is exactly the origin of fabrics anisotropies. For the computation presented here, however, the parameters are first assumed to be identical for both yarns, and this case herein is referred to as *a balanced weave*. The cross section of a yarn is assumed to be an ellipse with a radius ratio of 1.5.

The two yarns are initially orthogonal and aligned with the *X*- and *Y*- axis of a global Cartesian coordinate system. The macroscopic deformation is specified with respect to the global coordinate system. For example, a uniaxial extension along *X*-axis is specified as a load case where $\Phi_{11} > 1.0$ and $\Phi_{22} = 1.0$. Periodic boundary conditions are specified on the pair of end faces of each yarn and rigid body motions are precluded by applying appropriate essential boundary conditions. The volume fraction defined in Equation (4.65) is assumed to be $\varphi = 0.4$. And the homogenized relations between the macroscale Green-Lagrangian strain (4.59) and the macroscale second Piola-Kirchhoff stress (4.58) are presented.

4.3.5.1 Isotropic yarns

Instead of assuming transverse isotropy, yarns are first modeled as an isotropic material. The parameters associated with the transversely isotropic strain energy in Equation (4.68) are set to zeros and the isotropic material parameters in Equation (4.67) are chosen as $\lambda = 48.82GPa$ and $\mu = 32.55GPa$, which in an infinitesimal case recovers a Young's modulus $E = 84.62GPa$, the value of Kevlar® KM2 fibers published by Cheng and Chen [61], and a Poisson's ratio $\nu = 0.3$.

For biaxial extension, a macroscopic deformation $\left(\Phi_{11}, \Phi_{22} = 1.2\right)$ is specified and the deformed configuration is shown Fig.20b. For uniaxial extension, the unit cell is stretched along *X*-axis with a macroscopic deformation $\Phi_{11} = 1.2$ and $\Phi_{22} = 1.0$. The deformed configuration is given in Fig.20c. The homogenized stress-strain relation is

almost linear for both cases (Fig.21). It is also found that S_{11} are almost identical for both biaxial- and uniaxial- extension and that S_{22} is negligible compared to S_{11} in uniaxial extension. These facts indicate that there is little interaction between the two yarns and that the major responses in the unit cells are to decrimp the individual yarns. These observations are quite different from the expected responses of woven fabrics and the reason is due to the isotropic material model employed, where a strong shear resistance prevents the decrimping.

For in-plane shear (Fig.20d), the prescribed macroscopic deformation is $\Phi_{12} = \Phi_{21} = 0.2$. A small biaxial pre-stretching is applied to establish a firm contact between the two yarns as the shear deformation develops. The macroscopic shear stress is plotted against the deformation in Fig.22 and it is observed that S_{12} spikes as shear deformation increases, i.e. the shear locking.

(a) Undeformed configuration

(b) Biaxial extension

(c) Uniaxial extension
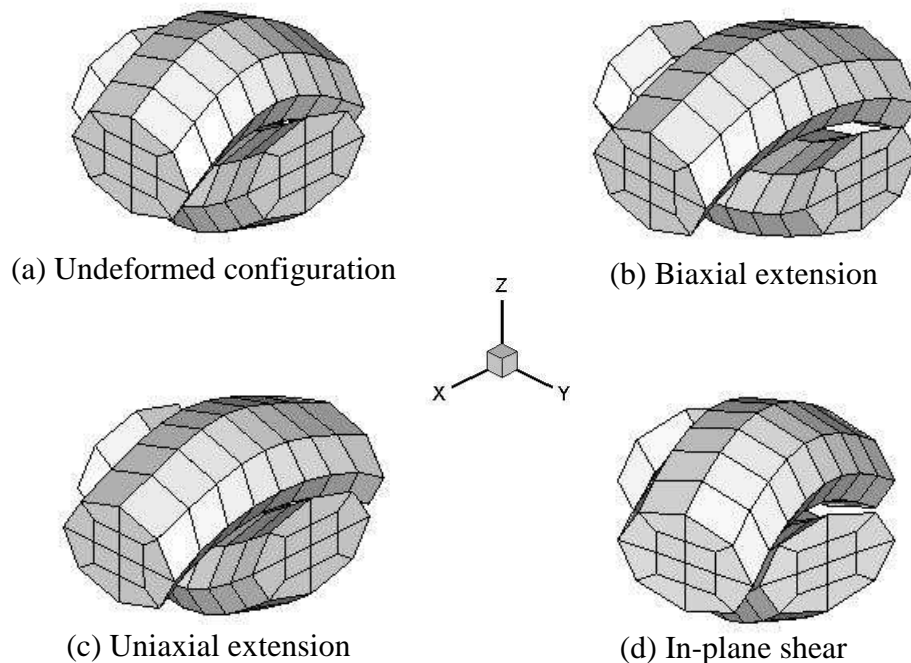
(d) In-plane shear

Figure 20: Undeformed and deformed configurations of a balanced weave with isotropic yarns
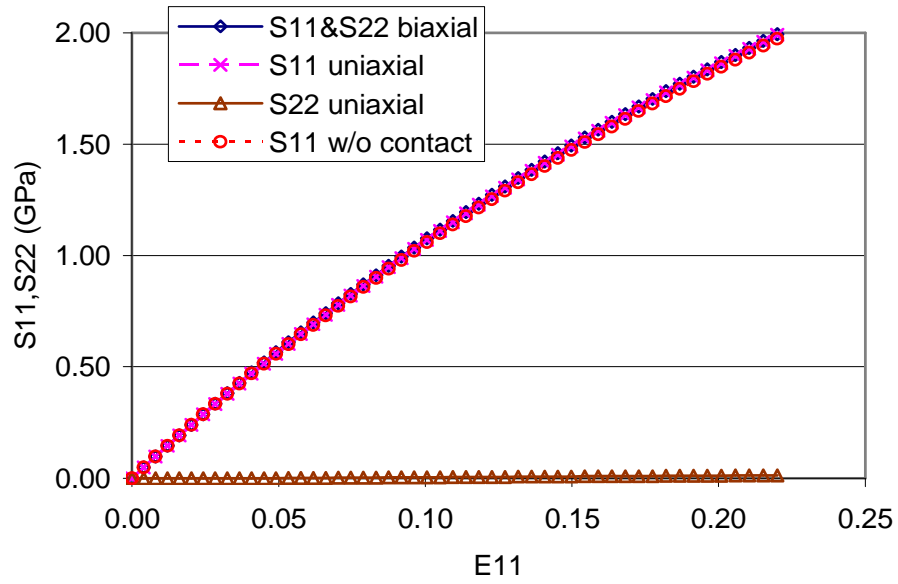
Figure 21: S_{11} and S_{22} vs. E_{11} for biaxial and uniaxial extension of a balanced weave with isotropic yarns
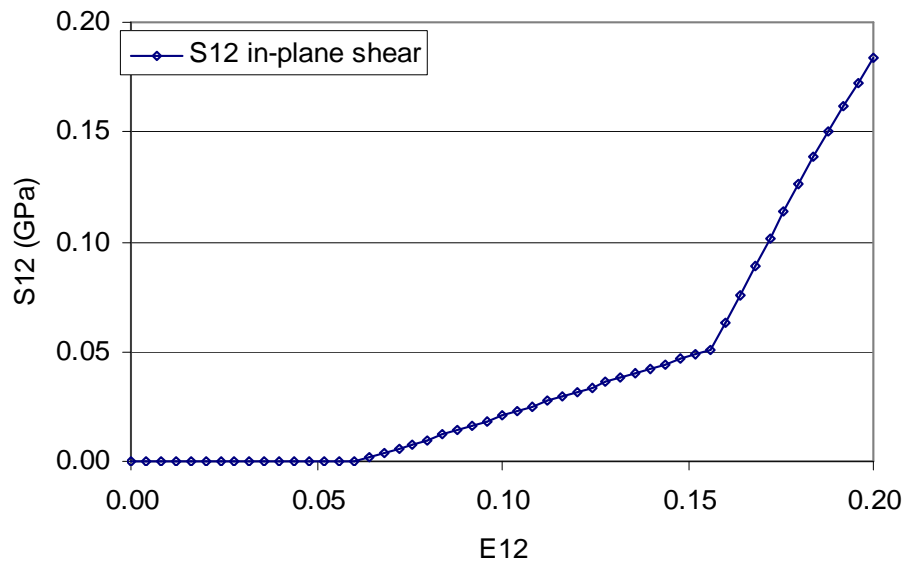
Figure 22: S_{12} vs. E_{12} for in-plane shear of a balanced weave with isotropic yarns

4.3.5.2 Transversely isotropic yarns

With the problems observed for the isotropic yarns, a transversely isotropic material model is tested here. The material parameters are chosen as follows:

$$\lambda = 0.4457, \ \mu = 0.5154, \ \alpha = 0.2714, \ \beta = 0.06548 \text{ and } \gamma = 10.54 \ (GPa),$$

which are deduced from the mechanical properties of a singe Kevlar[®] KM2 fiber given in [61] with its axial shear stiffness further reduced. The assumption is that as a fiber bundle, a yarn has lower shear stiffness than a single fiber due to the sliding amongst fibers. This assumption may need further investigation as the friction and/or the twisting in fibers may stiffen the yarn. However, this set of parameters is adopted as a test example to show the effect of the material anisotropy in yarns on the overall fabric properties. The deformations considered include biaxial extension, uniaxial extension, and in-plane shear. The deformed configurations are shown in Fig.23.

(a) Undeformed configuration   (b) Biaxial extension

(c) Uniaxial extension   (d) In-plane shear
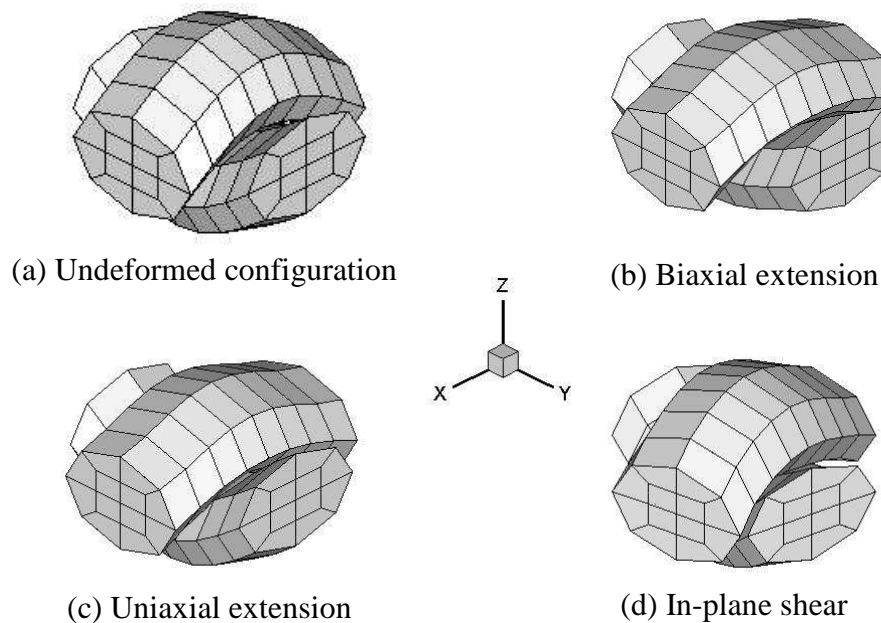
Figure 23: Undeformed and deformed configurations of a balanced weave with transversely isotropic yarns

The homogenized macroscopic stress and strain relations in biaxial/uniaxial extensions are shown in Fig.24. In addition, the stress-strain curve without considering the yarn contact is plotted as well. Stiffening and nonlinearity are clearly observed in the stress-strain curves. Due to the low shear stiffness, the yarns can be decrimped with little effort, which corresponds to the initial compliant decrimping response. When firm yarn contact is established, stiffening occurs. In Fig.24, S_{22} for the uniaxial extension is significant compared to that in Fig.21, which indicates that for the transversely isotropic yarns, the crossing yarn is stretched as the contact develops.
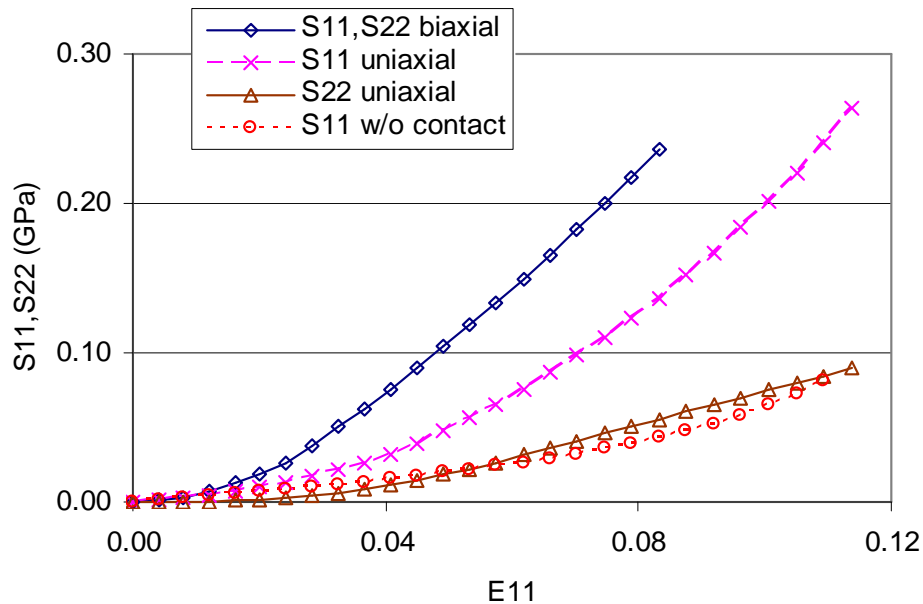
Figure 24: S_{11} and S_{22} vs. E_{11} for biaxial and uniaxial extension of a balanced weave with transversely isotropic yarns

The unit cell is also loaded by biaxial compression. Since no yarn contact develops as the unit cell deforms, compliant stress response is observed in biaxial compression. Fig.25 shows the biaxial extension-compression stress-strain relation. Stiffening due to the shear locking is found in the stress-strain relation of in-plane shear (Fig.26).
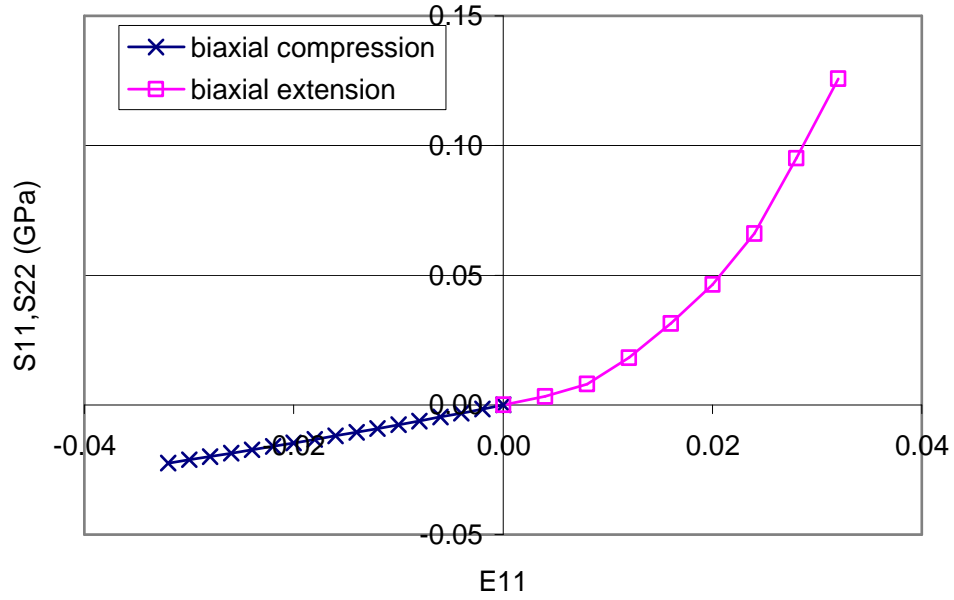
Figure 25: S_{11}, S_{22} vs. E_{11} for biaxial extension and compression
of a balanced weave with transversely isotropic yarns
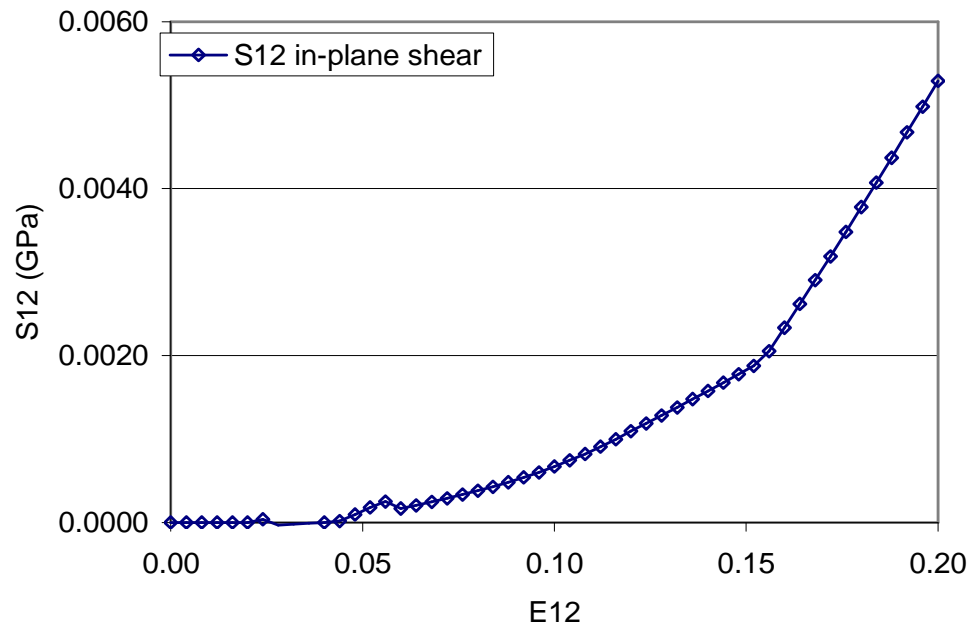
Figure 26: S_{12} vs. E_{12} for in-plane shear of a balanced weave
with isotropic yarns

<u>4.3.5.3 Full-period unit cell model</u>

   The previous computations are based the quarter unit cell model shown in Fig.19c. The model is anti-symmetrical about the fabric plane and does not represent a repeating pattern of the mesoscale yarn structure topology. In this subsection, a full unit cell model as shown in Fig.19b is constructed and the homogenization results obtained with the full model are then compared with those of the quarter model.
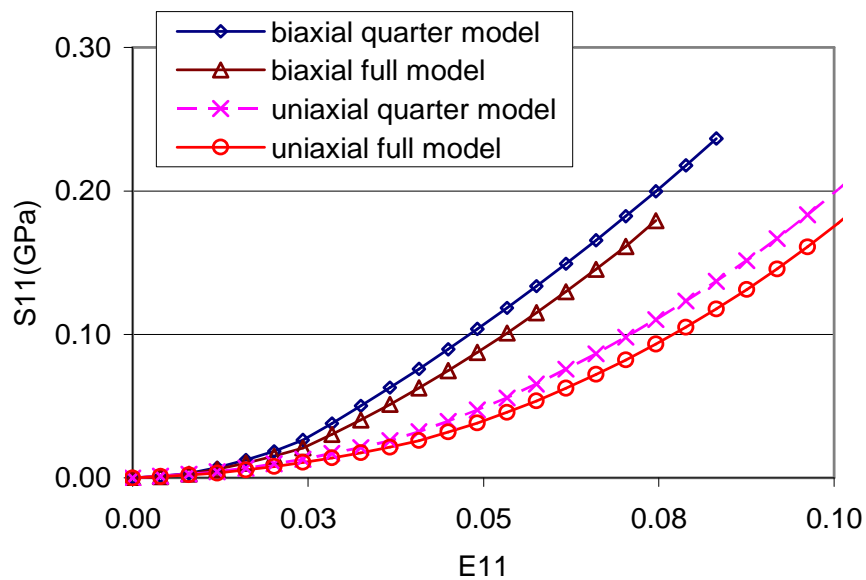
Figure 27: Comparing S_{11} vs. E_{11} for the quarter and the full unit cell models in biaxial and uniaxial extensions

   The stress-strain relations for biaxial- and uniaxial extension for both models are plotted in Fig.27, and it is found that the responses of the full-period unit cell are more compliant compared to those of the quarter model. One reason is due to the boundary conditions applied here. In both unit cell models, the local vertical displacements on the end faces of a yarn are restricted. The cross section at the yarn inflection point in the full model is free to move vertically. However, as an end face, the section is restricted in the

quarter model. Due to this reason, the quarter model is over-restricted compared to the full model and thus exhibits stiffer responses. An even more pronounced difference is observed in in-plane shear (Fig.28), where two perpendicular yarns tend to slide vertically as they are jam against each other when the shear deformation develops. Stronger resistance is thus exerted in the quarter unit cell model as the vertical displacement is more restricted than in the full unit cell model.

The deformed configurations of the full unit cell under the prescribed macroscopic strains are shown in Fig.29, where both a perspective view and a top view are presented for each load case. In Fig.29c, it can be found that the yarns warp under the application of contact tractions.
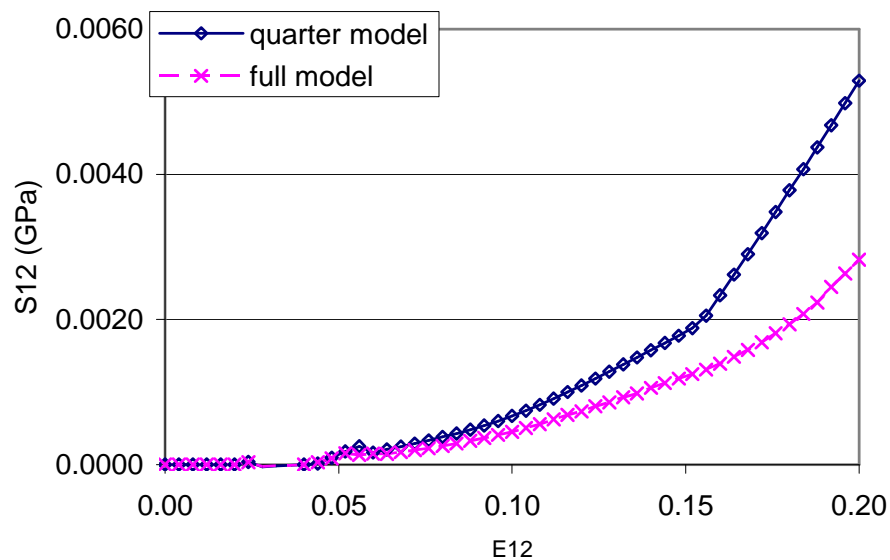
Figure 28: Comparing S_{12} vs. E_{12} for the quarter and the full unit cell models in in-plane shear
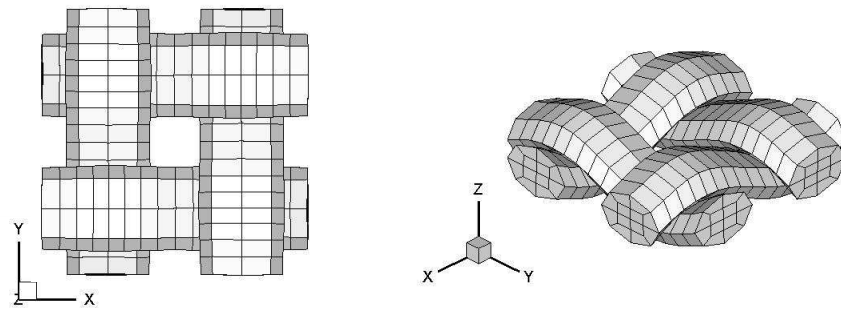
(a) Biaxial extension
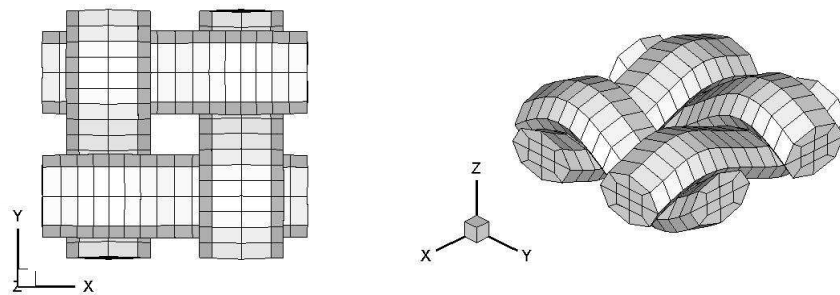
(b) Uniaxial extension
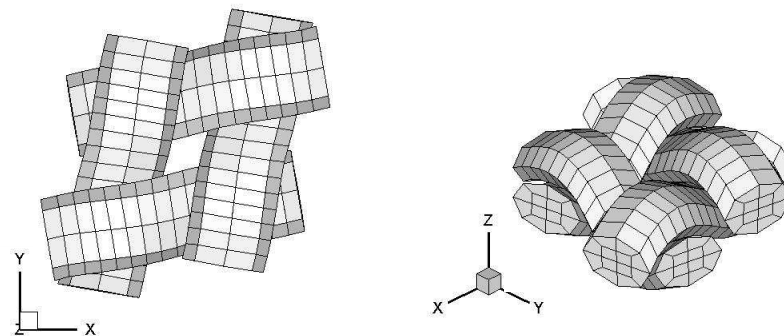
(c) In-plane shear

Figure 29: Deformed configurations of the full unit cell model

4.3.5.4 Mesh convergence

The last study is on the mesh convergence of the unit cell model. A model with finer mesh (Fig.30) is constructed and the stress-strain relations obtained with the fine model are compared with those of the coarse model in Fig.32 and Fig.33. It is found that

the responses obtained with the finer mesh are generally stiffer. This can be explained by the fact that more potential penetrations are identified with a finer mesh, which leads to a larger contribution from contact tractions. One problem with the current collision detection algorithm is that the edge-to-edge penetration is not checked. As shown in Fig.31, the edge-to-edge penetration occurs especially when a coarse mesh is employed and a fine mesh does help in identifying the penetration.

(a) The coarse mesh   (b) The fine mesh
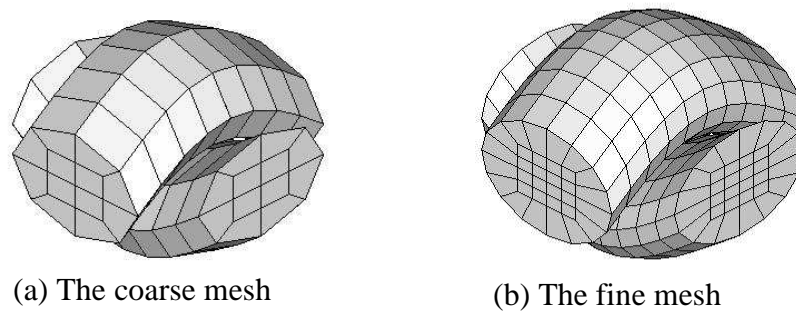
Figure 30: The unit cell models with different mesh densities
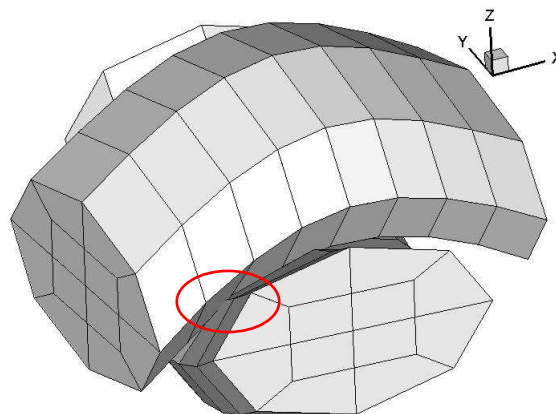
Figure 31: Edge-to-edge penetration in a coarse surface mesh
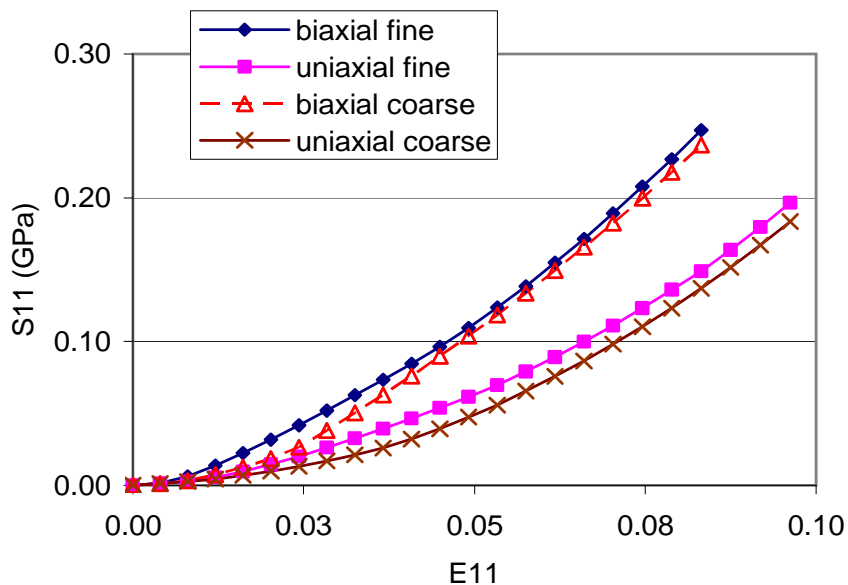
Figure 32: Comparing S_{11} vs. E_{11} for unit cell models of different mesh densities in biaxial and uniaxial extensions
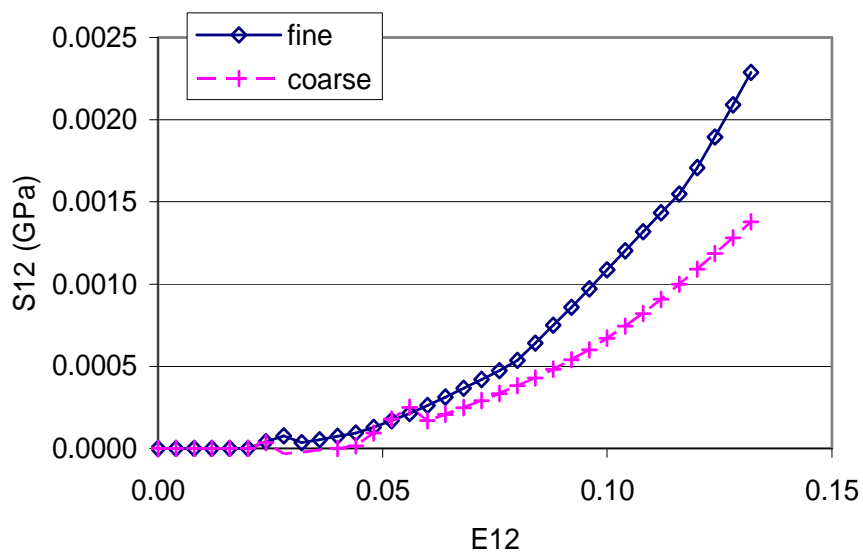
Figure 33: Comparing S_{12} vs. E_{12} for unit cell models of different mesh densities in in-plane shear

4.3.6 Discussion

The examples presented above demonstrate the effectiveness of the computational homogenization and unit cell analysis approach in studying the material properties of woven fabrics. Given yarn properties and the configuration of a yarn structure, the unit cell can predict the overall fabric properties. This capability can be exploited when novel fabrics are to be designed, where various combinations of the design parameters can be tested and identified. Compared to the early yarn structure models, the unit cell model described here captures the three-dimensional geometry of yarns and does not require any extra yarn interaction assumption, which usually introduces extra parameters and most likely more uncertainties as well.

A major uncertainty of the unit cell model is the yarn properties. In this study, yarns are modeled as a transversely isotropic material and the parameters are simply estimated from those of a single fiber. However, as a complex structure with microscopic constituent fibers, a yarn exhibits properties different from those of a single fiber. To realistically describe the material properties of a yarn, the same computational homogenization approach can be adopted. On this level, a yarn is considered as a structure composed of interacting fibers on microscale and the yarn properties are determined by homogenizing the microscopic response of the fiber bundles.

As presented in the examples, unit cell analysis yields homogenized stress and strain relations. However, these relations may not be directly applicable to the macroscopic problems due to the limitations of available mechanism to incorporate such relations. For example, in the clothing simulation the macroscopic problems are essentially the time integration of a dynamic shell model, which currently admits hyperelastic constitutive laws. As a result, the homogenized constitutive relations based on the unit cell analysis can not be applied to the clothing simulation unless they are cast as a strain energy function definition. For complex materials, such as woven fabrics, it can be challenging to find a single yet comprehensive mathematical form for the energy

function definition, which includes all complex mesoscale yarn interactions and their couplings with various load conditions. Such an effort has been made by Kim [62], who constructed a transversely isotropic hyperelastic model to describe homogenized yarn properties based on unit cell analysis of fibers. As observed in the paper, as the strain increases the hyperelastic model and the homogenization results deviate.

An alternative approach is multiscale modeling. Rather than constructing a material model and fitting homogenization results to the model, the unit cell analysis is conducted when the constitutive relation is needed on macroscale. The idea is to skip the closed form of the stress-strain relation but to consult the unit cell whenever the constitutive relation is needed. An outline of such an approach is described in [56]. One challenge is to obtain the sensitivity of the unit cell problem, which may be needed when constructing the tangent operator on macroscale, a procedure similar to derive consistent tangent operators for return mapping algorithms in computational plasticity as discussed by Simo and Hughes in [63].

CHAPTER 5

CLOTHING-WEARER INTERACTION STUDY

In this chapter, unilateral interactions between clothing and a wearer are studied. The clothing is modeled by the macroscale shell fabric model developed in Chapter 2 and the contact constraints between the clothing and the human body are enforced using the explicit contact algorithm introduced in Chapter 3. Human motions are prescribed and the contact forces that clothing exerts on the body are calculated so that the effects of these contact forces can be related to human performance measures.

The moment of all contact forces about joint centers are spatially integrated to obtained instantaneous joint torques. Although the joint torque can be readily determined by spatial integral of the torques exerted by individual contact forces, care must be taken to determine the correct contributing area for a given joint. For example, whether clothing contact forces on a forearm contribute to a meaningful torque about the shoulder joint is an issue to be studied. This problem is beyond the scope of this study, however, it is not investigated here. A simple assumption utilized in the following study is that clothing contact forces on a given body segment only contribute resisting torque to the joints directly connected to the segment.

Two problems are studied in this chapter. One is the sleeve-arm interaction problem, where the elbow flexing motion at an arm clothed in a sleeve is considered. Various parameters of the sleeve are investigated and the changes in the computed resistance torques about the elbow are compared. The other problem involves a fairly complicated human motion, in which the lower body clothed in a pants model walks and then steps over a two-foot tall obstacle. The computed time histories of the resistance torques exerted by the clothing about the right knee for two types of pants are compared.

<u>5.1 Human body representation and motion description</u>

As discussed in Chapter 3, general mesh-to-mesh collision detection can be expensive for large scale problems. In clothing-wearer interaction studies, a fine clothing mesh is usually employed to capture the flexible characteristics of fabrics. If the human body surface were to be modeled with a fine polygonal mesh, the cost of crude mesh-to-mesh collision detection would be very high. For this reason, the human body surface is grossly approximated herein by an assembly of ellipsoids, with which collision detection can be readily performed. An example is shown in Fig.34, where the lower body is represented by eight ellipsoids. For further simplification, the ellipsoids (the human body surface) are assumed to be rigid such that surface deformation, including that incurred by clothing interaction, is neglected. This assumption allows the contact problem to be solved as Signorini's problem as discussed in Chapter 3.
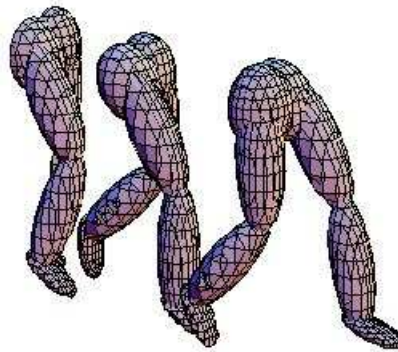
Figure 34: A lower-body walking model using ellipsoids

In the current study, the wearer's motion is fully prescribed and does not change in response to clothing resistance forces. Depending on its complexity, the motion is specified using different kinematics descriptions. A simple motion, such as flexing the elbow of an arm, can be specified as a time-history function of the rotation angle.

Complex motions, such as the walking shown in Fig.34, however, are described by leveraging the motion capture techniques. An optical motion capture system is utilized here and a human subject, wearing a special motion capture suit with reflective markers attached, is asked to perform given motions. The time history of each marker's position is recorded and the captured motion is re-constructed by the system on the subject's digital counterpart, a predefined skeleton model, where the position history of each joint is calculated.

For the clothing-wearer study, the motion based on the skeleton model needs to be further mapped to the ellipsoidal human model. Suppose for each segment, the position histories of two joints $\mathbf{J}_1$ and $\mathbf{J}_2$, and an auxiliary marker $\mathbf{M}$ are known, the centroid and the orientation basis of the ellipsoid at any instant in time are then constructed as follows:

Center:
$$\mathbf{x}^c = \frac{1}{2}(\mathbf{J}_1 + \mathbf{J}_2)$$

Orientations: $\qquad\qquad\qquad\qquad\qquad\qquad\qquad\qquad\qquad\qquad$ (5.1)

$$\hat{\mathbf{e}}_1 = \frac{\mathbf{J}_2 - \mathbf{J}_1}{|\mathbf{J}_2 - \mathbf{J}_1|}; \quad \hat{\mathbf{e}}_2 = \frac{(\mathbf{M} - \mathbf{x}^c) - \left[(\mathbf{M} - \mathbf{x}^c)\cdot\hat{\mathbf{e}}_1\right]\hat{\mathbf{e}}_1}{\left\|(\mathbf{M} - \mathbf{x}^c) - \left[(\mathbf{M} - \mathbf{x}^c)\cdot\hat{\mathbf{e}}_1\right]\hat{\mathbf{e}}_1\right\|}; \quad \hat{\mathbf{e}}_3 = \hat{\mathbf{e}}_1 \times \hat{\mathbf{e}}_2$$

A schematic of the motion reconstruction is shown in Fig.35.
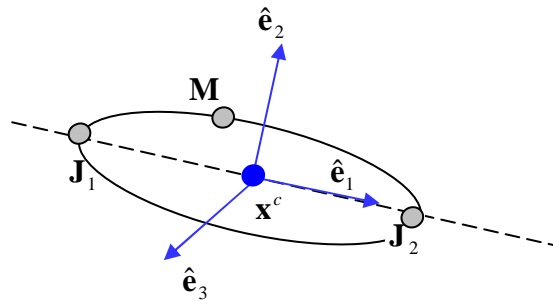
Figure 35: Re-constructing the motion of each ellipsoid using motion capture data that records for each ellipsoid the position histories of points $\mathbf{J}_1$, $\mathbf{J}_2$, and $\mathbf{M}$

5.2 Garment modeling

Clothing or garment is generally constructed by sewing pieces of fabric patches together. The properties of a garment depend not only on the fabric properties but also on the structural factors, such as seams, stitches and multiple fabric plies etc. In this study, these structural factors are neglected. No stitches or seams are modeled and a garment is assumed to be a uniform system of given fabrics. Multiple fabric meshes are simply combined to create a single mesh for a garment model. The sleeve studied in Section 5.3 is modeled as a mesh of a cylindrical tube. While the pants in Section 5.4 are constructed by combining four rectangular meshes along appropriate seam lines.

5.3 Arm-sleeve interaction study

In this problem, the interaction between an arm represented by two rigid ellipsoids and a cotton sleeve is studied. The motion considered is to flex the forearm about the elbow joint while keeping the upper arm fixed. The torque exerted by the sleeve about the elbow joint is calculated. The sleeve is modeled as a cylindrical tube with length $L = 0.5m$, radius $R = 0.06m$, and thickness $t = 1mm$. Boundary conditions are specified to restrain the motion of fabric nodes around the shoulder. The upper- and fore-arms are modeled as two ellipsoids, one fixed in space and the other rotating about the joint with a constant angular velocity. The total rotation angle is $57°$ before severe clothing self-contact occurs. The friction between the sleeve and the body surface is considered and a Coulomb friction coefficient $\mu = 0.1$ is assumed. The material properties used in the computation are as follows: Young's modulus in warp and weft directions $E = 1.2MPa$, shear modulus $G = 0.1MPa$, and mass density $\rho = 436Kg/m^3$.

5.3.1 Convergence study

The convergence behavior of the model in terms of mesh refinement is investigated. Four models with varying mesh densities (Fig.36) are constructed and then resistance torque vs. rotation angle curves are obtained (Fig.37). It is found that the

curves deviate slightly but follow the similar trend of reduced resistance with increasing refinement. A comparison of the computed deformations (Fig.38) shows that finer meshes capture local fabric buckling, which may not occur on the coarser meshes. The finding of increasing localized fabric buckling with increasing mesh refinement indicates the instability of the system. The same convergence study was conducted with a higher friction coefficient $\mu = 0.5$, and better convergence behavior is observed (Fig.39). As shown in the deformed configurations (Fig.40), higher friction between the arm and the sleeve prevents the sleeve from falling down onto the elbow joint and thus reduces the amount of wrinkling that occurs at the elbow. A comparison of Fig.37 and Fig.39 indicates that clothing resistance torques increase very significantly with higher friction between the arm and sleeve.

Mesh I: 10x13 elements   Mesh II: 15x20 elements

Mesh III: 20x26 elements   Mesh IV: 30x39 elements
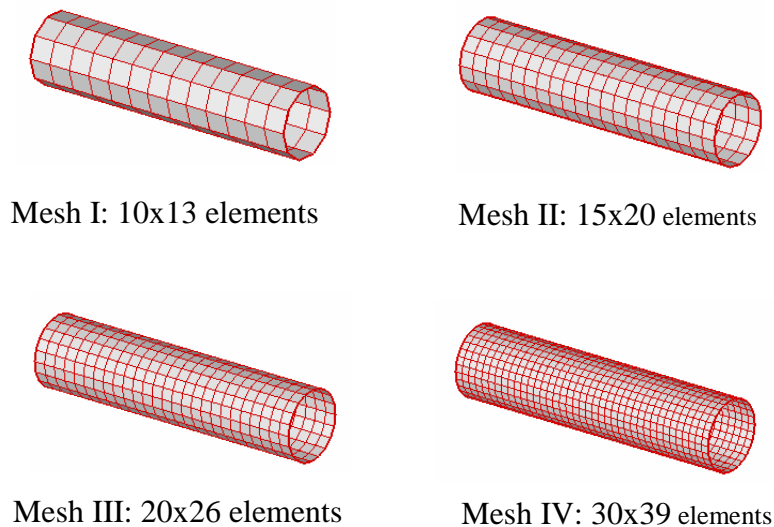
Figure 36: Sleeve models of increasing mesh refinement for convergence study
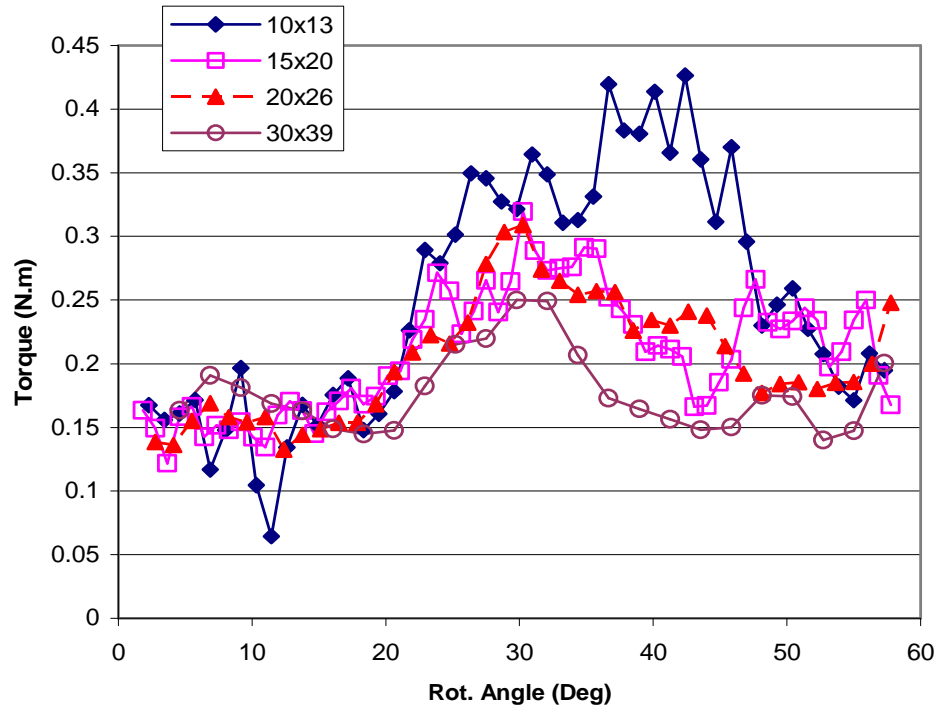
Figure 37: Computed clothing resistance torques about the elbow joint for a crimped cotton sleeve with varying mesh refinement; the Coulomb friction coefficient between arm and sleeve was $\mu = 0.1$
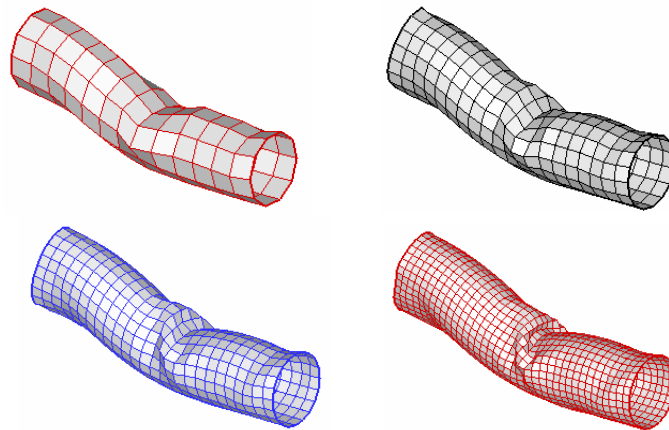
Figure 38: Illustration of localized clothing buckling in the elbow joint with increasing mesh refinement (low friction $\mu = 0.1$); Meshes are shown at elbow flexion angle $\alpha = 37°$
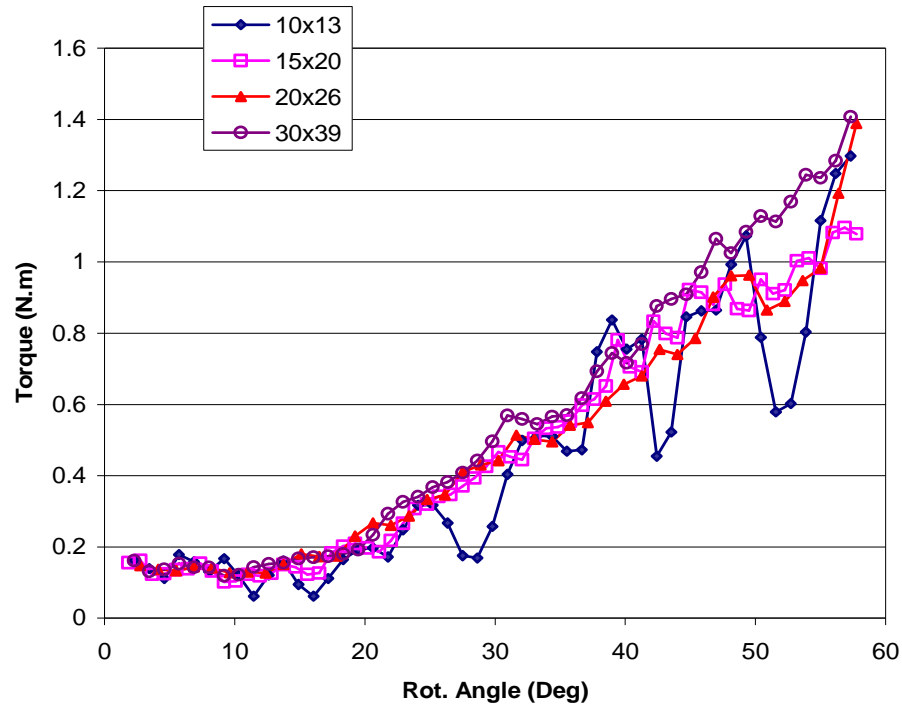
Figure 39: Computed clothing resistance torques about the elbow joint for a crimped cotton sleeve with varying mesh refinement; Coulomb friction coefficient between arm and sleeve was $\mu = 0.5$
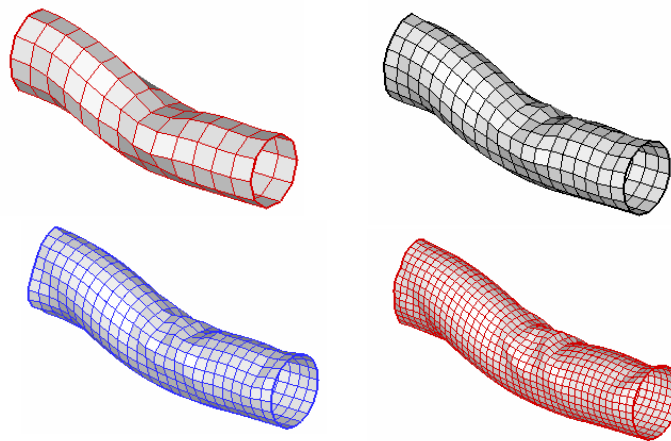
Figure 40: Local buckling is less sensitive to mesh refinement for higher arm-sleeve friction coefficient $\mu = 0.5$. Meshes are shown at elbow flexion angle $\alpha = 37°$.

5.3.2 Friction

The friction between clothing and human body surface is an important factor affecting the interaction of the two. For a sleeve model with a well-refined mesh, the low friction case ($\mu = 0.1$) is compared with a high friction case ($\mu = 0.5$). It is found once again that in the low friction case the sleeve slips down as the forearm rotates upward. Alternatively, in the high friction case, the sleeve does not slide down the forearm. Snapshots of the sleeve deformation for both the low and high friction cases are shown in Fig.41 at two elbow flexion angles, $\alpha = 37°$ and $\alpha = 57°$. It is noted once again that higher friction between the arm and sleeve translates to higher clothing resistance torque as indicated in Fig.42.

$\alpha = 37°$, $\mu = 0.1$ $\alpha = 37°$, $\mu = 0.5$

$\alpha = 57°$, $\mu = 0.1$ $\alpha = 37°$, $\mu = 0.5$
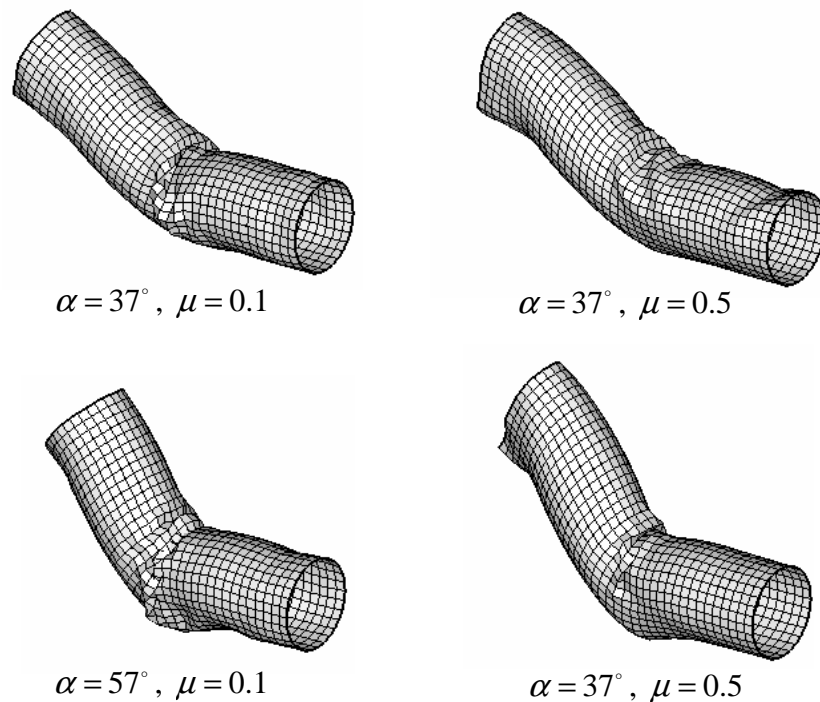
Figure 41: Sleeve deformations for different friction coefficients
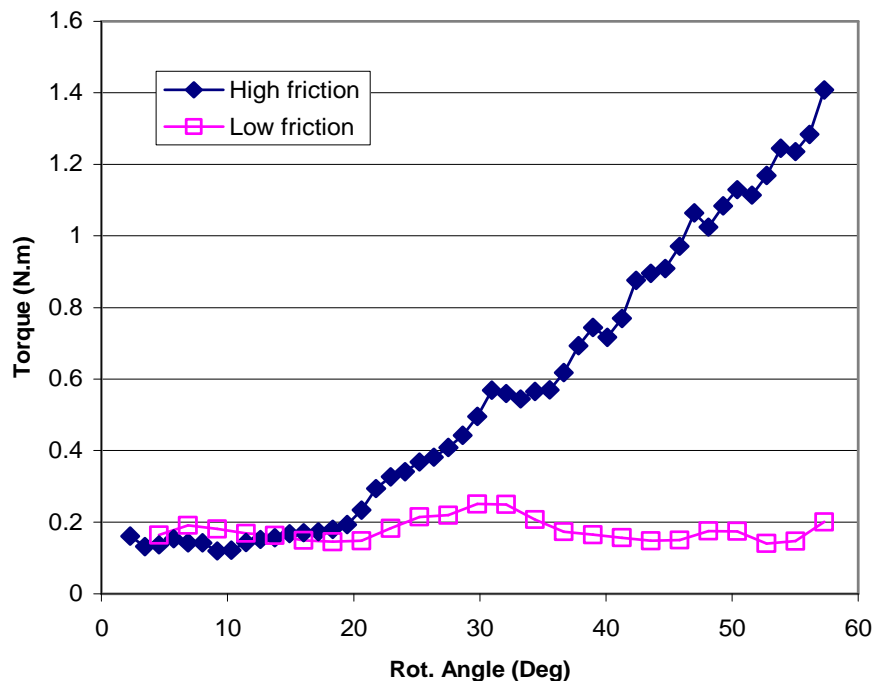
Figure 42: Clothing joint resistance torque exerted for different
surface friction coefficients

5.3.3 Effect of fit

To briefly study the effect of clothing fit on resistance, the radius of the sleeve tube is increased to $R = 0.07m$ from $R=0.06m$ while the dimensions of the ellipsoidal arms remain the same. The resisting torque exerted by the looser-fitting sleeve (Fig.43a) is compared with that of the original tighter-fitting sleeve (Fig.43b). For both fits, a skin surface friction coefficient $\mu = 0.5$ is used. The computed resisting torque exerted by the looser-fitting sleeve (Fig.44) is significantly less than that of the tighter-fitting sleeve for elbow flexion angles greater than $20°$.
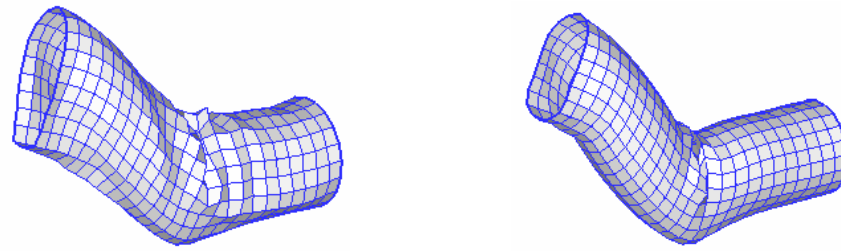
(a) Loose fit: *R*=0.07*m*   (b) Tight fit: *R*=0.06*m*

Figure 43: Deformed configurations of sleeves with different radii
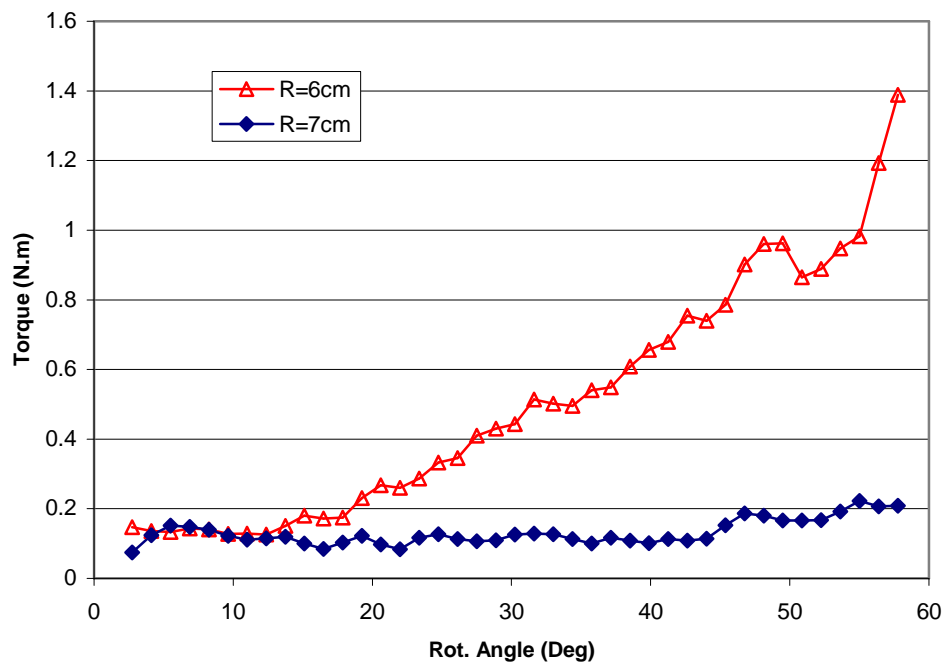
Figure 44: Computed resisting torques exerted by sleeves with different radii; the sleeve is compliant crimped cotton, and the skin friction coefficient is $\mu = 0.5$.

5.3.4 Effect of fabric thickness

Fabric thickness is another factor that can affect clothing-wearer interaction. A thicker fabric has greater mass and larger stiffness. Membrane stiffness increases in proportion to the fabric thickness, while the bending stiffness increases in proportion to the thickness cubed. Here, the thickness of the sleeve fabric is doubled to $t = 2mm$ and the joint torque is compared with the original case where $t = 1mm$. All other properties remain the same, and a surface friction coefficient $\mu = 0.5$ is assumed. The computed torque resistance (Fig.45) of the thicker fabric is roughly double that of the thinner fabric, which indicates that membrane rather than bending behavior of the sleeve is dominant.
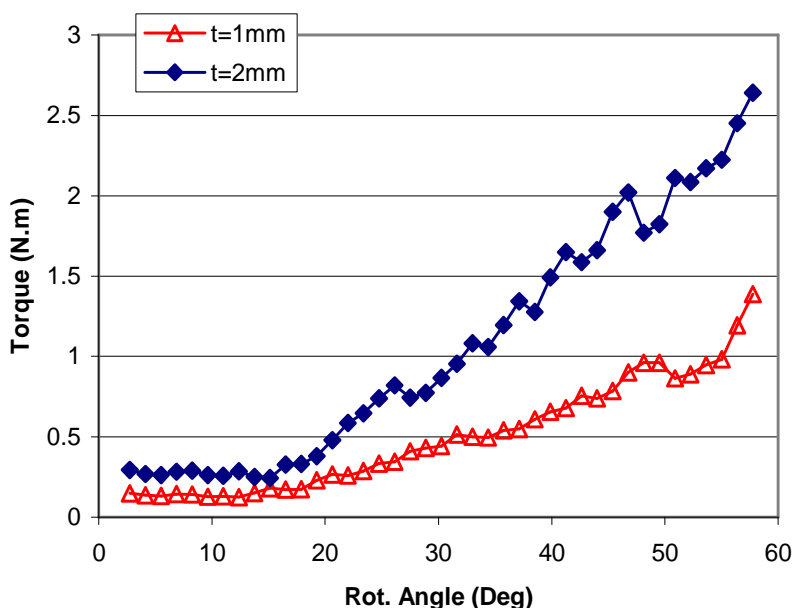
Figure 45: Comparison of sleeve torque resistance with different fabric thickness

5.3.5 Effect of fabric material properties

The last variation of the arm-sleeve problem examined here focuses on the effect of fabric material properties. Three sets of material properties are examined, roughly

corresponding to (I) a crimped cotton sleeve of thickness 1mm; (II) a taut de-crimped cotton fabric of thickness 1mm; and (III) a de-crimped plain-weave Kevlar fabric of thickness 1mm.

$$\text{Set I:} \quad E = 1.2 MPa, \quad \rho = 436 Kg / m^3$$
$$\text{Set II:} \quad E = 350 MPa, \quad \rho = 436 Kg / m^3$$
$$\text{Set III:} \quad E = 7.2 GPa, \quad \rho = 700 Kg / m^3$$

The shear stiffness of fabrics significantly affects their drapeability. For all of the three material assumptions considered here, the shear stiffness of the fabric in each case is taken as 1/200th of the Young's modulus in the yarn directions. Low surface friction $\mu = 0.1$ is assumed for all of the computations. The computed resistance torques for the three different sleeve materials are presented in Fig.46.
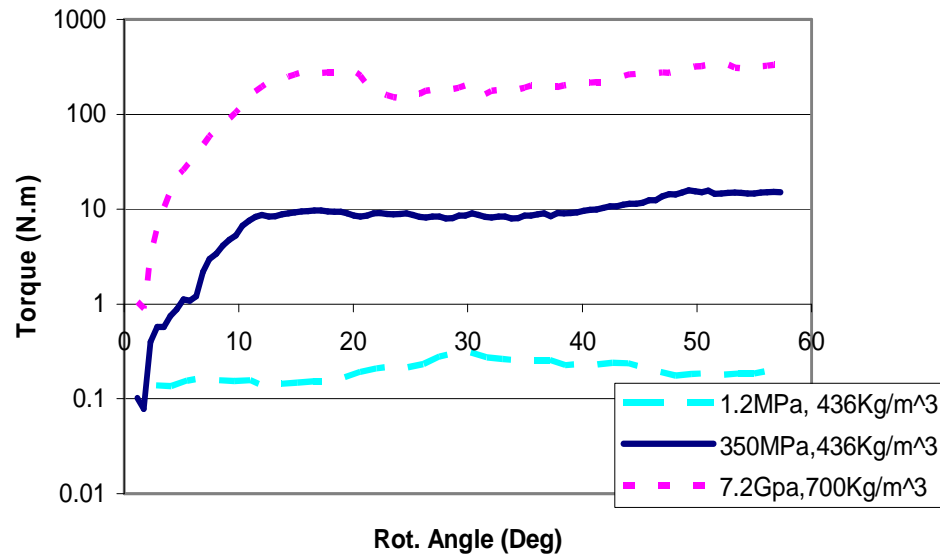
Figure 46: Comparison of sleeve torque resistance for types of fabrics

A stiff response is observed for both material sets II and III, and then a compliant response follows after the rotation angle reaches about 15°. By tracking the deformation

of the sleeve, it is found that before reaching an elbow flexion angle $\alpha = 15°$ the sleeve response is governed by bending; after that, the sleeve literally slides down along the forearm. As would be expected, it is also observed that the resistance torque exerted by each sleeve is roughly proportional to the stiffness of the material.

<p style="text-align:center">5.4 Interaction of pants with walking/stepping legs</p>

In this problem, a human subject walked four strides, with the third involving stepping over an obstacle $0.5m$ in height. The motion of this human was captured with an array of eight infrared VICON cameras, and the motions were then mapped onto the assemblage of ellipsoids (Fig.34) to make them walk. A pair of pants was then placed onto the human model (Fig.47) in the following sequence: (a) the feet of the human model were removed; (b) the pants of the human model were pulled up over the legs and pelvis; (c) the feet of the human model were then restored; and (d) the effect of a belt was created by tensioning the fabric at the waistline. With the garment on the human model, a simulation of the interaction between the pants and the lower body walking and crossing the obstacle was then undertaken (Fig.48). Two sets of pants were modeled, both made of compliant, crimped cotton. The first pair had a thickness of 1mm while the second had a thickness of 2mm.

The resistance that the pants models exert on the legs as they undergo their fully prescribed motions was calculated by taking the contact forces exerted by the clothing on the legs at each instant of the simulations and computing their instantaneous moment magnitude about the knees. Such computations are shown in Fig.49 for two pairs of cotton pants which are identical except for the fabric thickness. Not surprisingly, the thicker pants exert greater resistance torques than do the pants with the thinner fabric. The computed torques about the right knee are due strictly to the pants at the knee level and below. Contributions of the upper pant legs to the resistance have been neglected here.
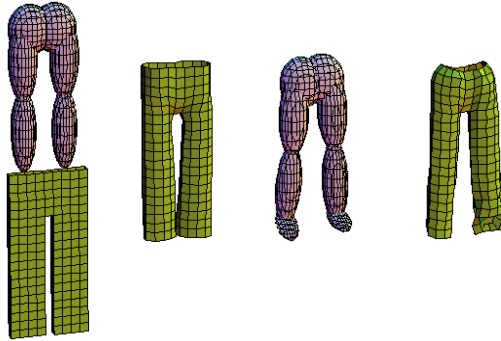
Figure 47: Sequence for the human model to don a pair of pants

| 500 | 400 | 300 | 200 | 1 |

| 900 | 800 | 700 | 600 |
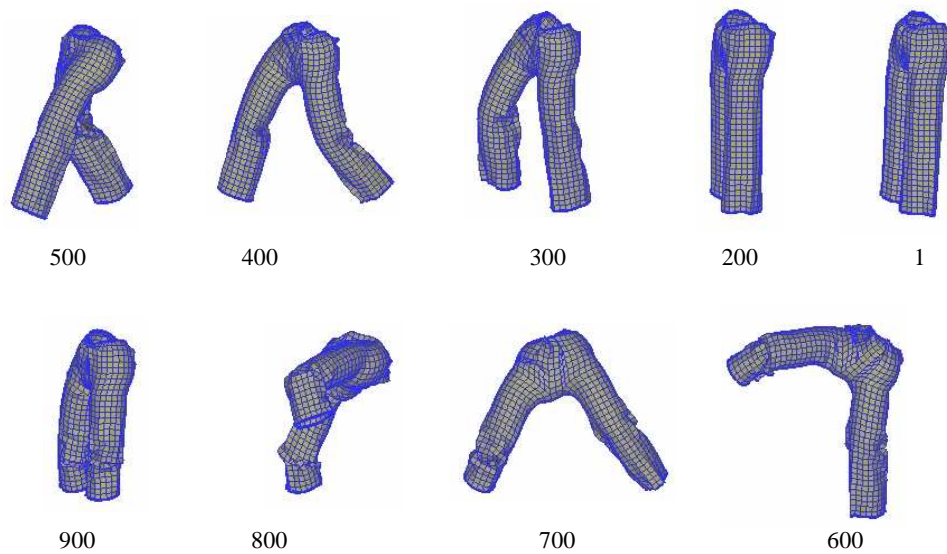
Figure 48: Simulation of pants interacting with lower body striding and then stepping over an obstacle. Numbers below each figure indicate the frame number of the simulation (c.f. Fig.49)
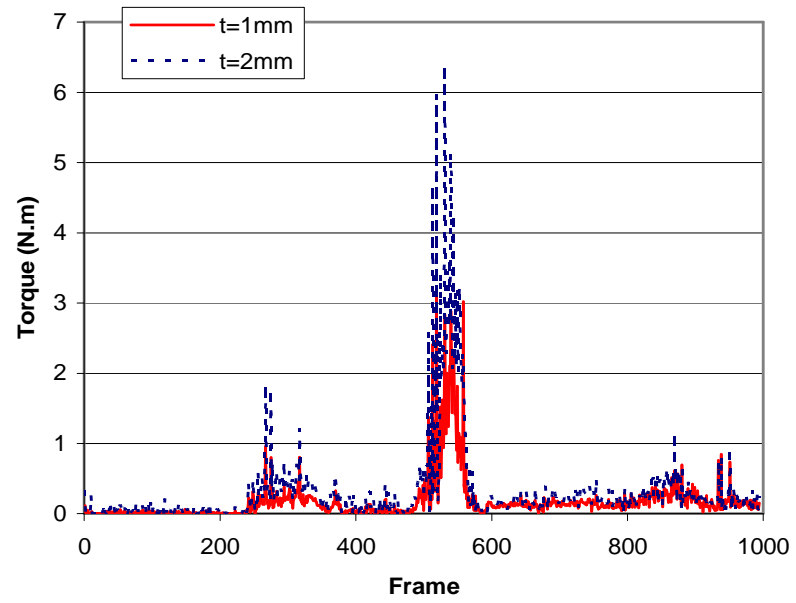
Figure 49: Computed resistance torques exerted by two pairs of cotton pants of different fabric thicknesses about the right knee

CHAPTER 6

SUMMARY AND DISCUSSION

6.1 Summary

6.1.1 Macroscale

A novel computational framework that allows quantification of the mechanical interactions between clothing and wearers is developed. In the framework, clothing is modeled using geometrically nonlinear continuum degenerated shell finite element methods and the wearer is represented by a digital human model with simplified ellipsoidal surface definition and motion capture kinematics description. The contact tractions exerted by clothing on the human model are calculated as a fundamental quantity, based on which objective performance measures can be derived to quantify the impact clothing imposes on the wearer. Sample studies are presented, where the effects of various factors (fabric thickness and properties, fit, and skin friction etc.) on the joint torques exerted by clothing are investigated, and these studies demonstrate the feasibility of the proposed computational framework. This novel computational facility allows the clothing-wearer interactions to be studied based on objective quantities and enables better understanding of the impact that clothing may impose on wearers. With such understanding, better designs of protective clothing systems with less performance restrictions can be obtained.

In developing the computational framework, some long-standing issues in solid mechanics are addressed. As thin and flexible media, fabrics exhibit highly unstable mechanical behaviors and undergo arbitrarily large deformations, which pose a challenge on the robustness of the computational model. In this work, a geometrically nonlinear shell element based on dynamic formulation is adopted to address this issue and it is proven to be effective in capturing the large fabric deformations with adequate robustness. Both implicit and explicit solution schemes are implemented and Rayleigh

damping is included to simulate the dissipation in the model. The clothing-wearer contact is formulated as a Signorini's problem by assuming rigid human body surfaces with prescribed kinematics and the problem is solved by an explicit Lagrange multiplier method. The expense for collision detection is minimized by using ellipsoidal surface definitions.

6.1.2 Mesoscale

Woven fabrics exhibit complex material behaviors that vary in response to changes in different loading conditions. It is challenging to develop a comprehensive constitutive model that captures all these complexities. In this work, the relation between the macroscopic fabric properties and the mesoscale yarn structures are studied by applying computational homogenization techniques.

A novel unit cell model with detailed three-dimension yarn geometries and general multi-body contact algorithm is developed. In this model, yarns are modeled as transversely isotropic media and their interactions are formulated as a multi-body frictional contact problem, which is solved by an augmented Lagrange multiplier method. Compared to previous efforts, the proposed model makes no simplifications on the yarn geometries and the yarn interactions, and it takes into account various combinations of loading conditions. The local response of the yarn structure unit cell model is solved for a given macroscopic strain and the macroscopic stress is obtained by homogenizing the total stress in the mesoscale model. It is demonstrated that the proposed unit cell model captures typical features of fabric behaviors.

The proposed unit cell model of mesoscale yarn structures provides a useful numerical tool for studying fabric properties. Compared to traditional experimental approaches, which require fabrication of testing samples, the unit cell analysis can be applied to test various combinations of factors that can affect the overall fabric properties and makes itself a rapid prototyping tool for fabric designs.

<div align="center">6.2 Discussion</div>

The main effort of this research is the construction of the proposed computational clothing modeling framework. The framework includes four major components: a macroscale fabric model, a mesoscale fabric/material model, a contact computation component, and a digital human model. Simplification assumptions have been introduced when these components are developed and integrated. In this section, these assumptions are revisited and future improvements on them are discussed as well.

<div align="center">6.2.1 Macroscale fabric modeling</div>

The macroscale fabric model is based on the continuum degenerated shell theory, where the bending behavior is obtained by numerical integration of stresses and strains through the shell thickness. This assumption is valid for a continuum, while for fabrics, which possess material discontinuities through the thickness, it may need to be revised. A resultant shell formulation may be more appropriate to address this issue.

Another assumption that deserves further investigation is the constitutive model. Currently a linear relation between the second Piola-Kirchhoff stress and the Green Lagrange strain, i.e. St. Venant model, is followed. This over-simplifies the material responses in fabrics even in the small strain range where complex yarn interactions on the mesoscale lead to highly nonlinear behaviors as demonstrated in Chapter 4. This topic is closely related to the multiscale modeling approaches discussed in the following subsection.

<div align="center">6.2.2 Multiscale modeling approaches</div>

The proposed unit cell analysis of mesoscale yarn structure model is currently independent of the macroscale fabric model and the homogenized stress-strain relation is not incorporated into the macroscale model. Two types of multiscale approaches are usually adopted to incorporate the homogenized constitutive relation into the macroscale model. One is the hierarchical multiscale approach, where the homogenized stress-strain

relations obtained by unit cell analyses are described by some mathematical constitutive functions, which are employed on the macroscale. However, the challenge with such an approach is the complexity of fabric properties, which rarely admits such comprehensive constitutive function expressions. An alternative approach is the concurrent multiscale method, which starts a mesoscale unit cell analysis whenever the constitutive relation is requested by the macroscale computation. With this approach, the macroscopic strain is applied as prescribed load on the unit cell and the resultant homogenized stress is returned to the macroscale problem as the response. The concurrent approach deserves further exploration for incorporation of realistic fabric properties. It is worth noting that concurrent multiscale modeling requires robust and efficient solution of the unit cell problem, and much progress has been made on this issue in this work.

6.2.3 Collision detection

In the current framework, the collision detection is simplified to reduce the computational expense. On the macroscale, the collision detection is conducted between a general clothing mesh and ellipsoidal surfaces that represent segments of the human body. On the mesoscale, mesh-to-mesh collision detection is confined to a local level, where only the neighbors in the initial configuration are checked. For highly distorted meshes, global collision detection is required and the efficiency of the algorithm becomes a significant issue. An efficient global mesh-to-mesh collision detection algorithm is beyond the scope of this study and was not pursued here. However, if a general body surface mesh as shown in Fig.50 is to be employed or the self-contact between clothing is to be considered, an efficient collision detection algorithm is needed.

6.2.4 The human model

As the main focus of the study is on clothing modeling, a simple human model is employed. As mention above, the body is approximated by an assembly of ellipsoids with its kinematics description obtained from motion capture. An obvious limitation of

the current model is the loss of geometric fidelity by using ellipsoids. To address this issue, realistic human body surface models need to be constructed. Body scan techniques can be employed for this purpose and a sample body scan mesh by courtesy of Professor Susan Ashdown and her Cornell Body Scan Research Group is shown in Fig.50.
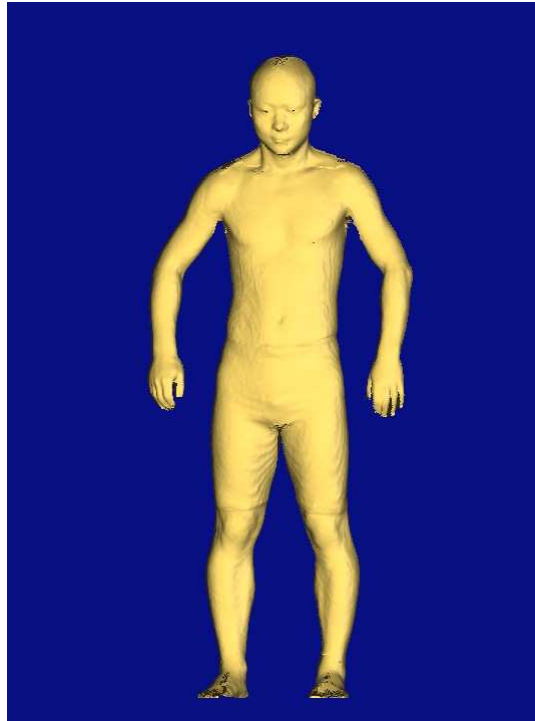
Figure 50: A human body surface mesh constructed using body scan techniques (courtesy of Dr. Ashdown at Cornell University)

Body scans can only capture the body surface at static postures. For clothing-wearer studies, however, the continuous evolution of the surface is needed as the human model engages in activity. To create the information, the body scan and the motion capture technique should be combined. The idea is to decompose the mesh into segments and to associate each of them with the corresponding segment in a motion capture model. The kinematics description obtained from motion capture system can then be mapped

onto the body surface mesh and drive it through the captured motion. With this method, the deformation of the body surface is not included and some mesh discontinuity and overlapping will inevitably occur as the motion proceeds. Mesh merging and patching techniques are thus needed to construct a continuous surface mesh in motion.

Currently the motion of the human model is completely prescribed either by time functions of joint angles or motion capture data. This treatment limits the clothing-wearer interaction to a unilateral situation, where clothing only responds passively to the given motion while cannot change the motion even though the restriction it exerts has made the motion unachievable. To enable the adaptation, more intelligent digital human model has to be employed. In addition, the sensitivity of the clothing restriction with respect to a given motion has to be investigated.

Another simplification used in the human model is that the body surface is rigid. This assumption simplifies the contact computation while excludes the effect of surface deformation in response to the clothing restriction.

6.2.5 Computational issue

The proposed clothing modeling framework is computationally intensive. On the macroscale, time integration of a dynamic system with complex contact computation and collision detection is performed. As mentioned in Section 6.2.3, a major bottleneck is an efficient global mesh-to-mesh collision detection algorithm. In addition, fast time integrators and parallel computation techniques are worth further exploring as well. The size of mesoscale yarn problem is relatively small. However, if it were to be applied in the multiscale computation framework, where each integration point corresponds to a mesoscale unit cell analysis problem, parallelization is definitely necessary.

6.2.6 Garment design

A huge factor that has been neglected in the current work is the garment design. In the example presented in Chapter 5, the pants are constructed by merging four rectangular mesh patches together. No design patterns are followed and the seams are not modeled. The neglected factors can be significant in determine the interactions of the final garment on the wearer and they need to be considered in the future work. For clothing pattern design, commercial garment computer-aided design (CAD) software, such as OptiTex, can be utilized. The pattern geometries can be created interactively with the graphical user interface the CAD software and then imported to the computation framework proposed in this work.

REFERENCES

[1] Paull, J.M. and Rosenthal, F.S., "Heat strain and heat stress for workers wearing protective suits at a hazardous waste site," *American Industrial Hygiene Association Journal*, 48: 458-463, 1987.

[2] Martin, H. deV. and Goldman, R.F., "Comparison of physical, biophysical and physiological methods of evaluating the thermal stress associated with wearing protective clothing," *Ergonomics*, 15: 337-342, 1972.

[3] Department of the U.S. Army, *Nuclear, Biological, and Chemical Protection (Field Manual No. FM 3-4)*, Washington, DC: Department of the U.S. Army, Headquarters, 1993.

[4] Johnson, R.F., McMenemy, D.J. and Dauphinee, D.T., "Rifle marksmanship with three types of combat clothing," *Proceedings of the Human Factors Society*, 34: 1529-1532, 1990.

[5] Alexander, M. and Laubach, L., "The effects of personal protective equipment upon the arm-reach capability of USAF pilots," *Proceedings Reprint of the Interagency Conference of Management and Technology in the Crew System Process*, 225-233, 1973.

[6] Huck, J., "Protective clothing systems: a technique for evaluating restriction of wearer mobility," *Applied Ergonomics*, 19(3): 185-90, 1988.

[7] Taylor, H.L. and Orlansky, J., "The effects of wearing protective chemical warfare combat clothing on human performance," *Aviation, Space, and Environmental Medicine*, 64(3, Sect2): A1-A41, 1993.

[8] Carter, B.J. and Cammermeyer, M., "Biopsychological responses of medical unit personnel wearing chemical defense ensemble in a simulated chemical warfare environment," *Military Medicine*, 150: 239-248, 1985.

[9] Bensel, C.K., "Soldier performance and functionality: Impact of chemical protective clothing," *Military Psychology*, 9(4): 251-300, 1997.

[10] Laing, R.M. and Sleivert, G.G., "Clothing, textiles and human performance," *Textile Progress*, 32(2): 1-132, 2002.

[11] Provot, X., "Deformation constraints in a mass-spring model to describe rigid cloth behavior," *Proc. Graphics Interface*, 147-154, 1995.

[12] Choi, K. and Ko, H., "Stable but responsive cloth," In *Computer Graphics (Proc. SIGGRAPH)*: 604-611, 2002.

[13] Breen, D.E., House, D.H. and Wozny, M.J., "A particle-based model for simulating the draping behavior of woven cloth," *Textile Research Journal*, 64(11): 663-685, 1994.

[14] Breen, D.E., House, D.H. and Wozny, M.J., "Predicting the drape of woven cloth using interacting particles," *Computer Graphics (Proc. SIGGRAPH)*: 365-372, 1994.

[15] Amirbayat, J. and Hearle, J.W.S., "The anatomy of buckling of textile fabrics: drape and conformability," *Journal of the Textile Institute*, 80(1): 51-69, 1989.

[16] Kawabata, S., *The Standardization and Analysis of Hand Evaluation*, The Textile Machinery Society of Japan, Osaka, 1980.

[17] Eberhardt, B., Weber, A. and Strasser, W., "A fast, flexible, particle-system model for cloth draping," *IEEE Computer Graphics and Applications*, 16(5): 52-59, 1996.

[18] Terzopoulos, D., Platt, J., Barr, A. and Fleischer, K., "Elastically deformable models," *Computer Graphics* (Proc. SIGGRAPH), 21(4) 205-214, 1987.

[19] Terzopoulos, D. and Fleischer, K., "Modeling inelastic deformation: viscoelasticity, plasticity, fracture," *Computer Graphics*, 22(4) 269-278, 1988.

[20] Carignan, M., Yang, Y., Thalmann, N.M. and Thalman, D., "Dressing animated synthetic actors with complex deformable clothes," *Computer Graphics* 26(2): 99-104, 1992.

[21] Collier, J.R., Collier, B.I., O'Toole, G. and Sargand, S.M., "Drape prediction by means of finite-element analysis", *Journal of the Textile Institute*, 82(1): 96-107, 1991.

[22] Chu, G.C., Cummings, C.L. and Teixeira, N.A., "Mechanics of elastic performance of textile materials. Part V: A study of the factors affecting the drape of fabrics – The development of a drape meter", *Textile Research Journal*, 20: 539-548, 1950.

[23] Cusick, G.E., "The measurement of fabric drape", *Journal of the Textile Institute*, 59: 253-260, 1968.

[24] Chen, B. and Govindaraj, M., "A physically based model of fabric drape using flexible shell theory," *Textile Research Journal*, 65(6): 324-330, 1995.

[25] Chen, B. and Govindaraj, M., "A parametric study of fabric drape," *Textile Research Journal*, 66(1): 17-24, 1996.

[26] Gan, L., Ly, N.G. and Steven, G.P., "A study of fabric deformation using nonlinear finite elements," *Textile Research Journal*, 65(11): 660-668, 1995.

[27] Bathe, K.J., *Finite Element Procedures in Engineering Analysis*, Prentice-Hall, Englewood Cliffs, NJ, 1982.

[28] Eischen, J.W., Deng, S. and Clapp, T.G., "Finite-element modeling and control of flexible fabric parts", *IEEE Computer Graphics and Applications*," 16(5): 71-80, 1996.

[29] Simo, J.C. and Fox, D.D., "On a stress resultant geometrically exact shell model. Part I: formulation and optimal parameterization," *Computer Methods in Applied Mechanics and Engineering*, 72: 267-304, 1989

[30] Simo, J.C., Fox, D.D. and Rifai, M.S., "On a stress resultant geometrically exact shell model. Part II: the linear theory; computational aspects," *Computer Methods in Applied Mechanics and Engineering*, 73: 53-92, 1989.

[31] Simo, J.C., Fox, D.D. and Rifai, M.S., "On a stress resultant geometrically exact shell model. Part III: computational aspects of the nonlinear Theory," *Computer Methods in Applied Mechanics and Engineering*, 79: 21-70, 1990.

[32] Hughes, T.J.R., *The Finite Element Method Linear Static and Dynamic Finite Element Analysis*, Prentice-Hall, Inc., Eaglewood Cliffs, NJ, 1987.

[33] Belytschko, T., Liu, W.K. and Moran, B., *Nonlinear Finite Elements for Continua and Structures*, John Wiley & Sons, Ltd., 2000.

[34] Etzmuss, O., Gross, J. and Strasser, W., "Deriving a particle system from continuum mechanics for the animation of deformable objects," *IEEE Transactions on Visualization and Computer Graphics*, 9(4): 538-550, 2003.

[35] Eischen, J.W. and Bigliani, R., "Continuum versus particle representations," *Cloth Modeling and Animation*, D.E., A K Peters, Ltd., Natick, MA, 79-122, 2000.

[36] Govindaraju, N.K., Lin, M.C. and Manocha, D., "Efficient collision detection among deformable objects using graphics processors," *PRESENCE*, *Special on Best Papers of IEEE Virtual Reality 2005*, 2006.

[37] Govindaraju, N.K., Kabul, I., Lin, M.C. and Manocha, D., "Fast continuous collision detection among deformable models using graphics processors," *Eurographics Symposium on Virtual Environments*, 2006.

[38] Laursen, T.A. and Simo, J.C., "A continuum-based finite element formulation for the implicit solution of multibody, large deformation frictional contact problems," *International Journal for Numerical Methods in Engineering*, 36: 3451-3485, 1993.

[39] Wriggers, P. and Simo, J.C., "A note on tangent stiffness for fully nonlinear contact problems," *Communications in Applied Numerical Methods*, 1: 199-203, 1985.

[40] Simo, J.C. and Laursen, T.A., "An augmented Lagrange treatment of contact problems involving friction," *Computers & Structures*, 42: 97-116, 1992.

[41] Laursen, T.A., *Formulation and Treatment of Frictional Contact Problems Using Finite Elements*, Ph.D. Dissertation, Department of Mechanical Engineering, Stanford University, 1992.

[42] Carpenter, N.J., Taylor, R.L. and Katona, M.G., "Lagrange constraints for transient finite element surface contact," *International Journal for Numerical Methods in Engineering*, 32: 103-128, 1991.

[43] Belytschko, T. and Neal, M.O., "Contact-impact by the pinball algorithm with penalty and Lagrangian methods," *International Journal for Numerical Methods in Engineering*, 31: 547-572, 1991.

[44] Hallquist, J.O., Goudreau, G.L. and Benson, D.J., "Sliding interfaces with contact-impact in large-scale Lagrangian computations," *Computer Methods in Applied Mechanics and Engineering*, 51: 107-137, 1985.

[45] Benson, D.J. and Hallquist, J.O., "A single surface contact algorithm for the post-buckling analysis of shell structures," *Computer Methods in Applied Mechanics and Engineering*, 78: 141-163, 1990.

[46] Kawabata, S., Niwa, M. and Kawai, H., "The finite-deformation theory of plain-weave fabrics – Part I: The biaxial-deformation theory," *Journal of the Textile Institute*, 64(1): 21-46, 1973.

[47] Kawabata, S., Niwa, M. and Kawai, H., "The finite-deformation theory of plain-weave fabrics – Part II: The uniaxial-deformation theory," *Journal of the Textile Institute*, 64(2): 47-61, 1973.

[48] Kawabata, S., Niwa, M. and Kawai, H., "The finite-deformation theory of plain-weave fabrics – Part III: The shear-deformation theory," *Journal of the Textile Institute*, 64(2): 62-85, 1973.

[50] King, M.J., Jearanaisilawong, P. and Socrate, S., "A continuum constitutive model for the mechanical behavior of woven fabrics," *International Journal of Solids and Structures* 42: 3867-3896, 2005.

[51] De Jong, S. and Postle, R., "A general energy analysis of fabric mechanics using optimal control theory," *Textile Research Journal*, 48(3): 127-135, 1978.

[52] De Jong, S. and Postle, R., "An energy analysis of woven-fabric mechanics by means of optimal-control theory, Part I: Tensile properties," *Journal of the Textile Institute*, 68(11): 350-361, 1977.

[53] De Jong, S. and Postle, R., "An energy analysis of woven-fabric mechanics by means of optimal-control theory, Part II: Pure-bending properties," *Journal of the Textile Institute*, 68(11): 362-369, 1977.

[54] De Jong, S. and Postle, R., "Modified equations for the energy analysis of the plain weave, including yarn extension – reply," *Journal of the Textile Institute*, 70(8): 359-364, 1979.

[55] Taban, F. and Luo, S., "Nonlinear deformation of woven fabrics," *Proceeding of IMECE*, TED-Vol.2: 63-69, 2002.

[56] Terada, K. and Kikuchi, N., "A class of general algorithms for multi-scale analyses of heterogeneous media," *Computer Methods in Applied Mechanics and Engineering*, 190: 5427-5464, 2001.

[57] Swan, C.C. and Kosaka, I. "Homogenization-based analysis and design of composites," *Computers & Structures*, 64: 603-621, 1997.

[58] Kim, H.J., Swan, C.C. and Lakes, R.S., "Computational studies on high-stiffness, high-damping SiC-InSn particulate reinforced composites," *International Journal of Solids and Structures*, 39: 5799-5812, 2002.

[59] Hassani, B. and Hinton, E., "A review of homogenization and topology optimization I-homogenization theory for media with periodic structure," *Computers & Structures*, 69: 707-717, 1998.

[60] Bonet, J. and Burton, A.J., "A simple orthotropic, transversely isotropic hyperelastic constitutive equation for large strain computations," *Computer Methods in Applied Mechanics and Engineering*, 162: 151-164, 1998.

[61] Cheng, M. and Chen, W., "Mechanical properties of Kevlar$^®$ KM2 single fiber, *Journal of Engineering Materials and Technology*, 127: 197-203, 2005.

[62] Kim, H.J., *Multi-scale Computational Homogenization of Composites with Voxel-based Meshing and Element Splitting Techniques*, Ph.D. Dissertation, Department of Mechanical Engineering, The University of Iowa, 2002.

[63] Simo, J.C. and Hughes, T.J.R., *Computational Inelasticity*, Springer, 1997.

[64] Limbert, G. and Taylor, M., "On the constitutive modeling of biological soft connective tissues a general theoretical framework and explicit forms of the tensors of elasticity for strongly anisotropic continuum fiber-reinforced composites at finite strain," *Internal Journal of Solids and Structures*, 39: 2343-2358, 2002.

[65] Spencer, A.J.M., *Continuum Theory of the Mechanics of Fiber-Reinforced Composites*, Springer Verlag. 1984.

[66] Kikuchi, N. and Oden, J.T., *Contact Problems in Elasticity: A Study of Variational Inequalities and Finite Element Methods*, SIAM, 1988.

[67] Zhong, Z.H., *Finite Element Procedures for Contact-Impact Problems*, Oxford University Press Inc., 1993.